

(BSD-TDR-62-299) STUDY OF THERMAL
RADIATION ASSOCIATED WITH NON-EQUILIBRIUM
AND EQUILIBRIUM FLOW IN THE APOLLO
FLIGHT REGIME (Avco-Everett Research Lab)
98 p

W70-73189

Unclass
21503

**AVCO
EVERETT**

RESEARCH LABORATORY

a division of
AVCO CORPORATION

CLASSIFICATION CHANGE

TO -

UNCLASSIFIED

By authority of

~~CONFIDENTIAL~~
E.O. 11652

Changed by

L. Shirley Date *10-30-73*

(U) STUDY OF THERMAL RADIATION
ASSOCIATED WITH NON-EQUILIBRIUM AND EQUILIBRIUM FLOW
IN THE APOLLO FLIGHT REGIME

R. A. Allen and P. H. Rose

RESEARCH NOTE 314

September 1962

sponsored by

**NATIONAL AERONAUTICS AND SPACE ADMINISTRATION
MANNED SPACECRAFT CENTER
APOLLO PROCUREMENT OFFICE**

under Contract NAS 9-156

**HEADQUARTERS
BALLISTIC SYSTEMS DIVISION
AIR FORCE SYSTEMS COMMAND
UNITED STATES AIR FORCE**

under Contract AF 04(694)-33

CONFIDENTIAL

~~CONFIDENTIAL~~

X64-10542

BSD-TDR-62-299

Document No. AERL 62-747
Copy 488 of 625 copies, Series A
RESEARCH NOTE 314

(U) STUDY OF THERMAL RADIATION ASSOCIATED WITH
NON-EQUILIBRIUM AND EQUILIBRIUM FLOW IN THE APOLLO
FLIGHT REGIME

by

R. A. Allen and P. H. Rose

AVCO-EVERETT RESEARCH LABORATORY
a division of
AVCO CORPORATION
Everett, Massachusetts

September 1962

sponsored by

NATIONAL AERONAUTICS AND SPACE ADMINISTRATION
MANNED SPACECRAFT CENTER
APOLLO PROCUREMENT OFFICE
Houston 1, Texas

under Contract NAS 9-156

HEADQUARTERS
BALLISTIC SYSTEMS DIVISION
AIR FORCE SYSTEMS COMMAND
UNITED STATES AIR FORCE
Air Force Unit Post Office
Los Angeles 45, California

under Contract AF 04(694)-33

This document contains information
affecting the National Defense of the
United States within the meaning of the
Espionage Laws, Title 18, U.S.C.,
Sections 793 and 794. Its transmission
or the revelation of its contents in any
manner to an unauthorized person is
prohibited by law.

~~CONFIDENTIAL~~

CONFIDENTIAL

THIS PAGE IS BLANK

CONFIDENTIAL

~~CONFIDENTIAL~~

ABSTRACT

Photometric measurements of the radiation behind normal air shock waves have been made in an electric arc-driven shock tube which produces shock waves at super-satellite re-entry velocities. These measurements and estimates of the radiation heating for a project Apollo vehicle and trajectory derived from these measurements are described in this report.

Measurements were made of the non-equilibrium and equilibrium radiation from normal air shocks at initial pressures varying from 1.0 to 0.05 mm Hg. (simulated altitudes 110,000 - 255,000 ft) and at shock velocities from 16,500 to 36,200 ft/sec. A calibrated grating, dual channel, monochromator and photomultipliers were used to obtain photometric measurements between .22 and .9 microns wavelength. A tungsten photoelectric gauge was used to obtain quantitative intensity results in the .075 - .14 micron region and a single channel prism monochromator with an infrared cell was used to obtain coverage at wavelengths beyond 1.0 micron.

Time histories of the resolved shock front radiation at various wavelengths and at various velocities and pressures were made and a parametric description of the radiation was obtained. The parameters measured include quantitative equilibrium and integrated non-equilibrium radiation intensities, the width of the non-equilibrium region, and the time required by the radiation to peak behind the shock front.

Spectroscopic techniques using an image converter and a drum camera operating in the race track mode were used to obtain time resolved spectra. N_2^+ (1-) and atomic nitrogen line radiation are found to be significant contributors to both the equilibrium and non-equilibrium radiation at 33,000 ft/sec. Experiments performed at different conditions of pressure and shock velocity validated the "binary scaling" of non-equilibrium radiation. "Collision limiting" of the N_2^+ (1-) band system radiation was also observed.

A summary of existing data on non-equilibrium air radiation was made. The value of 40 watts/cm² - 2 π ster. at 33,000 ft/sec was determined from the present experiments and found to be in good agreement with both the Ames Research Center ballistic range results covering the same velocity range and empirical extrapolations of our previous measurements at lower velocities. This value represents a source of heating which, in general, will be small compared to equilibrium radiation and to aerodynamic heating for an Apollo vehicle re-entering the earth's atmosphere.

A good non-equilibrium radiation theory is currently non-existent; however, an empirical calculation scheme has been developed which approximates the radiation observed. This calculational procedure has been incorporated into a flow field calculation for an Apollo re-entry vehicle. The results of this calculation show the normal shock approximation ignoring the presence of the body, describes both the non-equilibrium and equilibrium radiation to a factor less than two for the Apollo geometry.

~~CONFIDENTIAL~~

~~CONFIDENTIAL~~

THIS PAGE IS BLANK

-iv-

~~CONFIDENTIAL~~

TABLE OF CONTENTS

<u>Section</u>		<u>Page</u>
I	Introduction	1
II	Electric Arc-Driven Shock Tube	5
III	Monochromator Measurements	9
IV	Photoelectric Gauge Measurement (.075 μ to .14 μ Wavelength Region)	31
V	Total Radiation Measurements	35
VI	Photographic Techniques	43
VII	Present State of Knowledge	47
VIII	Non-equilibrium and Equilibrium Radiation in Flight	51
IX	Summary	69
	Acknowledgment	70
	Appendix A	71
	References	83

~~CONFIDENTIAL~~

THIS PAGE ~~IS~~ BLANK

-vi-

~~CONFIDENTIAL~~

~~CONFIDENTIAL~~

I. INTRODUCTION

For the past several years heat transfer for re-entry velocities of up to 25,000 ft/sec have been thoroughly explored.¹⁻⁴ For re-entry in the vicinity of 35,000 ft/sec, the radiative heating becomes a larger fraction of the over-all heat flux, and some feasible flight paths are such that the radiative heating could be the dominant heat flux.^{3,5,6}

At velocities in the range of 30,000 to 40,000 ft/sec, the translational temperature close to the shock front may be in the range of 40,000 to 75,000°K. If only the translational and rotational degrees of freedom are excited in the air immediately behind the shock front, this translational temperature is given by the Rankine-Hugoniot relationships for $\gamma = 7/5$. However the temperature is quickly reduced as the chemical and vibrational processes occur in the relaxation region behind the shock front. Due to a coupling between molecular electronic excitation and the thermodynamic condition of the gas, the molecular radiation in this relaxation region shows a considerable overshoot in intensity above the equilibrium level. This phenomenon is shown clearly in Fig. 1 by the drum camera spectrograms taken by race track techniques.⁷ The measurements shown were made on a 1.5" combustion driven shock tube on normal shocks in nitrogen. Figure A is a time resolved photograph; C an oscillogram record of radiation observed by a photomultiplier in the .55 - 1.0 μ wavelength region showing the radiative overshoot.

The chemical and excitation processes occurring in the non-equilibrium region of a shock front are binary reactions, i. e., the results of two body collisions. It follows from this fact that the intensity of radiation from this region should be proportional to the particle density, and the thickness of the region should be inversely proportional to the density. Consequently, as long as binary mechanisms predominate, the integrated radiation flux emitted from the non-equilibrium region should be independent of density at a given velocity. Experimental verification of binary scaling of the luminous front radiation was given in Refs. 8 and 9. It is also demonstrated by data collected in this study that the thickness of the non-equilibrium region and the time required for the radiation to reach its peak intensity scales with the ambient density as a binary phenomenon would scale.

There are four effects which can be predicted from the physics of radiation as applied to a body flow problem which can break down this binary scaling and depress the over-all gas cap radiation. Truncation, as discussed by Teare⁸ is the condition when the non-equilibrium region is thicker than the shock detachment distance and thus the profile is truncated by the body. Collision limiting,¹⁰ the second effect to reduce the radiation intensity occurs at low densities when the particle density in the gas is low so

~~CONFIDENTIAL~~

~~CONFIDENTIAL~~

that there are not sufficient collisions to maintain the population of excited states against the drainage by radiation. Experimental evidence of this effect is discussed later in this report. Thirdly, there is the radiation cooling⁸ which occurs when the level of radiation loss becomes an appreciable fraction of the total energy of the flow. Under non-equilibrium conditions, this phenomenon occurs at reduced densities where the flow energy, $1/2 \rho_{\infty} V_{\infty}^3$, is lower. Goullard¹¹ described a somewhat different radiation cooling effect for equilibrium radiation. Equilibrium radiation is a function of nose radius and is proportional to more than the first power of density. Radiation cooling by equilibrium radiation is thus most significant for large bodies and at high densities. The fourth effect is the fact that for a large gas cap thickness, the gas may no longer be optically thin. When the total radiation intensity of an optically thin gas exceeds 10% of the black body value, it is necessary to consider re-absorption in the gas.¹²

The total radiative flux to a body is the sum of the integrated non-equilibrium radiation and the equilibrium flux. Equilibrium radiation from air in the temperature and density range of interest to Apollo velocities, varies approximately as the 1.7 power of the density. Non-equilibrium radiation, however, is invariant with density due to binary scaling. The body size effects equilibrium intensity by changing the thickness of the radiating layer but has no effect on the non-equilibrium contribution. Thus, at low densities, i. e., high altitudes, and small body sizes, a level should be reached where the non-equilibrium radiation exceeds the equilibrium value. Because of the differences in the density and size dependence of the two sources of radiation discussed above, the density at which equilibrium and non-equilibrium radiation intensities are equal will vary with scale.

At high altitudes a point is reached for a given nose radius where truncation of the radiation profile occurs, i. e., where a characteristic distance such as the shock detachment distance, is smaller than the distance necessary for the gas to relax to equilibrium behind the shock front. If the ambient density where this occurs is low enough (i. e., large nose radii), there will be a "luminous front plateau" extending between this altitude and the altitude at which the non-equilibrium intensity became the dominant contribution. Over this altitude range the integrated radiation intensity remains constant despite the fact that the thickness of the non-equilibrium region varies. For small nose radii this "luminous front plateau" will cover a smaller density range since this "truncation" starts to occur at high densities. Truncation decreases the total integrated non-equilibrium radiation quite slowly at first, but when it reaches a point where the characteristic distance is equal to the distance to the radiation peak, the integrated radiation will fall off more rapidly, approximately as the square of the density as a consequence of the binary scaling behavior of the radiation profile.

A fall-off in the luminous front plateau is also to be expected at low densities due to "collision limiting" which vitiates the binary scaling near the shock front. Collision limiting for a large body would cause the integrated radiation intensity to vary linearly with density, whereas severe

~~CONFIDENTIAL~~

~~CONFIDENTIAL~~

truncation of a binary scaled region would introduce a density squared dependence.

At present no adequate theory exists which enables us to make accurate calculations of the luminous front radiation. However, by using general principles in conjunction with present experiments at appropriate velocities, good estimates of the radiation heat fluxes for lunar re-entry velocities can be made. By the use of an electrically powered shock tube¹³ normal shocks have been produced at higher than escape velocity. The information reported in this study was obtained primarily by use of this device, although much of our understanding of the luminous front has been obtained from the study of lower speed shock fronts in pure gases^{14,15} as well as in air.^{9,5}

This report will cover both the experimental and theoretical phases of the work on the non-equilibrium radiation problem in the 35,000 ft/sec speed range. Using the electric arc-driven shock tube to produce shocks of this velocity the major part of the experimental data were obtained by photometry with a calibrated monochromator and photomultipliers. Vacuum ultraviolet and an integrated radiation measurements were taken with a tungsten photoelectric gauge and a carbon heat transfer gauge respectively. These measurements are summarized in this report, compared to the data available from the NASA Ames Research Laboratory and their significance is discussed. An empirical calculation scheme for the non-equilibrium radiation is developed and is incorporated into a flow field calculation for an Apollo re-entry vehicle.

~~CONFIDENTIAL~~

CONFIDENTIAL

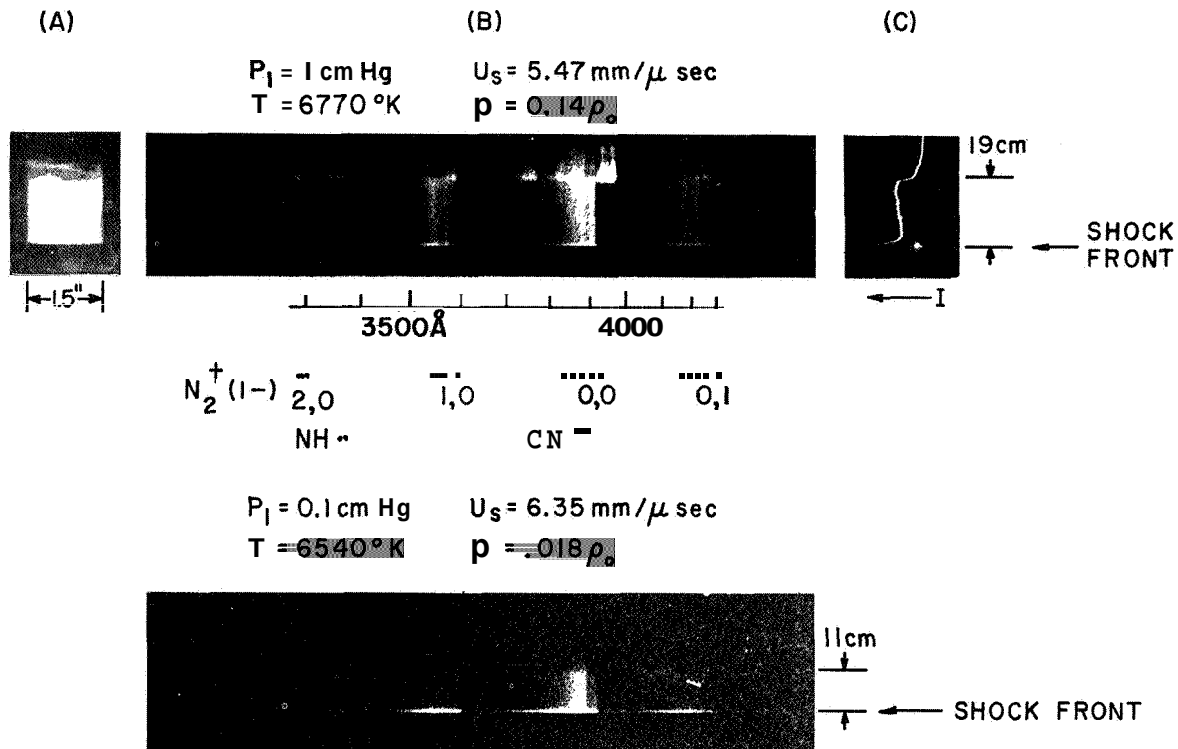


Fig. 1 (A) Time resolved photograph of normal shocks in nitrogen.

(B) Race track spectrograms of shock waves in nitrogen. The overshoot and equilibrium radiation of the $N_2^+(1-)$ radiation is clearly identified.

(C) Oscillogram record of radiation observed in the .55 - 1.0 μ region showing the radiative overshoot and relatively flat equilibrium region. All pictures on the top line are scaled to the same shock thickness.

CONFIDENTIAL

II. ELECTRIC ARC-DRIVEN SHOCK TUBE

Normal shock waves with speeds up to satellite velocities have been produced for a number of years in combustion-driven shock tubes.¹⁶ These shock tubes have proved invaluable in accurately simulating gaseous phenomena occurring during missile and satellite re-entry into the earth's atmosphere. Accurate simulation of the phenomena produced by the re-entry of space probes at escape velocities, however, is beyond the capabilities of conventional combustion-driven shock tubes. Magnetically driven shock tubes such as the MAST¹⁷ and others can produce shock speeds of up to many times escape velocity, but in these devices the shocked gas is subjected to large electric and magnetic fields. These fields are of large enough intensity that they may seriously alter the shock heated gases from the pure one-dimensional, steady, thermodynamic equilibrium state desired.

A schematic diagram of an electric arc-driven shock tube used to achieve the present data is presented in Fig. 2. A photograph viewing the driver end of the shock tube is shown in Fig. 3. The driver section is made of 1 1/2-inch inside diameter stainless steel tubing lined with a 3/32-inch-thick teflon insulator. The driver is separated from the low pressure test gas section by a conventional stainless steel diaphragm which is also used as an electrode. The other end of the driver is closed with a copper electrode which is supported by a nylon insulator. An aluminum wire, .002 inch in diameter, is stretched between a hole in the center of the copper electrode and the diaphragm end of the driver. The capacitor bank used with this shock tube consists of 264 capacitors, each having a capacitance of 1 microfarad and a voltage rating of 20 KV. The capacitors are assembled on a cart and each capacitor is connected to collector plates by a coaxial cable. The ground plate is connected to the driver body. The high voltage terminal is connected to the copper electrode through a lovotron switch mounted on the high voltage plate.

For a typical run, the driver is evacuated and then filled with helium to a pressure of 200 psi. The capacitor bank is charged to 18 KV. By energizing the lovotron switch, the capacitor bank is connected directly across the driver electrodes. The starter wire explodes and initiates an arc in the helium. The capacitor bank discharges through the helium in about 40 μ secs, heating it to a high temperature. The diaphragm-electrode breaks approximately when the helium has reached its peak temperature and pressure, approximately 20,000°K and 10,000 psi, and the driver gas expands into the low-pressure air test section, driving a shock wave before it. The details regarding the operation and performance of this device have been thoroughly described by Camm and Rose.¹³

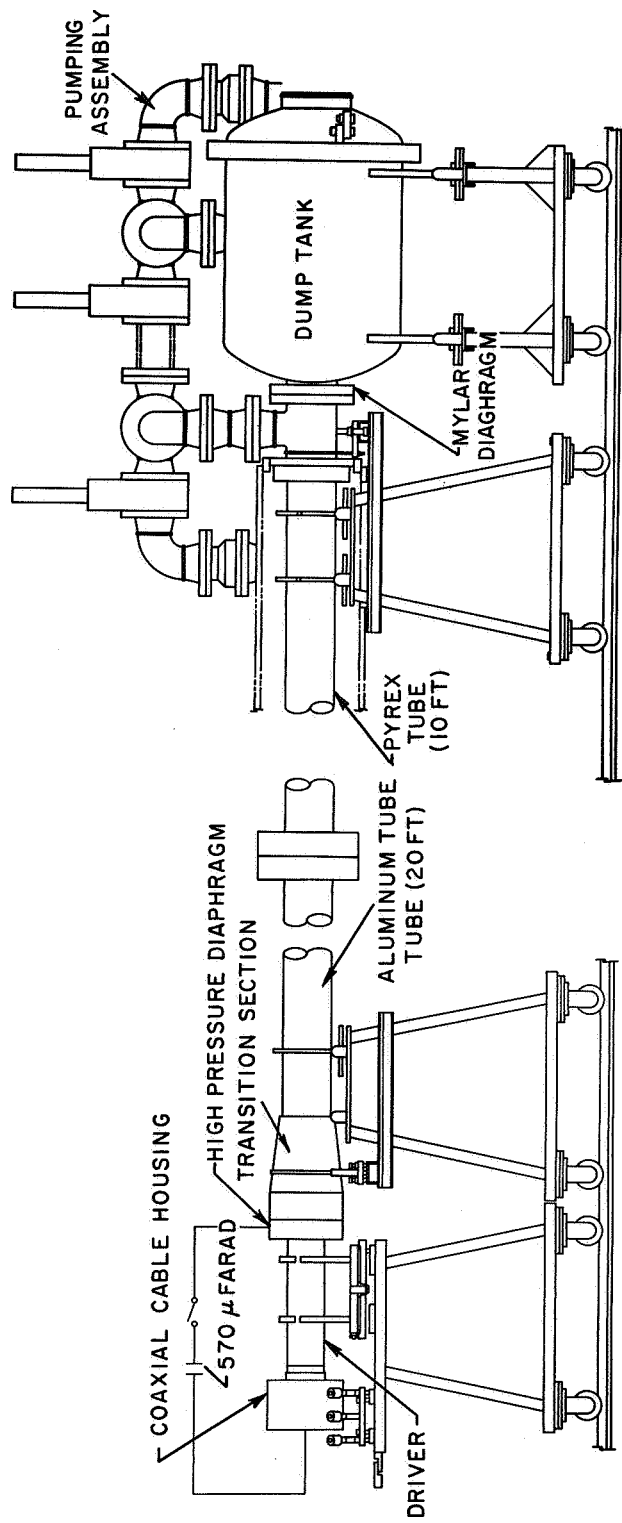


Fig. 2 Schematic diagram of typical arc-driven shock tube (Tube "B").
This shock tube is identical to a combustion-driven shock tube
except for the method of energy addition in the driver.

~~CONFIDENTIAL~~

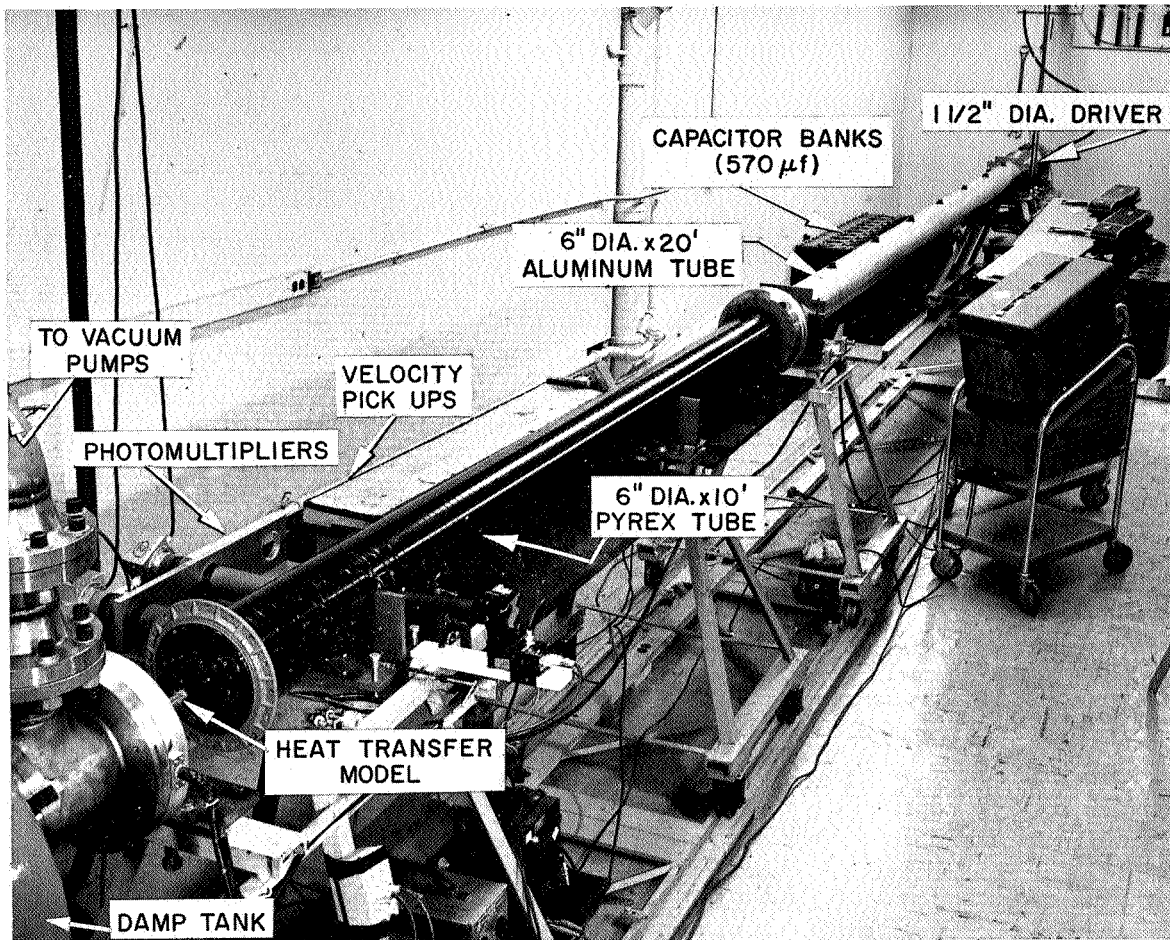


Fig. 3 Photograph of an arc-driven shock tube.

~~CONFIDENTIAL~~

~~CONFIDENTIAL~~

THIS PAGE IS BLANK

~~CONFIDENTIAL~~

111. MONOCHROMATOR MEASUREMENTS

A. Monochromator Measurements (.24 - .90 μ Wavelength Region)

Photometric measurements were made using a dual channel Bausch and Lomb grating monochromator having quartz optics. The arrangement of the equipment was identical to that described by Allen, Camm and Keck.¹⁸ The monochromator was equipped with three photomultipliers; two of these measured the radiation intensity in two adjacent narrow wavelength bands selected by the monochromator and the third monitored a fraction of the total radiation passing through the entrance slit.

The outputs of the photomultipliers were fed directly to Tektronix 545 oscilloscopes equipped with 53K/54K preamplifiers. A typical photomultiplier record is shown in Fig. 4. The initial pressure was 0.1 mm Hg, and shock velocity 33,000 ft/sec (10 mm/ μ s). The measurement shown was made in the .55 - 1.0 μ wavelength region. The time resolution of the optical system used is approximately 0.1 μ sec. This resolution was achieved by using a 0.5 mm width monochromator entrance slit in conjunction with appropriate stops. The radiation profiles in Fig. 4 also show steady state conditions after the initial overshoot shock is interpreted as the equilibrium radiation levels. The measurements were made looking through quartz ports mounted in copper knife edges which protruded into the center of the shock tube to eliminate boundary layer effects along the shock tube walls and shock curvature as described by Lin.¹⁹

Calibration of the complete optical train including the appropriate filters to prevent overlapping of orders was made using both a standard tungsten ribbon filament lamp and a graphite arc. The brightness temperature of the standard lamp was given as a function of lamp current at a wavelength of .653 μ by the National Bureau of Standards. The spectral intensity of the lamp at other wavelengths was calculated using data on the emissivity of tungsten given by DeVos²⁰ and the transmission of the quartz window. The arc was used to calibrate at shorter wavelengths. Data on the true temperature and spectral emissivity of such arcs has been given by Euler.²¹ In the region of overlap between the tungsten lamp and the arc, the two methods of calibration agree within 20% or better. The wavelength scale of the monochromator was calibrated with a mercury lamp. The error in setting the monochromator is estimated to be about $\pm 5 \text{ \AA}$.

Figure 5 shows an oscillogram of typical radiation profiles at various wavelengths. The top trace is of the monitor channel (.55 - 1.0 μ), the bottom trace is observing radiation between .4 μ and .42 μ . The initial pressure for these three experiments was 0.1 mm Hg. The radiative overshoot and the equilibrium level behind the relaxation region are clearly seen in the profiles. The slight rise in equilibrium radiation as one moves away from the shock

~~CONFIDENTIAL~~

front has been attributed to effects of attenuation of the shock velocity as it moves down the tube.⁵²

B. Monochromator Measurements (1.9 μ Wavelength Region)

Photometric measurements at a wavelength of 1.9 μ were made using a single channel Perkin-Elmer infrared spectrophotometer. For these measurements, it was necessary to obtain a separate wavelength calibration for the monochromator and prism. In the infrared portion of the spectrum, beyond wavelengths of 2 μ , there are few atomic emission lines that can be used for calibration as was done in the visible part of the spectrum. Therefore, one must resort to the use of the absorption bands of molecules, as discussed by Taylor.²²

To obtain absolute intensities of the emitting gas from these measurements, it was necessary to calibrate the infrared detector against a standard source. In this experiment a steel cavity black body operating at 1000°K was used. The calibration was carried out with the same geometrical arrangement as used in the shock tube runs, i. e., the radiation standard replaced the radiating gas. The detector, monochromator, and shock tube optics were calibrated as a unit. Thus, any corrections for reflections in the optics or for atmospheric absorption were included in the calibration.

C. Equilibrium Radiation Measurements

The approximate ranges of velocity and density for which radiation measurements have been made in conventional shock tubes is shown by the crosshatched area (A) in Fig. 6. The figure shows the equilibrium radiation flux from air at the stagnation conditions as a function of flight velocity and altitude.^{3,6} The 24-inch diameter shock tube¹⁹ permits operation of a shock tube at initial pressures of 0.02 mm Hg, extending the range accessible to luminous front experiments as shown by the area (B). The electric shock tube¹³ has allowed us to extend our measurements into Region (C).

Data on the equilibrium intensity of radiation for normal air shocks at 33,000 ft/sec at an initial pressure of 0.1 mm Hg are shown in Fig. 7. The measurements cover a wavelength range from 0.25 to 2.0 microns. Measurements at shorter wavelengths are difficult because of the reduced intensity from the arc calibration source and also the enhancement of scattered light at these shorter wavelengths. All the experimental data were obtained at the same shock speed, within 3%, producing an equilibrium temperature of 9,650°K. In each experiment two measurements were made in adjacent monochromator channels -- one represented by the solid triangles in Fig. 7, and the other by the open circles. Short lines have been used to connect the two intensity measurements obtained for each run.

Between 0.25 and 0.9 μ the wavelength resolution of both monochromator channels was .02 μ . The two measurements at 1.0 μ were obtained with the Perkin-Elmer prism spectrophotometer and a gold doped germanium infra red cell having a wavelength resolution of 0.1 μ . The theoretical curves

~~CONFIDENTIAL~~

were constructed using published values of oscillator strength, f numbers for the various radiating systems.^{10,18} The important molecular radiating systems under these conditions, the f numbers and the appropriate references are as follows:

<u>System</u>	<u>f number</u>	<u>Reference</u>
N_2 (2+)	.09	10
N_2^+ (1-)	.09	18

The NO β and γ and the N_2 (1+) systems contribute relatively little at the equilibrium conditions of the test discussed here. Atomic nitrogen lines are identified in the region between .5 and .9 microns, however, as yet we are not in a position to construct a theoretical line for this source of radiation. The contribution from these atomic lines has not been included in the various tables of radiation^{6,23,24} used and it is clear from the data shown here that this source of radiation is important.

The Kramer's radiation produced by the recombination of electrons and ionized nitrogen atoms should also be a major contribution to the continuum radiation under the equilibrium conditions of these measurements, i. e. , at shock velocities of 33,000 ft/sec. The dashed line in Fig. 7 was calculated from the data of Kivel and Bailey⁶ for this source of radiation. This calculation is an approximation and does not take into account the fine structure of this type of radiation at the shorter wavelengths. This fine structure is produced by the capture of free electrons by the ionized atom to the various electronic sublevels in the atom. Lindenmeier²⁵ has calculated the details of this fine structure. Application of this calculation and use of an effective nuclear charge, Z , of the singly ionized nitrogen atom of 0.6 is also shown in Fig. 7. The value of 0.6 for the effective nuclear charge was chosen to maintain the theoretical curve for this source of radiation below any radiation observed experimentally. The accuracy of this value for the effective nuclear charge is strongly dependent upon an accurate knowledge of the degree of ionization in the gas. The degree of ionization of the gas under the experimental conditions of the test was about 10%, as inferred from the shock velocity measurement and the equilibrium constants of the gas.^{26,27} A much better measurement of Kramer's radiation could be performed by obtaining radiation measurements in a more highly ionized gas sample, where the uncertainty about the degree of ionization is greatly reduced.

The velocity and density dependence of the equilibrium radiation measurements are shown in Fig. 8. Several representative wavelength regions were chosen and data was obtained at various velocities and densities. Theoretical curves were again constructed for the important radiating species. No theoretical line was constructed in Fig. 8 (E) because the measurements in this wavelength region were integrated over a large wavelength interval and hence were not very well calibrated. The data in this figure show a good overlap with conventional and combustion driven shock tube results. The data also show a steep velocity dependence at the higher velocities which can be attributed mainly to atomic line radiation.

~~CONFIDENTIAL~~

Interesting conclusions can be drawn from the equilibrium measurements obtained in the wavelength region $1.85 - 1.95\mu$. These measurements were obtained with the Perkin-Elmer photospectrometer and show no radiative overshoot, although an equilibrium level is present. Quantitative results of this equilibrium radiation obtained from normal air shocks at initial pressures of 0.1 mm Hg are plotted against shock velocity in Fig. 9. When these measurements were first observed, it was felt that the main radiation contributor in this region should be Kramer's radiation. When further measurements were obtained it was evident from the velocity dependence that some other contributors must be present which are important at the lower velocities. A theoretical curve for the nitrogen free-bound radiation was constructed using the effective nuclear charge, Z of 0.6, as inferred from the equilibrium measurements shown in Fig. 7. Also plotted are the other Kramer's radiation contributors from Kivel and Bailey.⁶ If one assumes that there is an unknown radiator in this wavelength region and that the radiation is produced by an N_2^+ ion, and that a transition to the ground state is involved, one can arrive at a velocity dependence of the radiation which fits the data fairly well. The Meinel bands of N_2^+ is a transition from the A to the X electronic states of the N_2^+ ion and hence is a likely candidate for this unknown contributor to the equilibrium radiation at a wavelength of 1.9μ . Further investigation is obviously needed to further test this hypothesis.

D. Non-Equilibrium Radiation

Measurements of the non-equilibrium radiation were made by detailed examination of radiation profiles such as those shown in Figs. 4 and 5. Integrated total non-equilibrium radiation was obtained from integration of the area under the luminous front profile. The point where the radiation intensity had fallen to a level 10% above the equilibrium level was used to define the width of the non-equilibrium regions. This distance, called $d_{0.1}$, was obtained by multiplying the observed time to this equilibrium plus 10% value, by the incident shock speed. When this integration is to convert from the laboratory fixed coordinate system to particle time carried out, the usual units in which radiation intensity measurements are made, i.e., watts/cm³ - ster - μ , become watts/cm² - ster - μ . The data is further adjusted by multiplying through by 2π steradians to give the integrated luminous front radiation intensity from one side of an infinite slab with the measured profile. Measurements from one condition of shock speed and initial pressure, i.e., 33,000 ft/sec and 0.1 mm Hg, are shown as a function of wavelength in Fig. 10. The wavelength region covered by the monochromator and photomultipliers extended from 0.21μ to 2.0μ . The measurements plotted at a wavelength of 0.1μ were obtained with a photoelectric gauge and will be discussed in a later section.

A value of the total, integrated luminous front radiation can be obtained from this graph by determining the area encompassed by the data points. A dashed line was drawn as an upper edge of an envelope including all the data points. The area under this dashed curve is $40 \text{ watts/cm}^2 - 2\pi - \text{ster}$. In regions where the least measurements are available and where large contributions could originate, the dashed line was drawn in purposely high. Atomic lines are noticed to contribute appreciably to the integrated

~~CONFIDENTIAL~~

non-equilibrium radiation. Efforts are presently in progress to obtain detailed spectra of these lines. The absolute intensities of the radiation at the time of radiation peak at various wavelengths are shown in Fig. 11. The units of intensity in this figure are the same as those of the equilibrium measurements, Fig. 7, i.e., in units of $\text{watts/cm}^3 \cdot \text{ster} \cdot \mu$. This figure demonstrates that the atomic lines are prominent in the non-equilibrium as well as the equilibrium regions. The ratios of intensity at the non-equilibrium peak, I_P , to the equilibrium intensity, I_P/I_e is shown as a function of wavelength in Fig. 12. The average peak to equilibrium ratio at this shock strength, 33,000 ft/sec at an initial pressure of 0.1 mm Hg of air, is approximately four. There was no overshoot observed at the wavelength of 1.9 microns. Other conclusions drawn from this figure are that the atomic line radiation overshoots and that the overshoot of the $\text{N}_2^+(1-)$ system is low relative to other wavelengths. This is not completely unexpected since the activation energy of this system is relatively small compared to other molecular radiators, and secondly, since nitrogen ions must first be produced in the non-equilibrium region before any radiation from this system can be observed, it may well have a longer excitation time than the molecular bands.

As in the case of the equilibrium radiation, the velocity and density dependence of the radiation at representative wavelengths was obtained. This data is presented in Fig. 13 for initial pressures varying from 0.05 to 1.0 mm Hg. If binary mechanisms dominate and there is no collision limiting in the non-equilibrium region, the integrated luminous front radiation should be independent of density. This fact is reasonably well borne out by data presented in this figure.

Although the integrated luminous front radiation is the most important experimental observation, other valuable information has been obtained from these experiments. The thickness of the non-equilibrium region behind a normal shock front is of particular importance since in some applications it influences the relative magnitudes of the equilibrium and non-equilibrium radiative heating. When the ambient density is sufficiently high, the thickness of the non-equilibrium region behind the shock will be small compared with the shock stand-off distance and most of the gas cap will be in thermodynamic equilibrium. As the density is reduced, the luminous front thickness increases, and less of the gas cap will be in equilibrium. At sufficiently low density the equilibrium region vanishes, and at still lower densities the luminous front profile becomes "truncated." If the density is reduced further, a condition will be reached where the body intersects the non-equilibrium radiation profile at the point of peak radiation. When this condition is reached the integrated non-equilibrium radiation will fall off as the square of the density, one power is due to the increased width of the reaction zone and one for the decreased intensity due to fewer collisions. We refer to this effect as "severe truncation." The present shock tube measurements have enabled us to obtain information regarding these phenomena. The time required for the luminous front intensity to fall to a level 10% above the equilibrium value has been defined as a measure of the non-equilibrium distance. The time to this level, called $t_{0.1}$ is measured in the laboratory coordinate system. The distance to this level in the particle fixed coordinate system is obtained by multiplication by the shock velocity, i.e., $d_{0.1} = t_{0.1} U_s$.

In like manner, the distance to the peak radiation, d_p is $U_s t_p$, where t_p is the time to peak radiation. Values of $t_{0.1}$ and t_p are presented as functions of shock velocity in Figs. 14 and 15. Measurements made at different initial pressures are presented here on a single plot whose ordinate is the product of pressure and time, i. e., $P_1 t$. This product should be approximately independent of initial pressure in a binary regime. The dashed line in Fig. 15 represents a lower limit of the time to reach the radiation peak and was calculated assuming a gas kinetic cross-section of $5 \times 10^{-15} \text{ cm}^2$.

Over the small range of initial pressures covered by these experiments, a single curve could be drawn through each of the two sets of data (the solid and dashed lines in Fig. 14). From these two curves, non-equilibrium distance, $d_{0.1} = U_s t_{0.1}$ and peak radiation distance, $d_p = U_s t_p$, were calculated as shown in Fig. 16 for various shock velocities. The region covered by the present experiments is indicated on the graph for the $d_{0.1}$ values. It should be recognized that Fig. 16 is an empirical curve which may not be valid at pressures significantly different from those covered by the experiments. Nevertheless, when used with proper caution, Fig. 16 provides useful information for estimating the onset of "truncation" and "severe truncation" in hypersonic flight situations in ballistic ranges.

E. Collision Limiting Experiment

An experiment has been performed to determine the density at which various radiative band systems of shock heated air become collision limited.¹⁰ Since the results are easier to interpret in a pure gas, data have been collected on the N_2^+ first negative (3900 - 3925Å) and N_2 first positive (5000 - 10,000Å) band systems in pure nitrogen. A range of initial pressures of 20 - 500 μ Hg and shock velocities of 4.5 - 7.0 mm/ μ sec have been covered.

Analysis of the radiation profiles in the shock front indicates that the binary scaling law begins to break down at the lower initial pressures used in these experiments. Before collision limiting is effective, the kinetic processes responsible for the radiation overshoot involve only binary collisions. Therefore, the intensity of radiation overshoot is expected to be proportional to density while the duration of the overshoot should be inversely proportional to density.⁸ To check this binary scaling for the N_2^+ first negative band, two radiation profiles in nitrogen taken at the same shock velocity but at initial pressures of 100 and 200 μ Hg have been plotted in Fig. 17 using the binary scaling law. The two profiles practically coincide. However, in Fig. 18 four radiation profiles at lower densities, two at 100 μ and two at 20 μ Hg, plotted in a similar manner, do not scale in a binary fashion.

The lack of binary scaling of the data between 100 and 20 μ Hg initial pressure has been ascribed to collision limiting. If the assumption is made that all the atomic and molecular species in the gas are effective in deactivating the excited electronic state of the N_2^+ first negative system, then a collisional deactivation cross-section greater than $3 \times 10^{-14} \text{ cm}^2$ can be calculated from this data.

~~CONFIDENTIAL~~

Further analysis of the parameters characterizing the radiation profile must be carried out to ascertain, if possible, whether the effect observed was indeed due to collision limiting of the excited electronic state. The range of initial pressure covered by this experiment must be extended to higher pressures to check that the binary scaling law holds into a pressure range where collision limiting can definitely be eliminated as a phenomenon. This higher pressure data should also allow comparison with other data previously obtained. Because of these uncertainties, the results shown are of a preliminary nature and further experiments are needed to explore the collision limiting effect.

~~CONFIDENTIAL~~

CONFIDENTIAL

5000A - 10,000A Region

$P_1 = 0.1 \text{ mm Hg}$

$u_s = 33,000 \text{ ft/sec}$

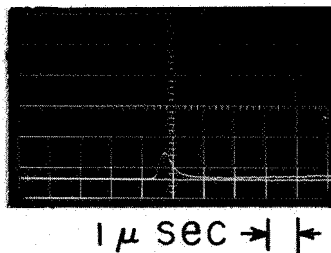


Fig. 4 Oscillogram of the nitrogen first positive radiation behind a normal shock in air in the electric shock tube. The wavelength region is $.55 - 1.0\mu$. $u_s = 33,000 \text{ ft/sec}$. $P_1 = 0.1 \text{ mm Hg}$.

NORMAL AIR SHOCKS

$P_1 = 0.1 \text{ mm Hg}$

TOP TRACE $[.55 - 1.0\mu]$

BOTTOM TRACE $[.40 - .42\mu]$

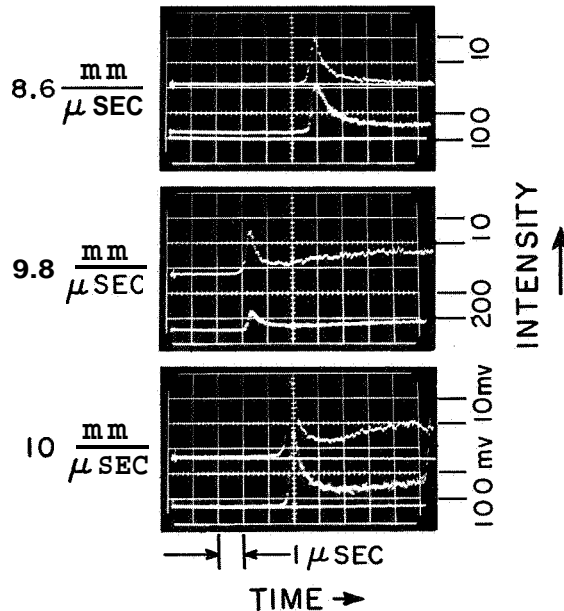


Fig. 5 Oscillogram records of radiation behind normal shocks in air at various shock velocities. The wavelength region of the upper traces is $.55 - 1.0\mu$. The bottom $.40 - .42\mu$.

CONFIDENTIAL

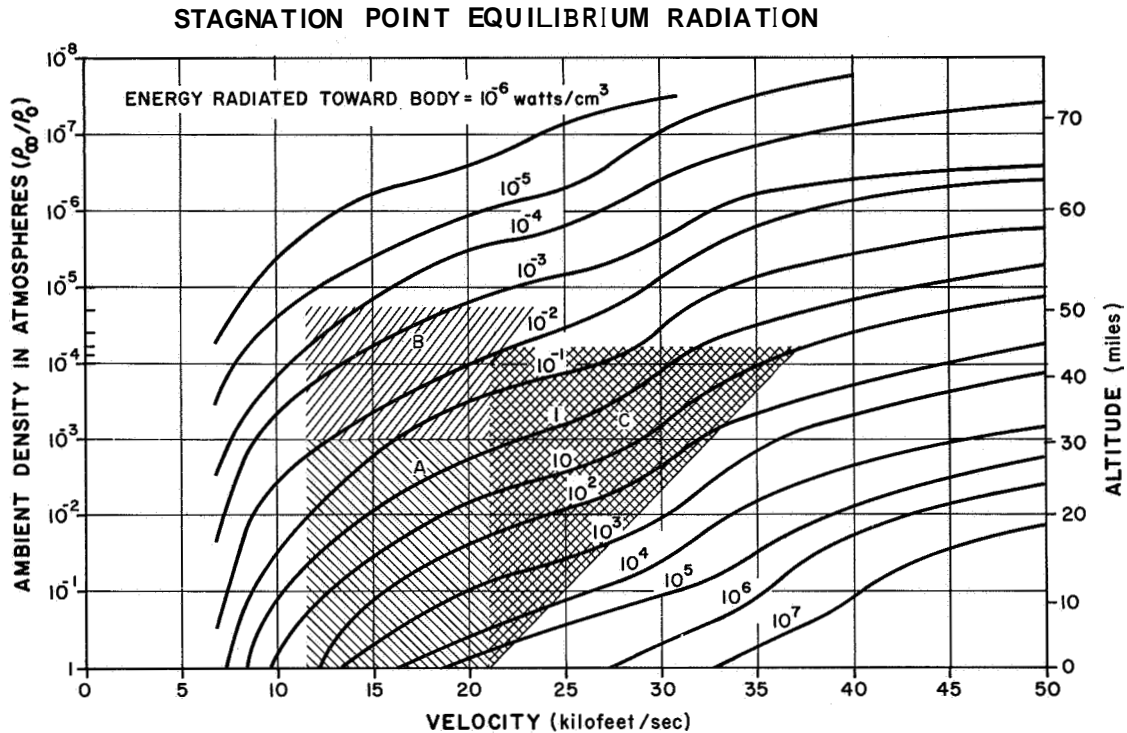


Fig. 6 Approximate operating regions for shock tube radiation measurements in terms of shock velocity and ambient air density.

- (A) Conventional combustion-driven shock tubes.
- (B) 24-in. low density shock tube.
- (C) Electrically-driven shock tube.

The contours show one-half ($2\pi \bar{I}$) of the emitted radiation energy per unit volume from the stagnation region for fully equilibrated air. For an optically thin gas, this represents an energy flux towards the stagnation point in w/cm² per unit thickness of gas cap.

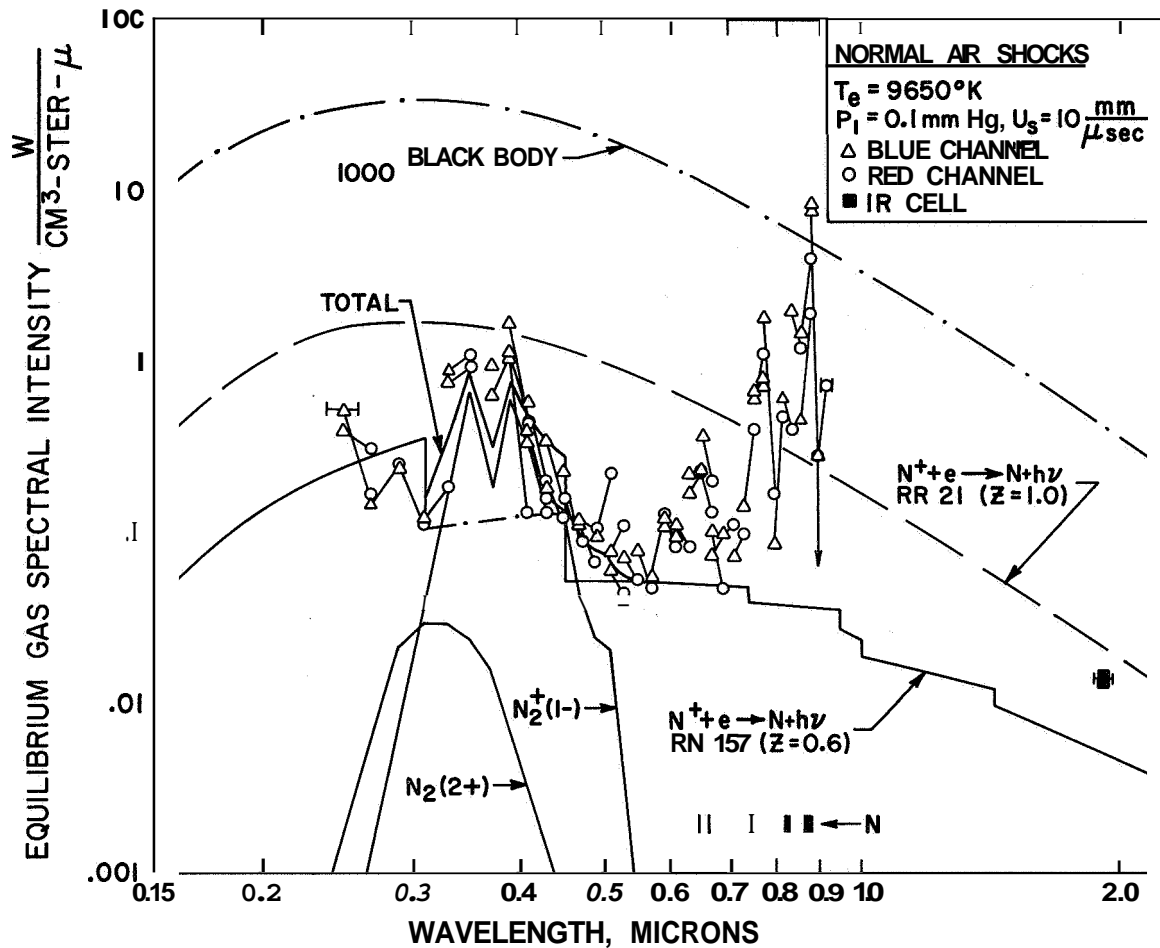


Fig. 7 Equilibrium radiation measurements behind normal air shocks versus wavelength.

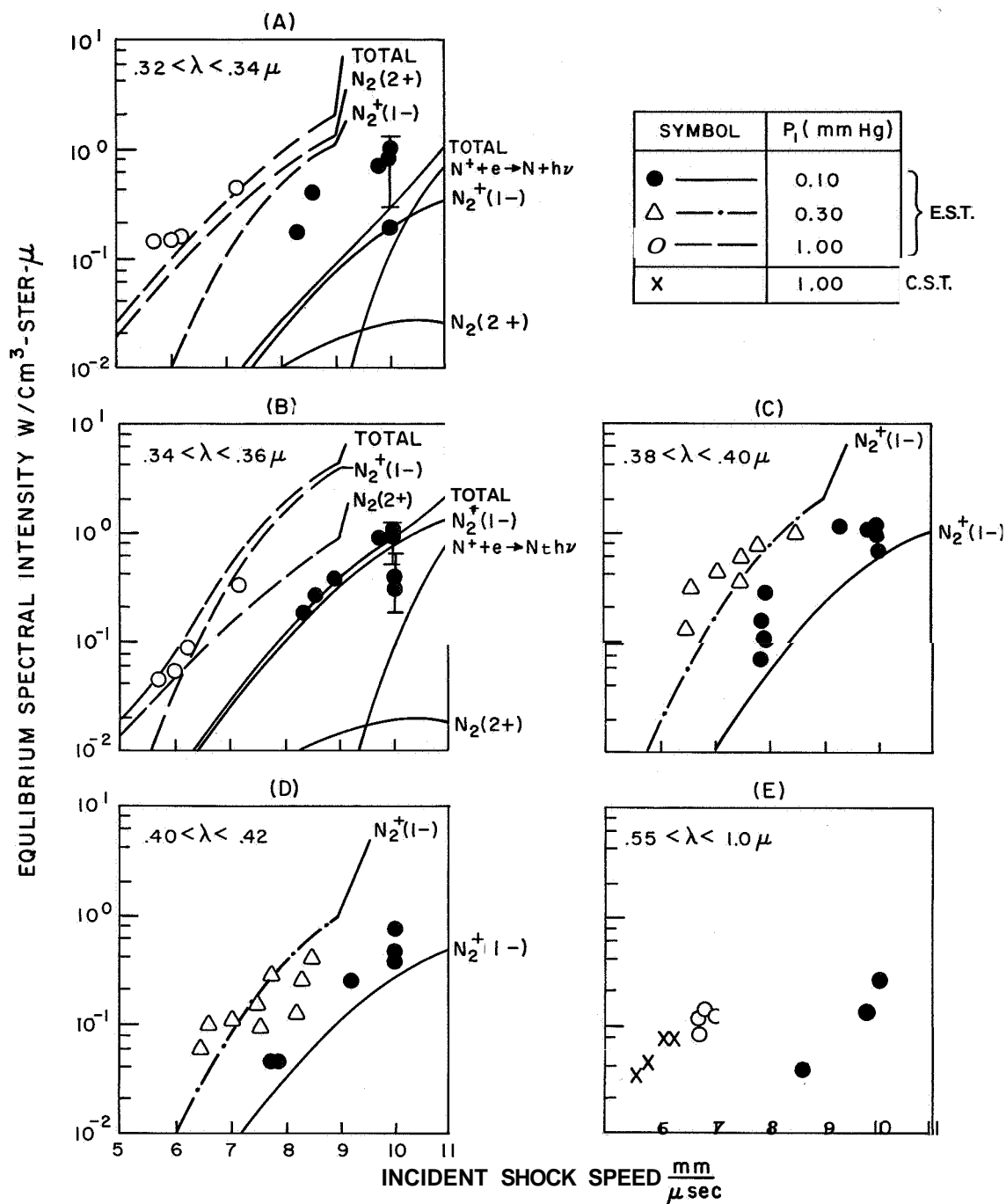


Fig. 8 Equilibrium radiation measurements behind normal air shocks at various initial pressures and shock velocities. Sets of measurements were made in the indicated wavelength intervals. Theory curves are constructed using published values for f numbers.

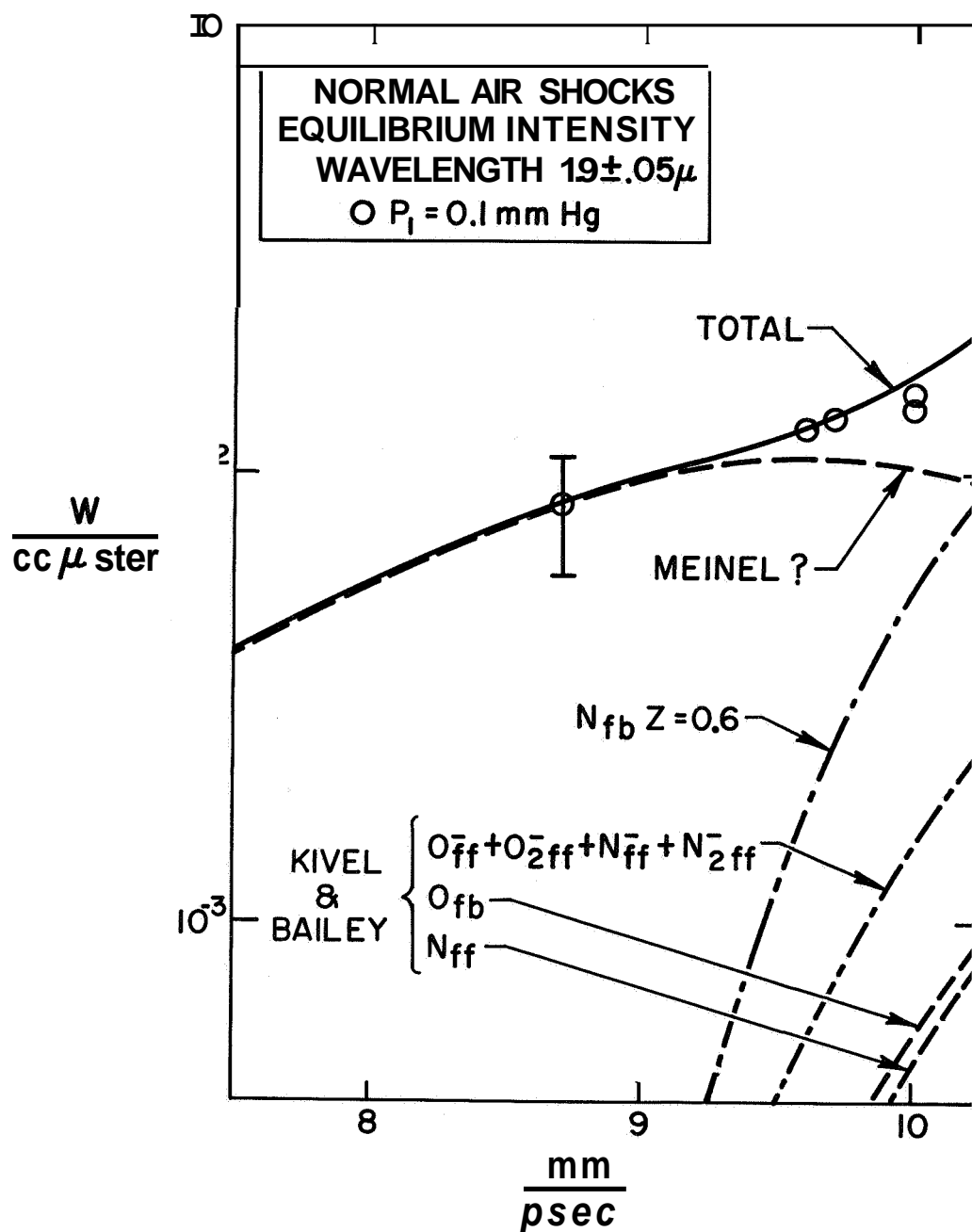


Fig. 9 Equilibrium radiation measurements, at a wavelength of 1.9μ , behind normal air shocks, initial pressure, 0.1 mm Hg. The theory lines are discussed in the text.

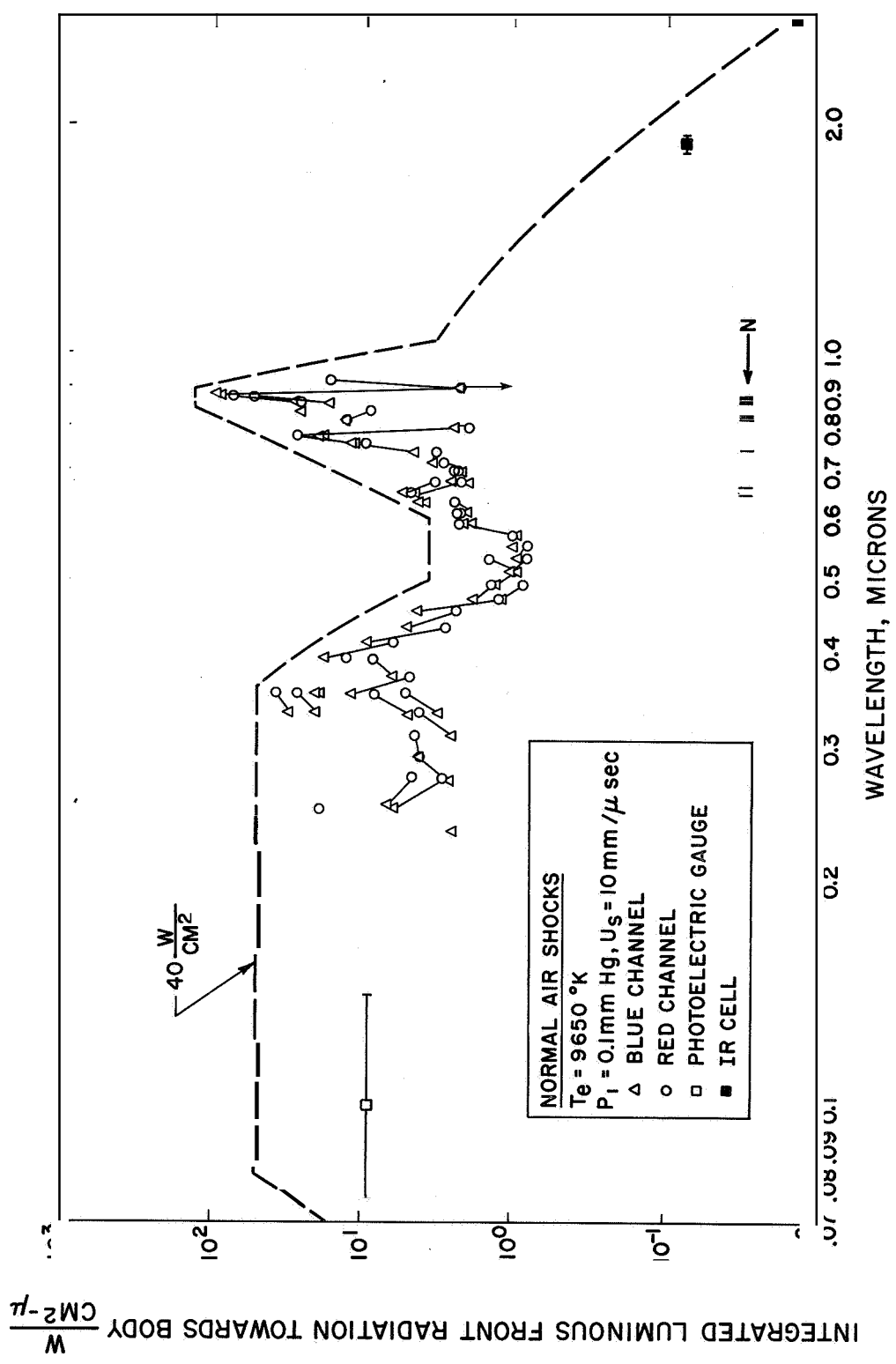


Fig. 10 Non-equilibrium radiation measurements of normal air shocks versus wavelength. The shock conditions are $U_s = 10 \text{ mm}/\mu \text{ sec}$, $P_1 = 0.1 \text{ mm Hg}$. The area under the dashed curve is $40 \text{ watts}/\text{cm}^2 - 2\pi \text{ ster.}$

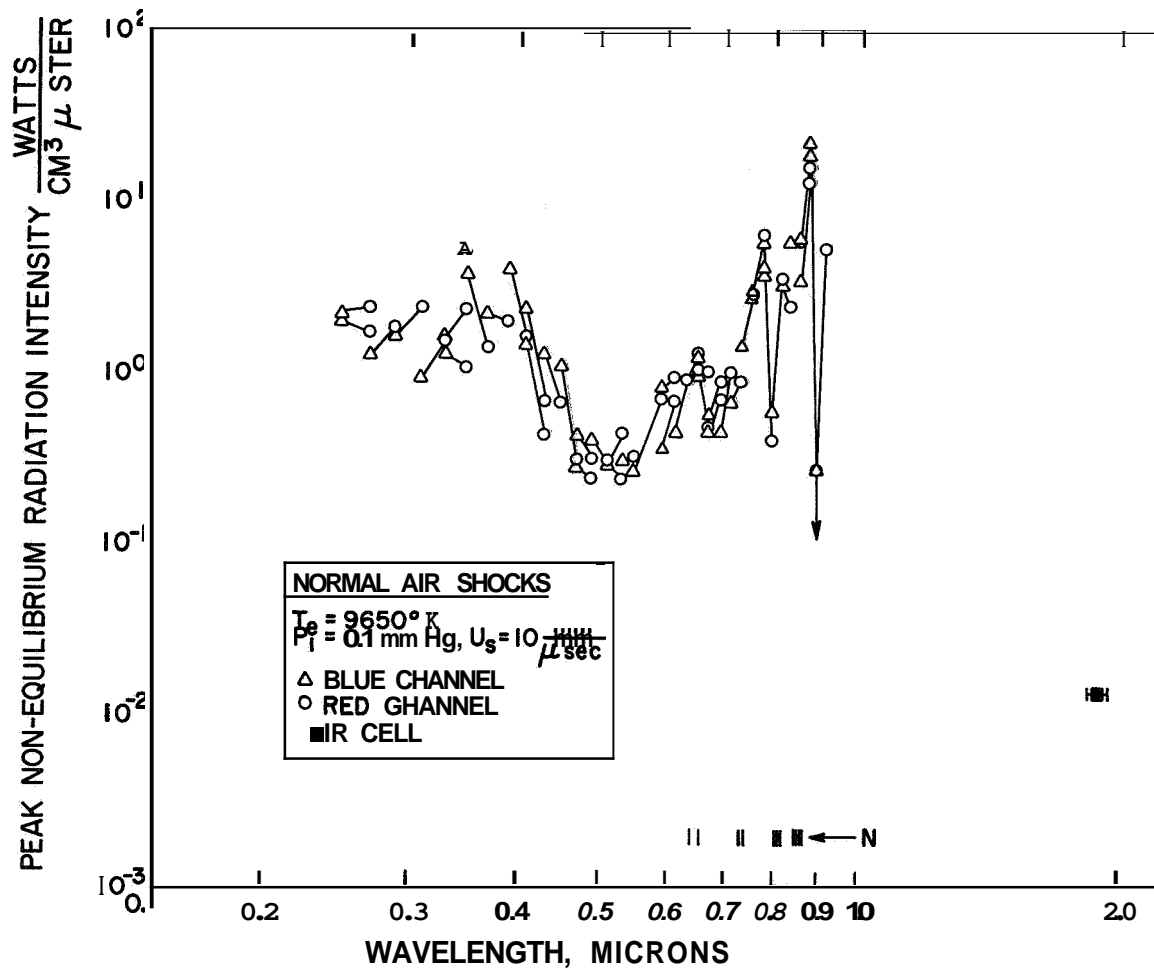


Fig. 11 Absolute intensity measurements versus wavelength at the time of peak radiation. The shock conditions are 10 mm/μ sec, R = 0.1 mm Hg.

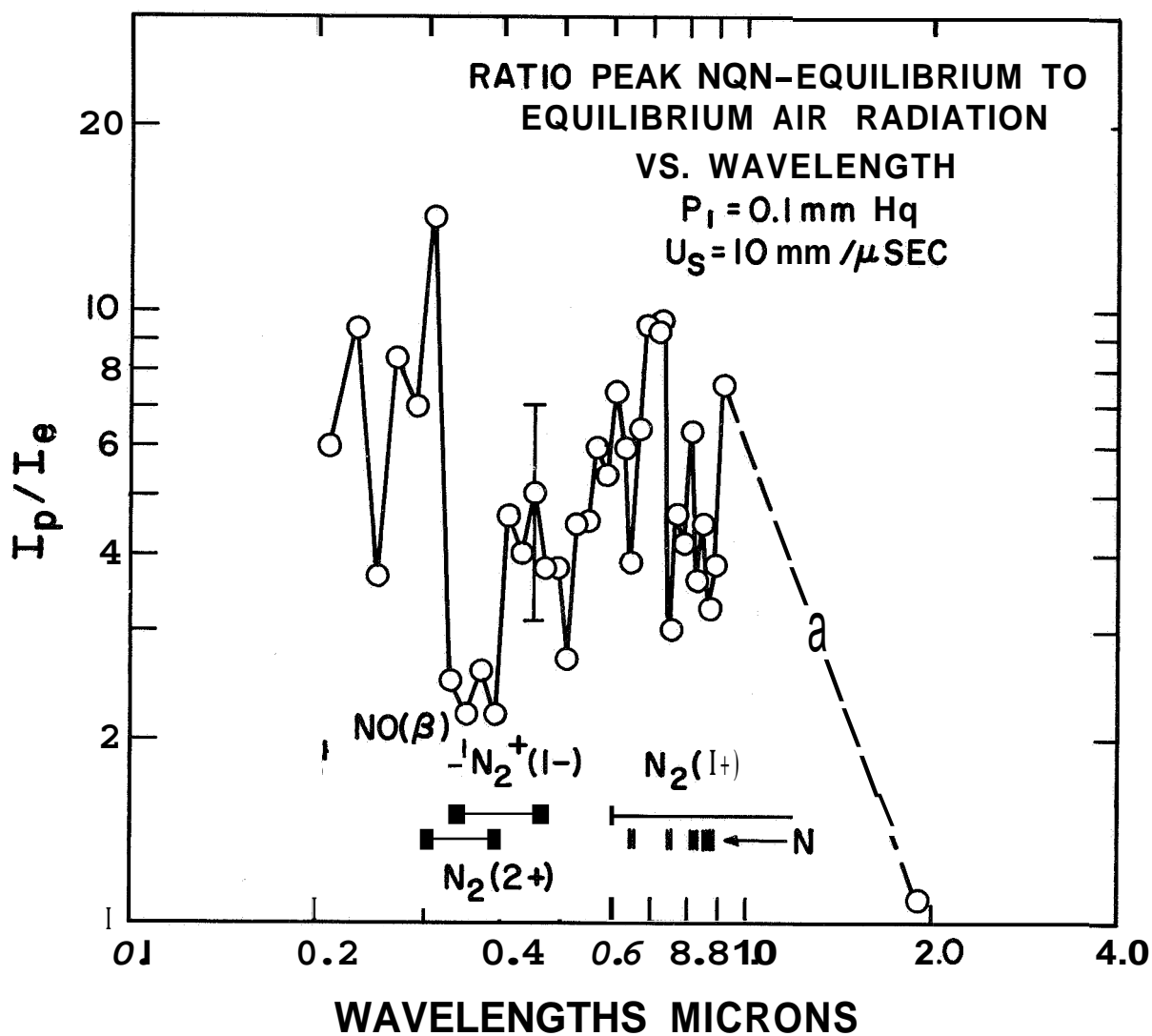


Fig. 12 Ratio of peak non-equilibrium to equilibrium radiation versus wavelength. The shock conditions are $10 \text{ mm}/\mu \text{ sec}$, $P_1 = 0.1 \text{ mm Hg}$.

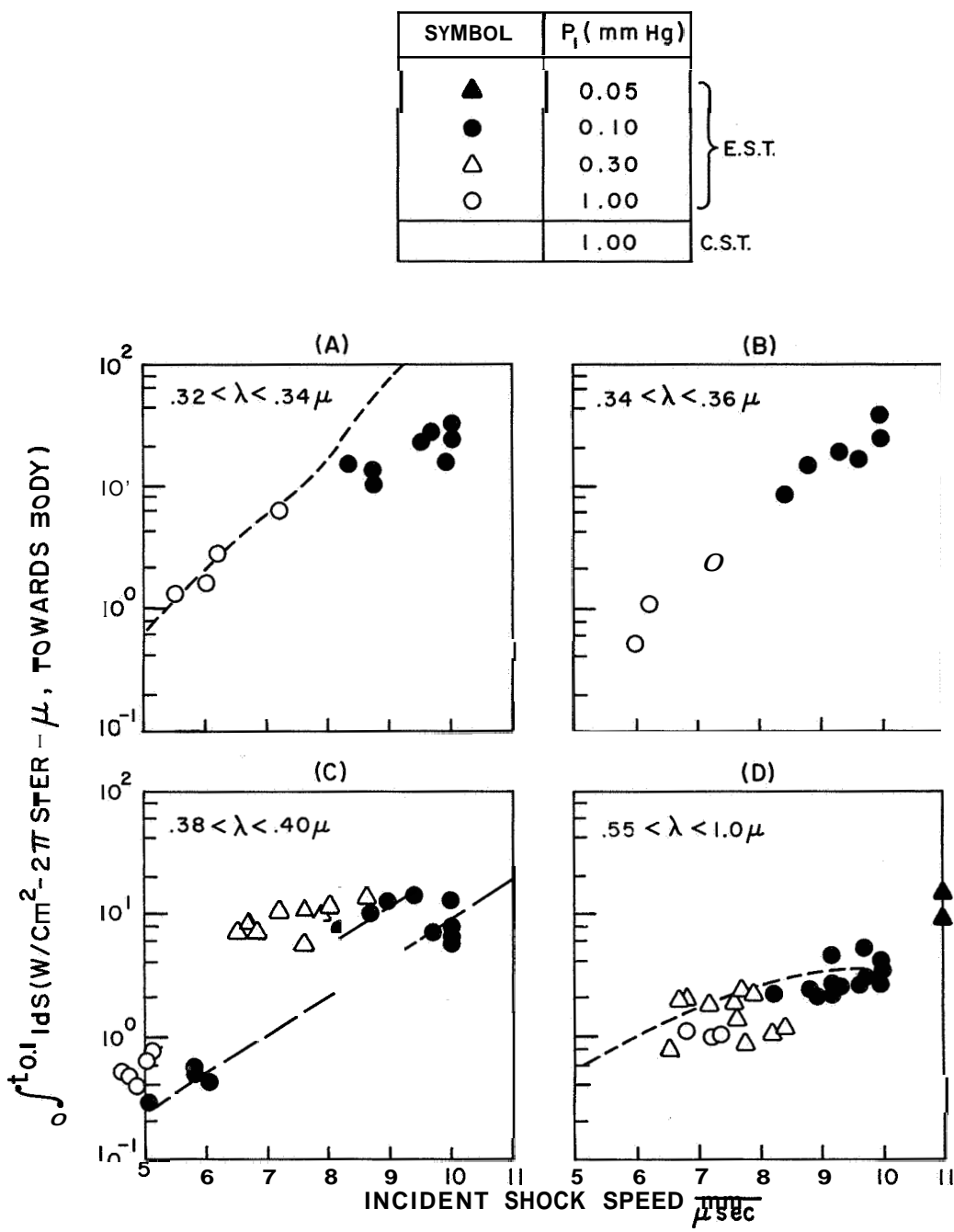


Fig. 13 Non-Equilibrium radiation measurements of normal air shocks at various initial pressures and shock velocities. Sets of measurements were made in the indicated wavelength intervals.

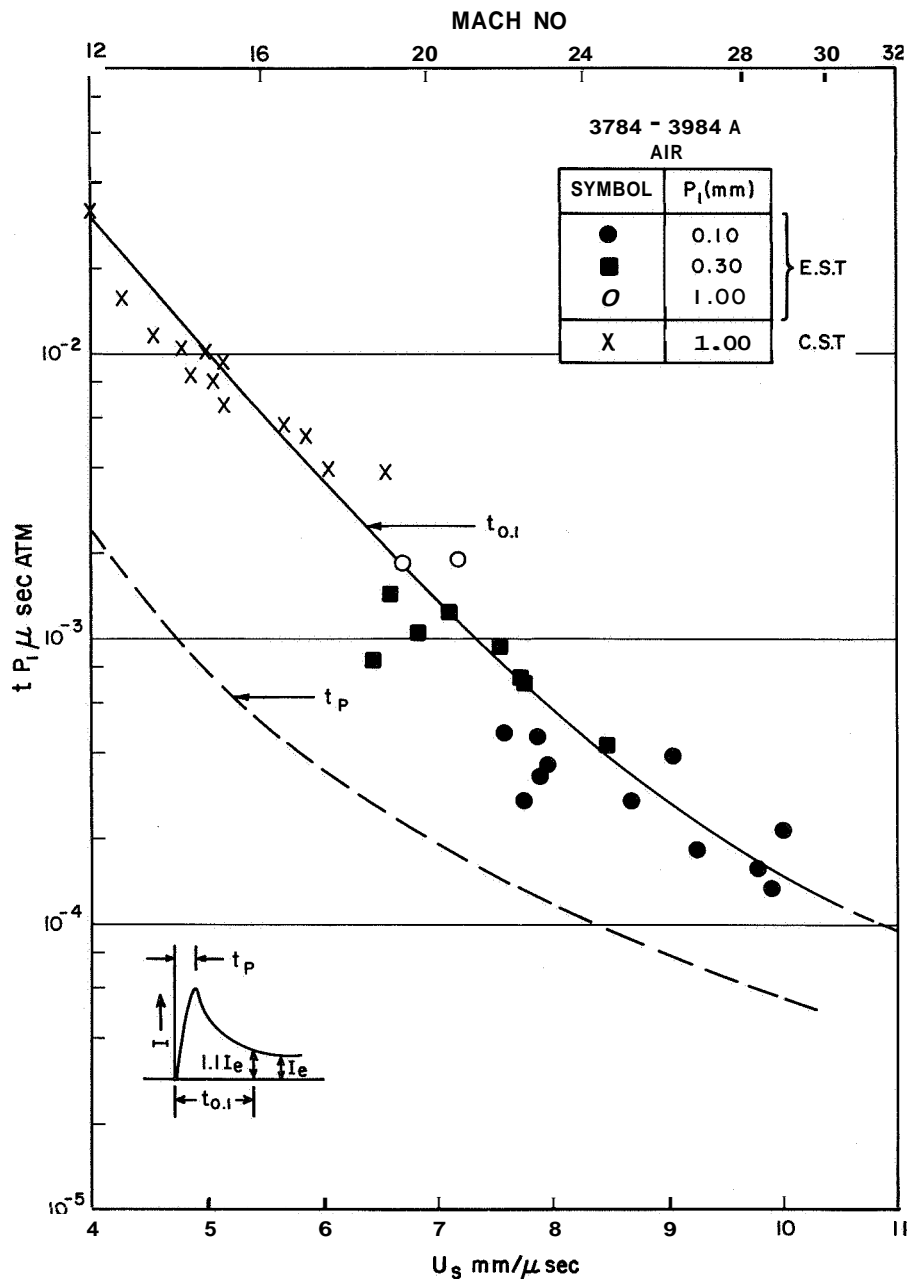


Fig. 14 Observed time duration of luminous front in air, plotted versus shock speed. The time, $t_{0.1}$, in the laboratory coordinate system, is taken to a point at which the radiation intensity has decayed to a level 10% above equilibrium. Initial pressure is used as a scaling factor to correlate data obtained at different values of P_1 . The solid line is an empirical curve drawn through the data. The dashed line corresponds to the observed time to peak radiation, t_p , presented in Fig. 15.

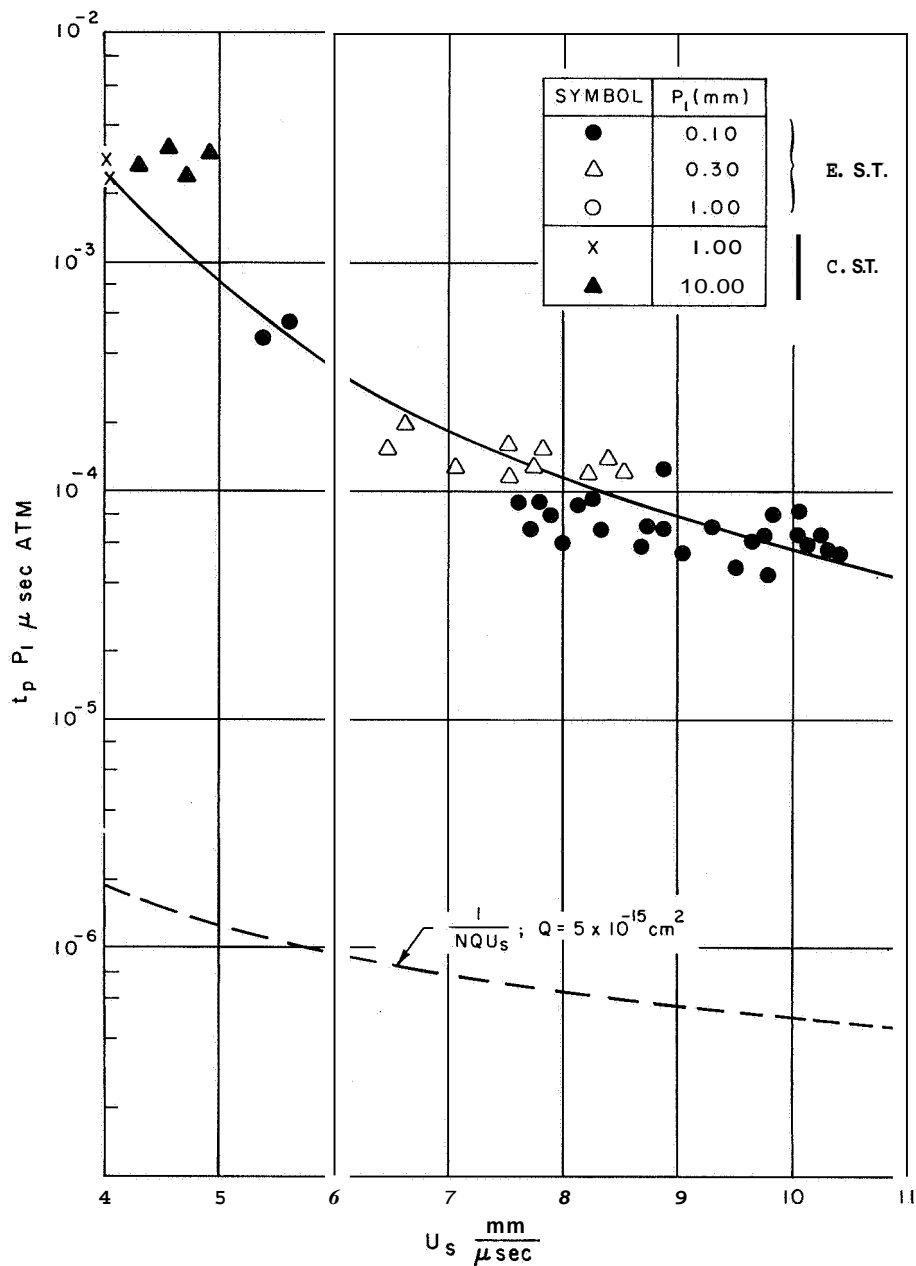
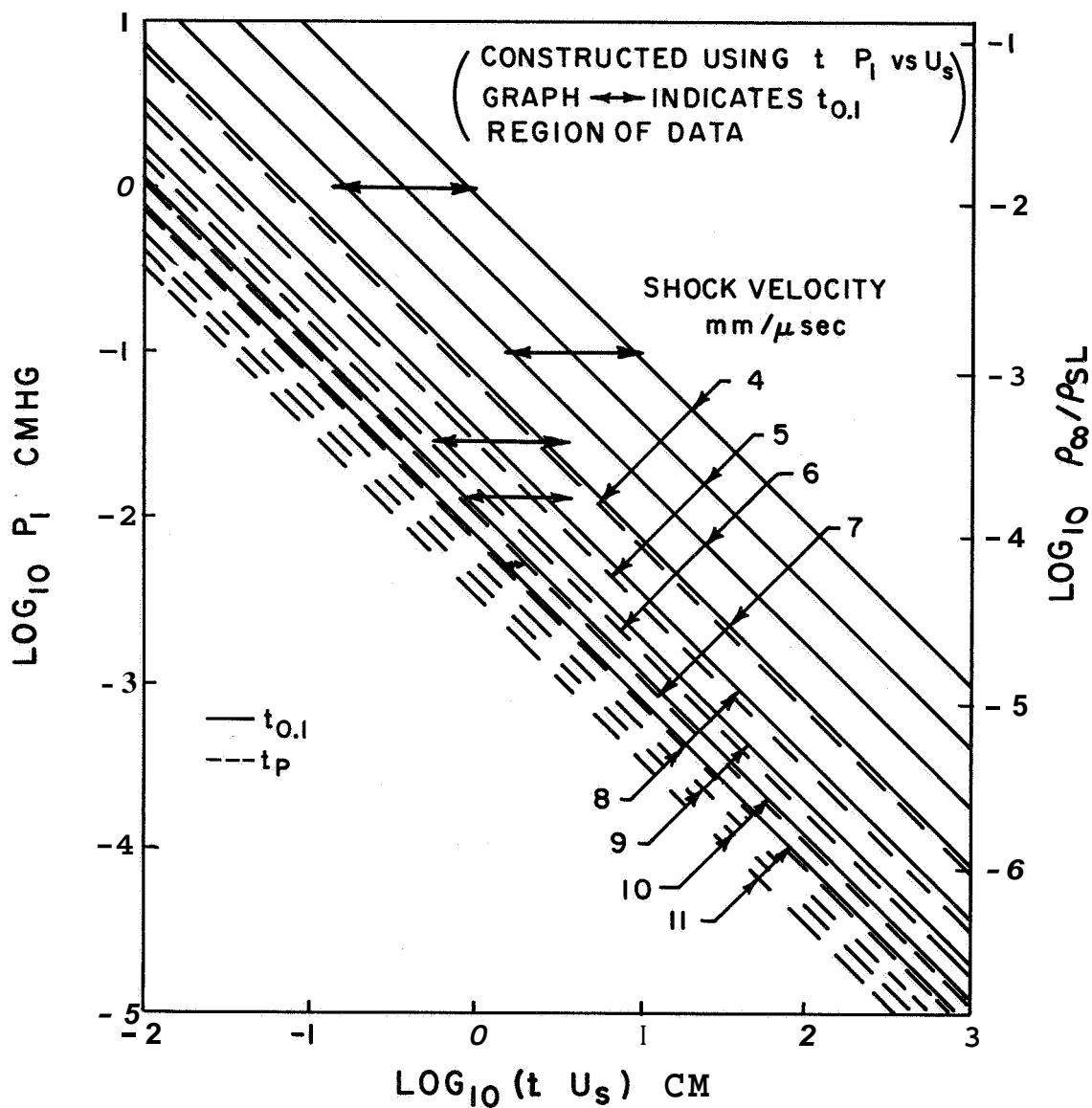


Fig. 15 Observed time to peak radiation of the luminous front radiation in air plotted versus shock speed. Initial pressure is used as a scaling factor to correlate data at different values of P_1 . The dashed line corresponds to a minimum time to peak radiation and is based upon a gas kinetic cross section of $5 \times 10^{-15} \text{ cm}^2$ and the incident shock velocity.



NON-EQUILIBRIUM AND TIME TO PEAK DISTANCE

Fig. 16 Initial pressure, P_1 , is plotted against luminous front thickness $U_s t_{0.1}$, and peak radiation distance $U_s t_p$. The lines have been constructed by means of the empirical data presented in Figs. 14 and 15. Arrows indicate the regions covered by the experiment.

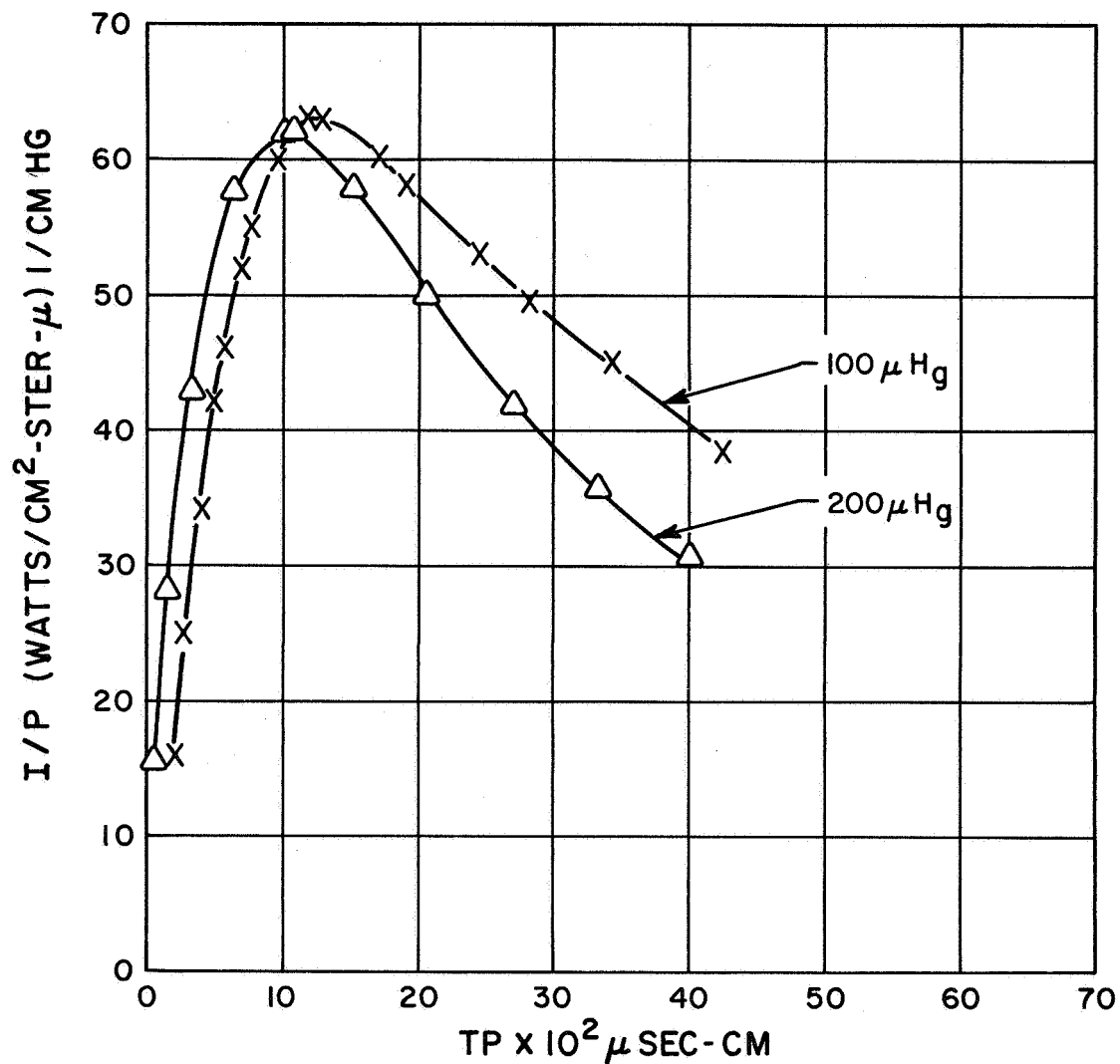


Fig. 17 Radiation intensity profiles of N_2^+ first negative system showing binary scaling. In plotting these profiles the intensity, I , for a 30 cm path length has been divided by the initial pressure, P , in cm Hg; and the time, T , has been multiplied by P . The shock velocities for the two runs were $5.22 \pm .01$ mm/ μ sec.

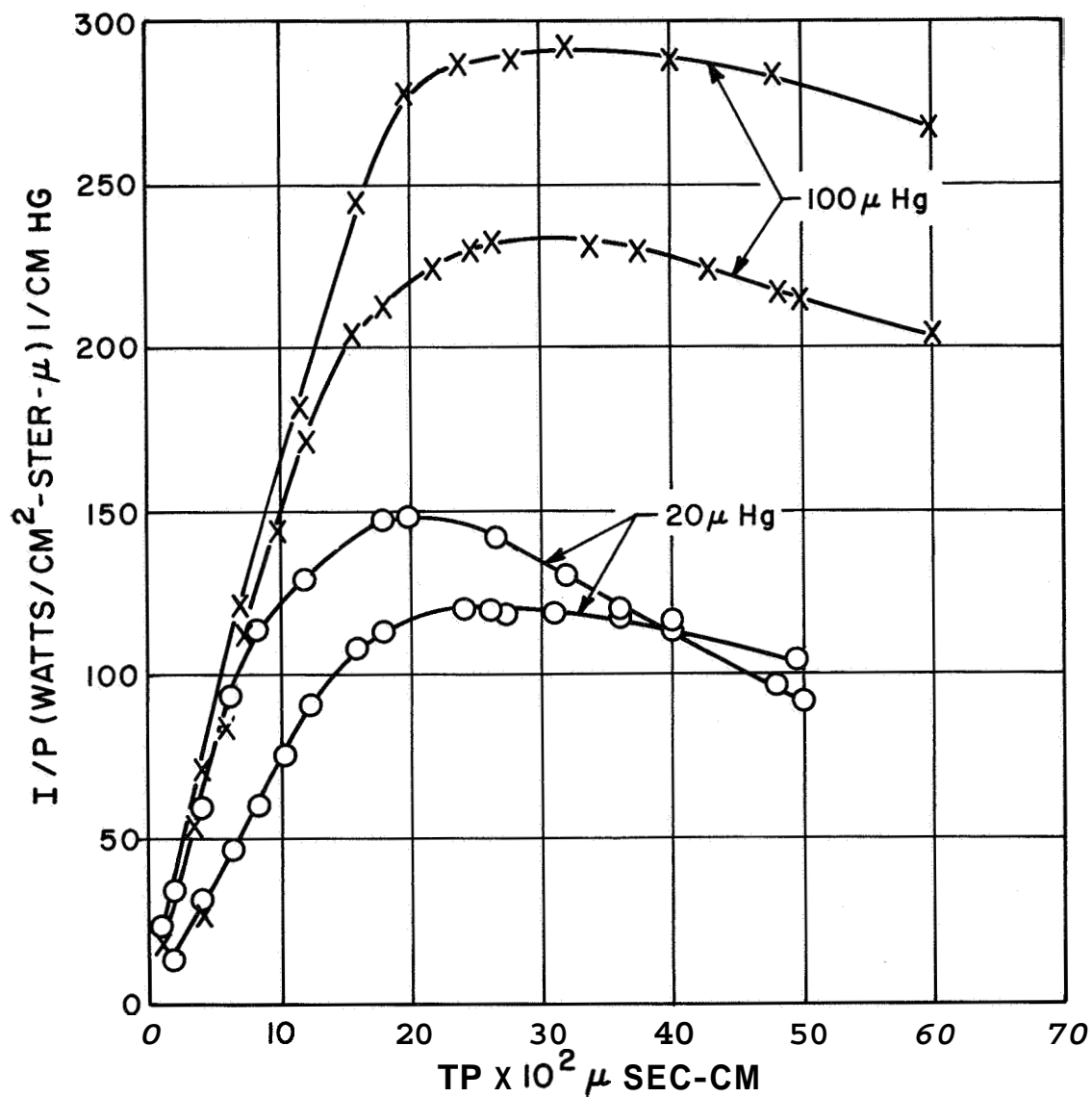


Fig. 18 N_2^+ first negative profiles for 100 μ and 20 μ Hg initial pressure showing a breakdown in binary scaling. These profiles have been plotted as in Fig. 17. The shock velocities for these runs were $5.77 \pm .02 \text{ mm}/\mu\text{sec}$.

CONFIDENTIAL

THIS PAGE IS BLANK

CONFIDENTIAL

IV. PHOTOELECTRIC GAUGE MEASUREMENT (.075 μ to .14 μ WAVELENGTH REGION)

Measurements have been made of the non-equilibrium radiation intensity from a 10mm/ μ sec normal shock in air at a pressure of 0.1mm of Hg in the wavelength region of from .075 to .14 μ using a tungsten photoelectric gauge.

Preliminary tests were made to see where in the shock-heated air, the ultraviolet radiation originated. A tungsten photoelectric gauge was placed at the axis of the shock tube facing the driver as shown schematically in Fig. 19. A 1 1/2-inch steel disk was supported coaxially at a distance of 7/8 inch in front of the gauge. The oscilloscope which displayed the gauge response was triggered when the shock reached a photomultiplier which was placed upstream of the disk. The oscillogram obtained from a 10 mm/ μ s shock in air at a pressure of 0.1 mm of Hg is also shown in Fig. 19. The time at which the shock struck the disk is clearly indicated by the time the trace goes off scale. This sudden rise is due to radiation from the shock reflected from the disk. The oscillogram shows that the ultraviolet radiation began to appear about 8.6 μ sec before the shock struck the disk. This time corresponds to the point where the shock begins to enter the field of view of the gauge. The subsequent curvature of the trace is due to the geometry. The above test clearly indicates that the source of the measured ultraviolet radiation is the shock heated air, not the driver gas. Since the temperature in the non-equilibrium region is many times that in the equilibrium region, it is assumed that the radiation comes from the non-equilibrium region. This point must be clarified in future tests with greater spatial resolution.

The construction details of the photoelectric gauge and its operating principle were described in Ref. 5. Briefly, it consists of a 3/8-inch diameter tungsten disk supported coaxially in a shock tube and masked by its cylindrical case to include a field of view of about 53°. The six-inch diameter arc-driven shock tube was used for this measurement. The gauge was held at a negative potential of about 30 volts and the photoelectric current was measured across a 2,200 ohm load resistor as the shock approached. The 53° field of view should provide a period of 14 μ sec when the gauge irradiation is constant provided there is no appreciable absorption in the test gas between the gauge and the shock. Typical oscillograms are shown in Figs. 19 and 20. The fact that the plateau was absent from the oscillograms indicates that absorption was strong at distances as small as 3/8 inch.

The differential response of the gauge is given by the equation:

$$\frac{dI}{d\lambda}(\lambda) = \frac{\epsilon(\lambda) J(\lambda) d\lambda \lambda^5 A T_s}{hc (6.7 \times 10^{18})}$$

~~CONFIDENTIAL~~

where $I(\lambda)$ = photoelectric current in amperes

$\epsilon(\lambda)$ = photoelectric efficiency of tungsten in electrons per photon

$J(\lambda)$ = radiation intensity normal to the shock in watts/cm²-ster- μ

λ = wavelength in centimeters

A = effective area of tungsten target

T_S = transmission of shield screen

Ω = average solid angle seen by tungsten target

h = Plank's constant = 6.6×10^{-34} watt-sec² per photon

c = velocity of light = 3×10^{10} cm per sec

6.7×10^{18} = number of electrons per coulomb

If the radiating species in the region over which tungsten is sensitive is assumed to be the nitrogen Worley bands ($b^1 1\Sigma_u^+ \rightarrow X^1\Sigma$)²⁸ then the spectral intensity should be proportional to $1/\lambda^5$ between 0.8 to 1.3 microns. Making this assumption and using the response of the gauge at the instant when the shock hits, a spectral intensity was computed and is shown in Fig. 20. The integrated value of the spectral intensity curve was found to give a total radiation intensity in this region of 0.1 watts/cm²-ster. This value corresponds to a value of 9.4 w/cm² - micron radiating towards the body plotted. This value is shown along with the monochromator data in Fig. 10.

~~CONFIDENTIAL~~

CONFIDENTIAL

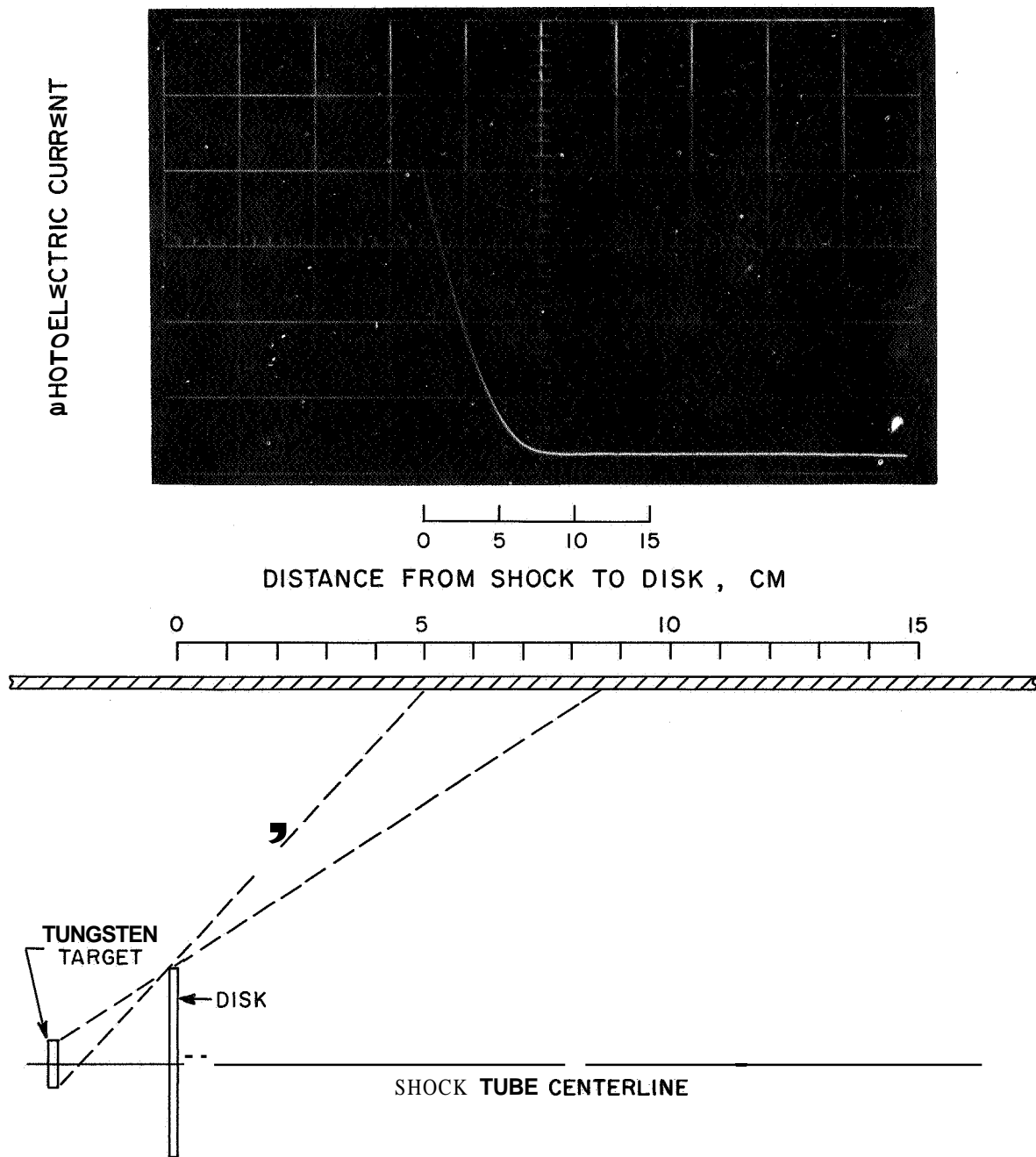


Fig. 19 Schematic diagram showing the geometry used to determine from which portion of the shock-heated gas the ultraviolet radiation emanated; and an oscillogram showing the signal from the tungsten photoelectric gage for a 10mm/ μ sec shock in air at a pressure of 0.1 mm of Hg.

CONFIDENTIAL

~~CONFIDENTIAL~~

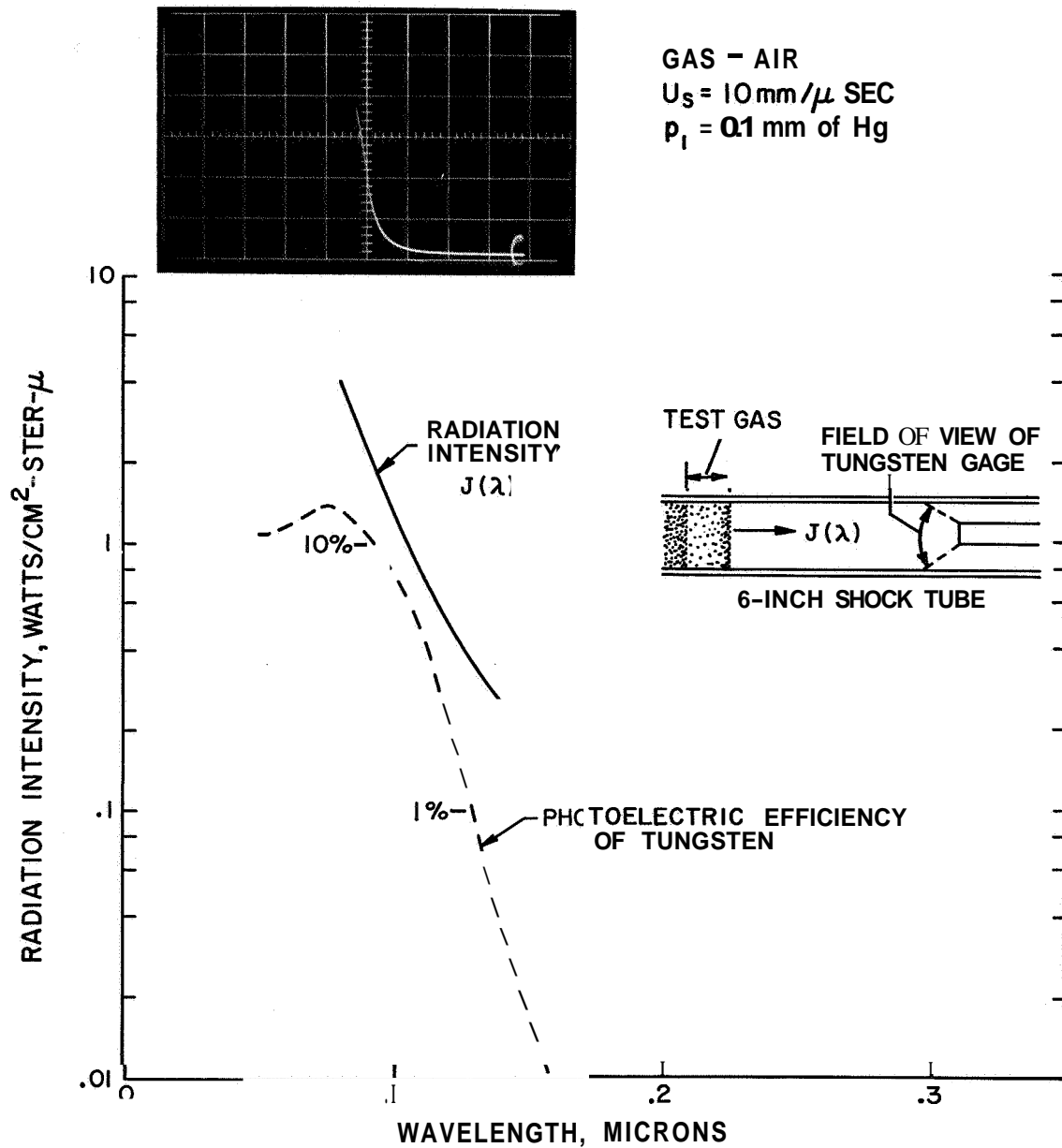


Fig. 20 Spectral intensity of the ultraviolet radiation from a $10 \text{ mm}/\mu \text{ sec}$ shock in air at a pressure of 0.1 mm of Hg. assuming a λ^{-5} distribution from .08 to 0.13μ ; spectral photoelectric efficiency of tungsten; and oscillogram showing the gage response as the shock approached.

~~CONFIDENTIAL~~

V. TOTAL RADIATION MEASUREMENTS

An absolute measurement of the total integrated radiation intensity from both the equilibrium and the non-equilibrium regions of the shock front would be invaluable. It would provide in a single measurement the total radiation intensity which otherwise has to be obtained by the summation of the results of many different measurements made over the whole spectral range from the far ultraviolet through the far infrared. Such a measurement could give an immediate upper bound on the severity of the radiative heating problem, both for the non-equilibrium and the equilibrium contributions, could determine the radiative energy loss from a shock front, and could serve as a check on the monochromator measurements to insure that no spectral regions with significant radiation have been missed.

An infrared heat transfer gauge capable of measuring the total radiation intensity over a wavelength region from about 12 angstroms to over 10 microns has been developed by Camac and Feinberg.²⁹ The gauge consists of a carbon layer, $\approx 0.5\mu$ thick, deposited by pyrolysis on a thin synthetic sapphire window. An infrared detector is focused by a Cassagranian optical system on the carbon surface through the sapphire window. The output of the detector thus measures the emission from, and consequently, (if calibrated properly), the temperature of the carbon layer. From the carbon temperature the incident heat transfer can be inferred. The broad spectral response of carbon to the radiation from the hot gas is taken advantage of to produce the heating of the carbon surface. The thermal properties and the transmission of the sapphire in the infrared are utilized to control the temperature rise and to allow viewing of the carbon by the infrared detector. Detailed descriptions of the gauge design, calibration and selected uses were published in Ref. 29.

An important advantage of this infrared heat transfer gauge is that the detector is physically decoupled from the hot gas by the opaque gauge. Thus, the high temperature phenomena of ionization, photoelectric effects, capacitive effects and electron diffusion are completely isolated from the detector output. The detector measures only the temperature of the carbon and nothing else.

The greatest difficulty encountered has been the limited sensitivity of the system. Heat fluxes of the order of 0.1 - 1.0 kw/cm² are necessary to produce a detectable signal when the gauge is used to measure short heating pulses of the order of 10⁻⁶sec. Several techniques are presently under consideration to overcome this problem. The obvious solution, a more sensitive infrared detector, is available. Recent attempts to produce a free layer of graphite to increase the thermal response to a given heat pulse have also proven quite successful. Between these two techniques significant improvements of the sensitivity are hoped for.

The difficulty of separating the heating due to non-equilibrium radiation from the contributions due to equilibrium air and the driver gas is discussed in Appendix A. The flush gauge geometry used derives only 35% of its signal from the non-equilibrium region. The ability to discriminate between the various contributions to the heating can be changed by using recessed geometries to a point where the non-equilibrium shock front amounts to as much as 90% of the total signal, but only at the expense of an order of magnitude in the signal strength. With the presently used gauge geometries, data reduction is rather tedious due to the complex view factors which must be considered. Great simplifications would be possible by increased sensitivities.

The fabrication of the infrared gauges, particularly the production of the carbon coating on the sapphire, is still somewhat of an art. Thus extreme care must be exercised throughout these experiments to eliminate spurious effects due to poor thermal contact of the carbon and sapphire, dirt, and pin holes in the carbon surface. Fortunately each of these effects produces characteristic and recognizable signals which allow one to make a certain amount of selection among the data.

A number of exploratory experiments were performed to determine if an upper limit to the non-equilibrium radiation could be established with the sensitivity available. Two types of gauges were used. The first were double coated, i.e., a layer of graphite and a layer of aluminum to reflect much of the radiative heating. The response of these gauges was classical, showing the instant rise and characteristic flat temperature response of the laminar heat transfer on the wall of a shock tube as has previously been measured at much smaller shock velocities by Hartunian³⁰ and others.³¹ Extensions of the boundary layer calculations of Mirels³² and Rott³³ by Kemp³⁴ were used to determine an absolute value of the gauge response from these measurements. The heat transfer rate time history, $q(t)$ in this experiment was of the form

$$q(t) = \frac{Q}{\sqrt{t}}$$

where Q is a constant and t is time. The thermal response, $T(t)$, of the gauge to this heating pulse at times large compared to the transit time for the characteristic thermal thickness is

$$T(t) = \frac{Q \sqrt{\pi}}{\sqrt{k\rho C}}$$

In the above, k is the diffusivity, p the density and C the heat capacity at the surface whose properties control the temperature rise, in this case the sapphire window. Of course, for convective heating there is no view factor problem.

The output of the infrared detector is directly related to temperature and is reasonably linear over a limited range.²⁹ Thus, the output $E(t)$, can be written as

$$E(t) = KT(t) = K \frac{Q\sqrt{\pi}}{\sqrt{k\rho C}}$$

$$= K' Q$$

The side wall heat transfer experiments performed measured the value of K' at a shock velocity of 10 mm/ μ sec at an initial pressure of 0.1 mm of Hg. The following values were obtained

K'	$= .525$	$\frac{\text{mv}}{\text{watt}}$	$\frac{1}{\text{cm}^2 \text{ sec}^{1/2}}$	carbon only
	$= .239$	"	"	carbon plus aluminum
	$= .399$	"	"	carbon only

Two other experiments were performed to evaluate this constant. One was a heat transfer measurement on the end wall of a shock tube behind a reflected shock at velocities between 15 and 20,000 ft/sec as used for dynamic calibration by Camac and Feinberg.²⁹ The values of K' achieved from this calibration were

K'	$= .236$	$\frac{\text{mv}}{\text{watt}}$	$\frac{1}{\text{cm}^2 \text{ sec}^{1/2}}$	carbon
	$= .330$	"	"	carbon plus aluminum

The final calibration was by the black body or static method of Ref. 29. In this calibration, the output of the IR cell to a black body source at the window location is measured to give

$$\frac{AE}{AT} \text{ in } \frac{Mv}{^\circ\text{C}} .$$

This response must be corrected for the emissivity of the carbon layer of the gauge in the infrared, C_1 and the absorption of the sapphire, C_2 .

The value measured in this calibration after corrections was

$$\frac{E(t)}{T(t)} = \frac{\Delta E}{\Delta T} C_1 C_2 = .182 \frac{Mv}{^{\circ}C}$$

This value can be converted to K' from the previous equations to give

$$K' = .122 \frac{\frac{mv}{watts}}{cm^2} \frac{1}{sec^{1/2}}$$

The agreement between the three values of K' was felt to be good and verifies the calibration procedures used for this gauge.²⁹

The experiments without the aluminum layer which are sensitive to both aerodynamic and radiative heating were not able to detect a signal which could be attributable to non-equilibrium radiation. This statement is based on the fact that the signal did not rise noticeably prior to the arrival of the shock front at the gauge. A typical oscillogram is presented in Fig. 21. At the point where the shock arrives at the gauge a small rise is visible followed by a steady rise. This signal is attributed to convective heating. The arrival of the shock and the non-equilibrium radiation profile are seen from the monitor trace below the IR detector output.

Thus, the problem of estimating an upper bound to non-equilibrium radiation becomes one of determining how large the radiation under the monitor spike could have been without creating a detectable signal prior to the arrival of the shock. For this estimate the view factor of the gauge must be carefully accounted for. This procedure has been described in Ref. 29. The view factor for the shock tube and gauge geometry used in these experiments are derived in Appendix A. An upper limit of the non-equilibrium shock front can be calculated by the safe assumption that all the radiation comes from a thin slab of heated air moving with the shock velocity. The width of this region is taken to be the width of the non-equilibrium profile on the monitor in Fig. 21, i. e. , 2 cm.

It was shown²⁹ that the surface temperature of the carbon on sapphire at the time of arrival of the shock $T(t_s)$ could be approximated by

$$T(t_s) = 0.9 \sqrt{t_s} q(t_s)$$

for any heat input of the form $q(t) = Qt^n$. The value of the constant 0.9 was correct to a factor of two for all the heat pulse shapes considered.²⁹ In the above, t_s is the arrival time of the shock at the gauge measured after the onset of the first significant heating, and $q(t_s)$ is the heat transfer rate actually seen by the gauge at the time, t_s .

Inspection of Fig. 21 shows that the signal has not risen at the arrival of the shock, t_s . We therefore assume the noise level, i.e. 0.15 mv, as the magnitude of the signal which represents the smallest heat transfer rate detectable by this gauge. Inspection of the variation of view factor for the experimental geometry, Fig. 22 shows that at a distance of 10 cm, i.e., $t = 10\mu$ sec at 10 mm/ μ sec shock velocity, the view factor has dropped by an order of magnitude. This should be sufficient to make the gauge temperature rise approximately zero. Thus, we take t_s equal to 10μ sec and get for the maximum heat transfer rate seen by the gauge.

$$\dot{q}(t_s) = \frac{\frac{.15 \times \text{mv}}{.1 \times 82 \text{ mv/oC}}}{(0.9)(\sqrt{10 \times 10^{-6}})} = 2.91 \times 10^2 \frac{\text{watts}}{\text{cm}^2}$$

The heat transfer to the gauge $\dot{q}(t)$ can also be written in terms of the radiation viewed as

$$\dot{q}(t) = \frac{q^*(A)}{2} \times a \frac{I}{\text{cm}^2}$$

where a is the tube radius and $q^*(A)$ is the view factor parameter (which was calculated for a two unit radiation intensity and consequently is divided by 2 to make the units of I be watts/cm³ - ster). A value of $q^*(A)$ of 1.4 is chosen appropriately for the front or Region 1 of the "short slug" in Fig. 22. The "short slug" fits the profile of the observed radiation profile. Solving for the intensity, I , we get

$$I = \frac{291 \times 2}{1.4 \times 7.62} = 54.5 \frac{\text{watts}}{\text{cm}^3 \text{ ster}}$$

The non-equilibrium radiation in terms of watts/cm² for 2π steradians for a 2 cm thick front, would thus be

$$I = 684 \text{ watt/cm}^2 - 2\pi \text{ ster}$$

This value can not be considered as an absolute upper limit because of the several approximations made. The potential of this technique and the importance of improving the sensitivity of this instrument are clear from the above result.

Progress in this direction has been encouraging. The technique of producing and handling a free carbon layer has been developed. This free layer is not in good thermal contact with the window and consequently the temperature response of such a gauge is not determined by the backing material but by the heat capacity of the carbon itself. By not requiring

~~CONFIDENTIAL~~

thermal contact we can now resort to window materials other than sapphire which transmit at longer wavelengths. Such windows allow us to use a more sensitive liquid helium cooled infrared detector. Such a detector has been used to detect a 0.1 degree C temperature rise of the carbon. Such sensitivity should allow us to measure non-equilibrium shock front radiation as low as 525 watts/cm² - 2 π ster, and equilibrium radiation as low as 54 watts/cm² - 2 π ster (see Appendix A).

~~CONFIDENTIAL~~

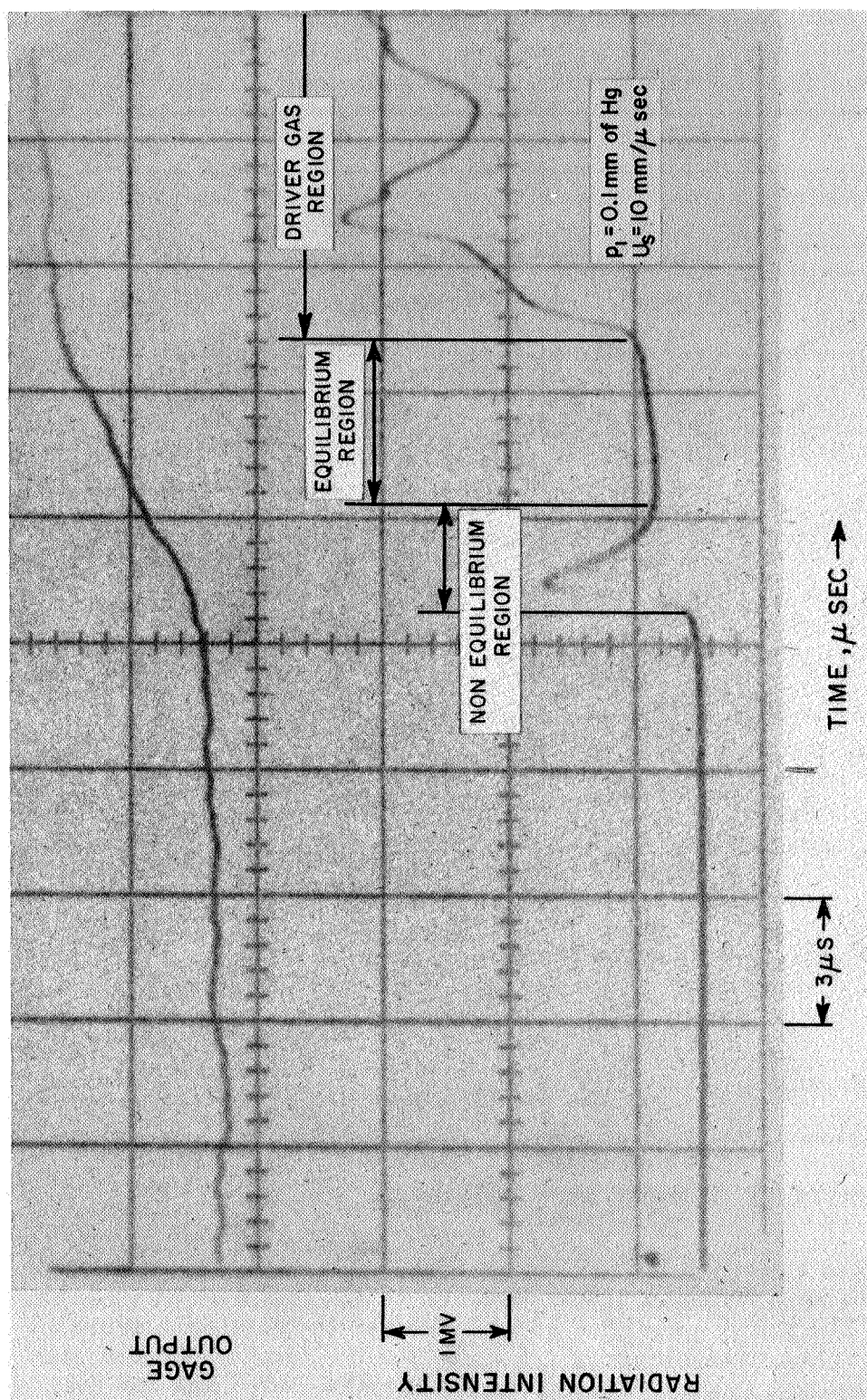


Fig. 21 Dual beam oscillogram showing the response of the infrared heat transfer gage and the response of a photomultiplier viewing the shock at the same station.

CONFIDENTIAL

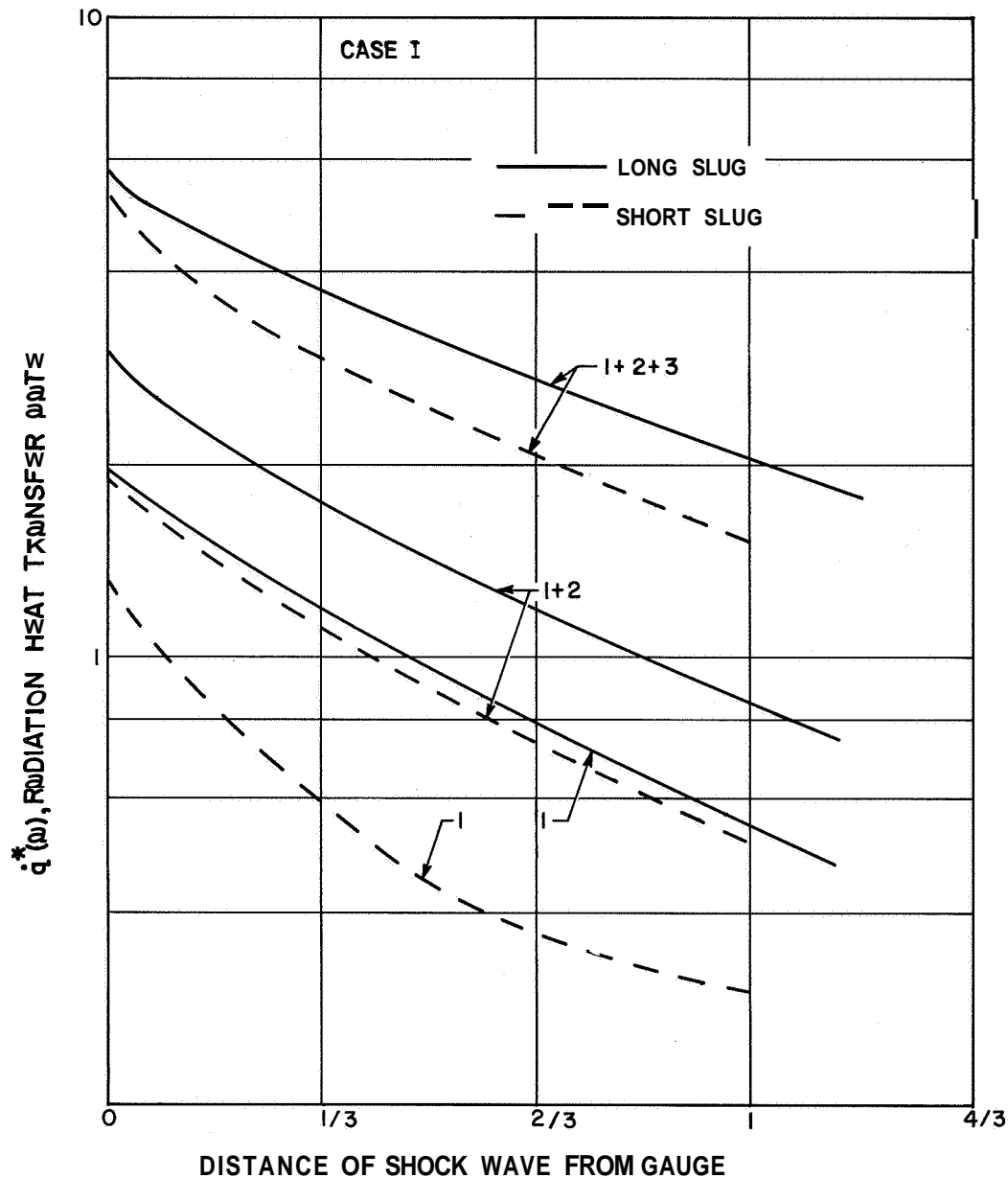


Fig. 22 Theoretical radiation heat transfer rate $\dot{q}^*(A)$ from normal shock heated gas as a function of the distance of the shock wave from the gauge. The curves designated by 1 are for the luminous front region; curves designated by 1 + 2 are for the luminous front plus the equilibrium region; and curves designated 1-2-3 are for the other two regions plus driver gas. For the Case I presented in this figure and a discussion of long and short slugs one is referred to reference.

CONFIDENTIAL

VI. PHOTOGRAPHIC TECHNIQUES

Several photographic techniques are available for the study of transient phenomena in shock heated gases. Figure 1 showed a drum camera spectrogram taken by the racetrack technique. However, this technique is severely limited in intensity and no spectra have been obtained by this technique at initial pressures of 0. 1 mm Hg or less.

A Space Technology Laboratories' image converter has a light amplification ability of 50 to 1 and has the required speed and sensitivity for obtaining time resolved shock front spectra. Figure 23 shows a series of exposures looking through a 6-inch port in the side of the test section of the electric shock tube. The exposures are separated in time by 5 microseconds. The luminous front and approximately 10 cm of test gas can be clearly identified. The shock conditions are $p_1 = 0. 1$ mm Hg, $U_s = 10$ mm/ μ s.

Figure 24 shows a spectrum taken by the image converter operating in the race track mode. The approximate wavelength region of sensitivity was $.35 - .54\mu$. The N_2^+ (1-) radiation can be identified in the luminous front and equilibrium region. This spectrum has poor spatial and wavelength resolution. Improvements in this technique to produce detailed spectra of all sources of radiation are of utmost importance.

~~CONFIDENTIAL~~

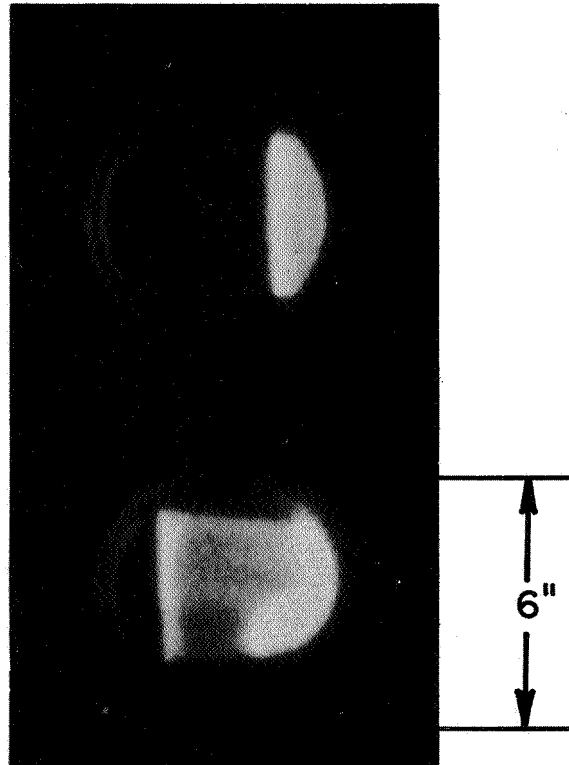


Fig. 23 Photographs taken with an S. T. L. image converter of a normal air shock in a 6" electrically driven shock tube. The time difference between the two exposures was 5 microseconds. The exposure time was 50 milimicroseconds.

~~CONFIDENTIAL~~

~~CONFIDENTIAL~~

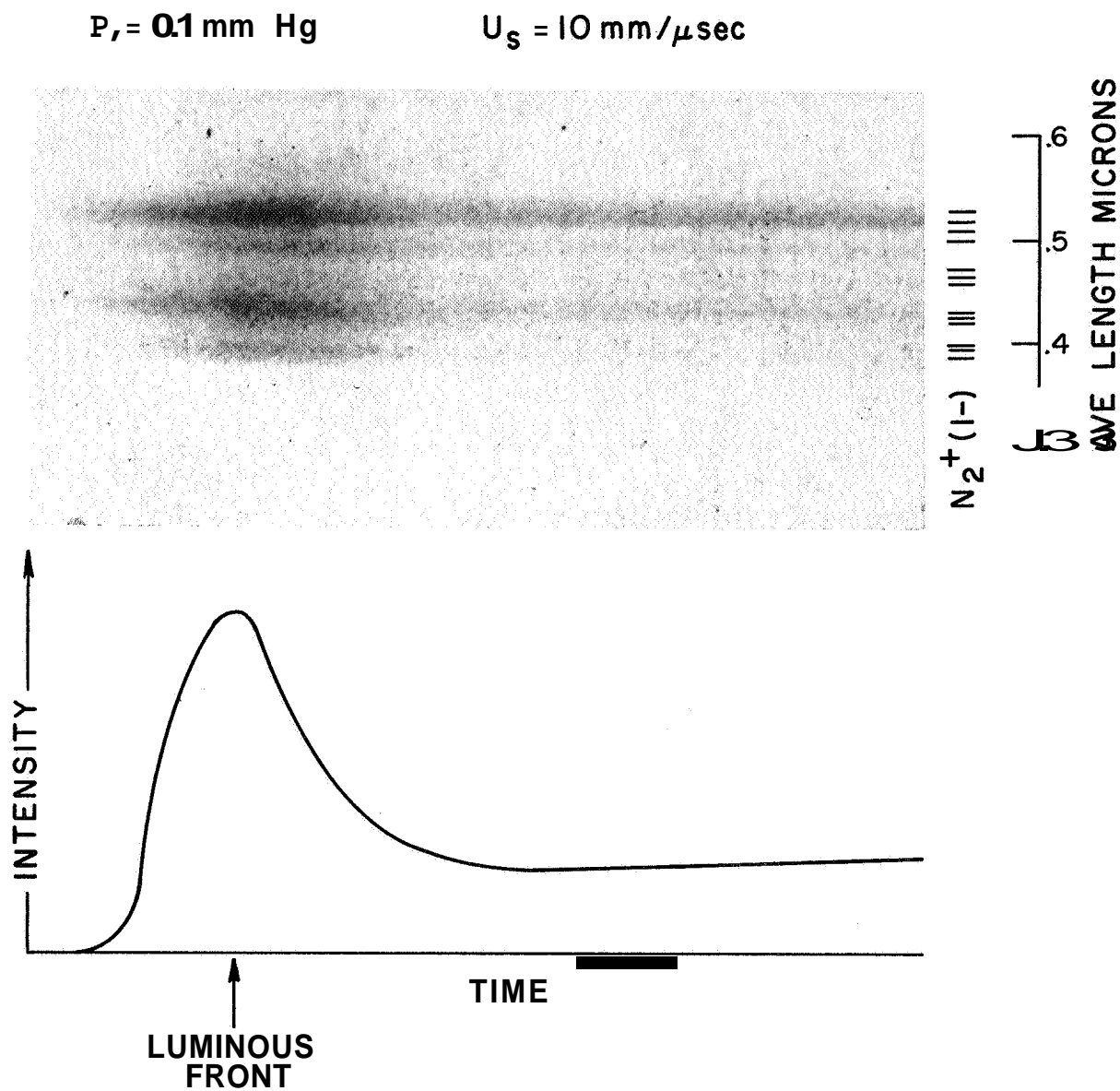


Fig. 24 Race track spectra taken with S. T. L. image converter of a normal air shock. $U_s = 10 \text{ mm}/\mu\text{sec}$, $P_1 = 0.1 \text{ mm Hg}$. The spatial and wavelength resolution is poor, however the $N_2^+(1-)$ radiation is identified.

~~CONFIDENTIAL~~

~~CONFIDENTIAL~~

THIS PAGE IS BLANK

~~CONFIDENTIAL~~

VII. PRESENT STATE OF KNOWLEDGE

A. Summary of Existing Data

A summary of existing data on non-equilibrium radiation is displayed in Fig. 25. The single AERL point, represented by the solid triangle, is the area included under the dashed line in Fig. 10 which represent the most thorough spectral survey made to date. This value should be considered as a reasonable upper limit for the non-equilibrium radiation at 33,000 ft/sec. The point representing the carbon gauge measurement should be considered a solid upper limit of non-equilibrium radiation with the reservations previously outlined. The non-equilibrium radiation data reported in Ref. 5 is plotted at its proper velocity at 25,000 ft/sec. The velocity dependence shown was obtained empirically from Fig. 13. Results obtained from observing the radiation given off by hypervelocity projectiles fired in ballistic ranges at NASA Ames Research Center are also plotted.³⁵ It was possible to predict "severe truncation" of some of this data from our measurements of the distance to peak radiation, i. e. , Figs. 14, 15 and 16. It was assumed that the distance to the radiation peak had to be several times the stand-off distance before "severe truncation" set in to qualitatively account for the pressure of the body.

The over-all agreement between the present data and the Ames results is excellent. A few measurements made at Ames at velocities above 33,000 ft/sec indicate that the velocity dependence of the radiation does not become significantly different above 33,000 ft/sec. Some shock tube measurements have been made at shock velocities as high as escape velocity, as shown in Fig. 13. The ballistic range data is severely limited in wavelength coverage and recourse is made to shock tube data to account for regions of the spectrum not seen by the detectors. However, as seen in Fig. 10, even shock tube data has limited wavelength coverage in the ultraviolet, and the infrared beyond 1.0 micron. A need exists for developing instruments to gain coverage of the wavelength regions which are not so easily attainable to check the small possibility of the existence of an unknown source of significant radiative heating.

B. Present State of Theoretical Knowledge

The first step toward understanding non-equilibrium radiation for a normal shock front is a knowledge of the chemical kinetics of high temperature air. Any attempt to predict radiation must rely on calculations of the temperature, density and particle concentration histories behind the shock front as well as a knowledge of the excitation mechanism for the radiating species. Calculations can be made by integration of the chemical rate equations with a given set of rate constants. The relevant chemical rate constants are reasonably well known³⁶ for temperatures

~~CONFIDENTIAL~~

up to 8,000°K. However, to make calculations for shock speeds of 40,000 ft/sec, it is necessary to extrapolate the assumed temperature dependence for these rate constants to temperatures of 75,000°K in some cases.

Determination of some of the pertinent rates were made by examining the rate of decay of the radiative relaxation profiles very near the equilibrium region.⁹ The rates were chosen to fit the radiation profiles in the region near equilibrium, where the molecular vibration and electronic degrees of freedom have relaxed over a wide range of conditions. Hammerling et al¹⁴ have discussed a tentative coupling of vibrational relaxation with the dissociation process, which states that dissociation can take place equally well from any vibrational level in the ground state molecule. The over-all effect of this coupling is to slow down the dissociation rates in the gas until vibration has relaxed to the local translational temperature, at which time the dissociation rates can proceed at their full values. When the chemical rates are extrapolated in the usual manner and the coupling scheme of Ref. 14 is used, good agreement is obtained between experiment and theory in the radiative relaxation region near equilibrium.⁹ This process has been carried out in air and it has been demonstrated that the calculations of translational temperature, density and particle concentrations behind a normal shock are reasonable. Despite the extreme extrapolation necessary, chemistry does not appear to be the main problem in our effort to synthesize the radiative mechanisms of the shock front.

Understanding the luminous front radiation hinges upon a knowledge of how energy initially invested in heavy molecules is transferred to molecular electrons. This question is our main problem. A tentative hypothesis has been made that electronic degrees of freedom are strongly coupled to vibrational energy in the gas.⁹ This hypothesis is in accord with observations in gas discharges where radiation is quenched more effectively by molecules than by atomic collisions.³⁷ It is also in accord with temperature measurements in nitrogen shocks made by F. S. Faizullov et al,³⁸ using sodium line reversal techniques. He observed that the population of excited sodium atoms followed the vibrational temperature of the nitrogen. There are other indications, notably in the work of Gaydon and his co-workers,^{39,40} that such a coupling exists. Work is presently underway at AERL to test this hypothesis in pure nitrogen shocks.

A semi-empirical procedure for making calculations of molecular non-equilibrium radiation is possible. It is based on the fact that the chemistry of the non-equilibrium region is reasonably well known and that measurements of the time to the radiation peak, Fig. 15, are available under the conditions for which calculations are desired.

The program of Ref. 14 can be used to calculate the particle densities of various species and translational temperature history for a given flight condition. If the population of a given molecular excited level is held in equilibrium with its ground state population at the local translational temperature, the local radiation intensity can be calculated from equilibrium data. The excitation region is approximated by assuming a linear rise of

~~CONFIDENTIAL~~

~~CONFIDENTIAL~~

radiation starting from zero at the shock front to intersect the curve derived from the above assumption at the time of peak radiation obtained from the data in Fig. 15. Integrating the area under such a radiation history profile, one gets a value for the integrated non-equilibrium radiation from a given molecular radiating system. Figure 13 (A,D) shows a comparison between integrated non-equilibrium measurements and the appropriate lines (dotted lines in the figure) calculated by this method for the $N_2(2+)$ and $N_2(1+)$ systems respectively. The oscillator strengths used for these calculations were those published in Ref. 10.

The $N_2(2+)$ system is assumed to radiate 1/4 of its energy in the .32-.34 μ region, and the $N_2(1+)$ system 3/5 of its energy in the 0.55 -1.0 μ region.^{8,9} The lack of agreement in Fig. 13 (A,D) is not surprising since, firstly, there are other radiating species which will radiate in these wavelength regions, and secondly, this method of approximating the excitation region of the luminous front is very crude. Nevertheless, an approximate velocity dependence is obtained, and the calculations have been found to be useful for extrapolation of the non-equilibrium molecular radiation to conditions not covered by the present experiments. This calculational procedure is further discussed in the next section where it is used to apply to a flow field calculation.

Another unknown which is important at lunar re-entry velocities is Kramer's radiation.^{4,6,25} This radiation is produced by the deceleration or capture of electrons by ions. The intensity of radiation is a function of the electron temperature as well as the concentration of electrons and ions. Calculations must be made to estimate the effective electron temperatures as well as particle concentration histories in the shocked gas if one is to extrapolate present Kramer's radiation measurements to regions inaccessible to experiment. This form of radiation will not be "collision limited" in the usual sense, since the radiation comes about by the interaction of particles in the gas rather than by spontaneous emission of a photon by an excited molecule. It is possible that a similar effect will be produced, however, if by some process the electron temperature is reduced below the translational temperature of the gas. Additional work is needed to measure Kramer's radiation at equilibrium conditions corresponding to escape velocity flight conditions.

~~CONFIDENTIAL~~

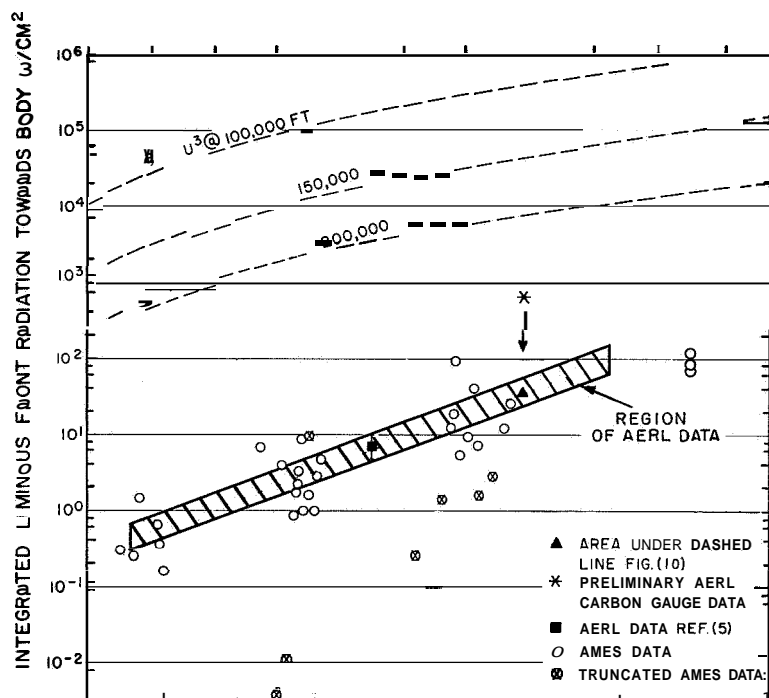


Fig. 25 A summary of existing Avco-Everett Research Laboratory and Ames Research Center non-equilibrium radiation data.

VIII. NON-EQUILIBRIUM AND EQUILIBRIUM RADIATION IN FLIGHT

As long as our understanding of the mechanism whereby the excited radiating states are produced is incomplete, we are not in a position to calculate and predict the non-equilibrium radiation time history for a shock front or its effect on a vehicle surface. Estimates of the non-equilibrium radiation widely differing from reality can result from a lack of knowledge of the excitation mechanism and its rate.⁸ Use of the experimental data in a semi-empirical calculation scheme to approximately reproduce the observations, as discussed in the previous section, must suffice in lieu of a complete theory of the non-equilibrium shock front radiation.

The empirical fit of the measured radiation rise time to the calculated decay of radiation is the basis of our calculation scheme. In following this procedure, one must consider phenomena and loss mechanisms not usually included in flow calculations. During the early portions of the shock front, particularly at high speeds and high altitudes, one must account for the loss of energy by radiation.^{41,42} The reabsorption of radiation, i. e. , departures from the usual transparent gas assumption also can become important.^{12,43} Fortunately, the measured location of the radiation peak is such that in many cases the region immediately behind the shock front, in which radiation losses would amount to a significant depletion of the total kinetic energy of the flow and where reabsorption should be strongest, is eliminated as an emitting region by the slow excitation process.

The variations of the thermodynamic properties and compositions of the flow behind a shock front are calculated by the non-equilibrium chemistry program of Teare.¹⁴ The subsequent decay in radiation time history can be calculated by assuming that the translational temperature is the appropriate temperature governing the population of the excited levels of the radiating molecules. Thus, the simple equations for the contributions of the three dominant nitrogen molecular band systems given below which follow from this assumption and a knowledge of the f numbers⁶ apply.

$$I [N_2(1+)] = 2.5 \times 10^{-13} [N_2] \exp (-90,000/T_e)$$

$$I [N_2(2+)] = 3.4 \times 10^{-11} [N_2] \exp (-129,500/T_e) \quad \text{Watt/cm}^2 \text{ ster}$$

$$I [N_2^+(1-)] = 1.6 \times 10^{-12} [N_2^+] \exp (-36,000/T_e)$$

In the above, $[N_2]$ is the number of ground state nitrogen molecules per unit volume, and $[N_2^+]$ is the corresponding number of ground state molecular ions, both of which are calculated by the chemistry model in the normal shock calculation program.¹⁴ T_e is the electronic temperature which we are assuming to be equal to the translational value at times greater than the time required to reach the radiation peak.

The non-equilibrium radiation is calculated only for the three band systems listed above. At air temperatures above 8000°K , an important source of radiation arises from the acceleration or capture of electrons by atoms or ions. The calculated intensity of this radiation, called Kramer's radiation, does not show a direct exponential temperature dependence as do the molecular bands. Approximate contributions of these sources can be calculated from the following equations:

$$\begin{aligned} I [N^+] &= 2 \times 10^{-32} [N^+] [e^-] \left(\frac{10^4}{T} \right)^{0.5} \\ I [O^+] &= 2 \times 10^{-32} [O^+] [e^-] \left(\frac{10^4}{T} \right)^{0.5} \end{aligned} \quad \frac{\text{watt}}{\text{cm}^3\text{-ster}}$$

where $[N^+]$, $[O^+]$ and $[e^-]$ are the respective concentrations expressed in particles/cm³. If total radiation profiles are desired, the nitrogen molecular band system contributions during the non-equilibrium front must be fair-
ed into the equilibrium values which are dominantly due to the atomic ion reactions. For this reason, the distance to the equilibrium region from this calculation is, in general, shorter than the distances calculated or measured for specific molecular bands.

The results of such calculations performed for a shock velocity of 9.64 mm/ μ sec (31,600 ft/sec) are shown in Fig. 26. The calculation was performed for two values of assumed rise time, 0.19 and 0.61 cm in terms of the distance from the shock front to the radiation peak. Both these times were found to be sufficiently long that the energy loss from the radiation peak was not noticeable. However, if the rise time were much shorter than the 0.19 cm case, the strong radiation indicated by the dotted line would surely decrease the energy of the gas and reduce the subsequent intensities.

As long as there is no significant energy loss, a single such curve can be used to determine the variation of integrated non-equilibrium radiation, i. e., from the shock front back to the point where the intensity is 10 percent above the equilibrium value, with assumed distance to the peak radiation. This result is shown in Fig. 27 for the same shock strength, i. e., 9.64 mm/ μ sec, and an initial pressure of 0.18 mm of Hg, or a density representative of flight at about 200,000 ft altitude. From the measurements of the rise time of the radiant intensity, Fig. 15, properly scaled to account for the binary reaction chemistry, the proper value of total integrated non-equilibrium radiation intensity can be determined in this plot, as indicated in Fig. 27.

The extreme sensitivity of the radiation intensity to the excitation mechanism is clearly shown in this figure. At approximately the measured value of the radiation rise time, the integrated intensity will change by a factor of three if the rise time is made only twice as fast. This sensitivity will increase further with shock velocity since the initial translational temperature in the shock front increases with the square of the shock speed and the time to peak decreases as the shock velocity increases.

The predictions of this calculation scheme were compared to both the absolute value and velocity dependence of the measured nitrogen first and second positive band system radiation in Fig. 13 (A,D). The agreement of the N_2 (1st) band system is quite good in the velocity range investigated. The less satisfactory agreement for the N_2 (2nd) data at velocities above $8 \text{ mm}/\mu \text{ sec}$ is not too surprising in view of the crudeness of the calculation scheme and factors, such as collision limiting and other radiating systems which could be present in the measurements, which have been ignored in the comparison.

An experimental profile of the radiation in the 0.55 to 1.0μ wavelength region is compared to a calculated one in Fig. 28. The time to peak was normalized in the calculation as described above, so the agreement of this time is not too surprising. However, the absolute magnitudes are not normalized. The high equilibrium value of the measurements is due to sources of other than the N_2 band systems which were not included in the calculation scheme; namely, Kramer's radiation and atomic nitrogen lines, as discussed earlier. Neither of these sources overshoot as strongly as the nitrogen molecular bands, and consequently, the overshoot should initially correlate to the calculated value considering the nitrogen bands only, and at later times, approach an equilibrium value which includes the contributions from the other band systems. This general character of the correlation between the radiation measurement and this calculation scheme is clearly observable. A better correlation than this general qualitative description of these details of the shock front processes is probably beyond our present capability.

To complete this empirical calculation scheme, we fair the decay of the molecular nitrogen band system radiation into the level of the total equilibrium radiation, as calculated from Kivel and Bailey.⁶ The accuracy of these tables of equilibrium radiation are not the subject of a lengthy discussion here. Despite the fact that several of the numbers used in these tables need to be modified,^{18,44} this has not been considered to be a serious limitation in the temperature and density region of interest to project Apollo. The critical radiating systems which need to be considered are Kramer's radiation, due to recombination of electrons with nitrogen (also some oxygen) atomic ions, and atomic nitrogen lines. None of the proposed f number corrections effect these systems. The present status of knowledge of these sources was discussed in a previous section. It is known that the values of Kramer's radiation are somewhat high in Ref. 6, however the absolute value which should be used is still in doubt. Atomic line radiation is not included in the estimates of any of the radiation tables. In lieu of having better and more definitive data, the values of Ref. 6 shall continue to be used here.

The proposed normal shock calculation scheme has been used to estimate the three-dimensional effects when the shock is not plane but envelopes a blunt body. It would be highly desirable to treat the blunt body problem simply as a normal shock or as some simple modification, thereof. However, as a streamline very near the stagnation point travels along the body for distances more than ten times the stand-off distance of the shock at the stagnation point, it is dangerous to assume a priori that the normal shock properties can be correlated to the blunt body situation.

Several methods have been developed to introduce finite rate chemistry into flow field calculations. One obvious approach is to introduce the rate equations for the various reactions into the method of characteristics and thus to solve the complete non-equilibrium flow field. The computational difficulties of this method are considerable and, although attempts are being made by several investigators in this direction, this approach **has** not answered the real problem which is the subsonic flow field immediately behind the shock. However, the two limiting cases, equilibrium and frozen characteristic calculations are available. ^{45, 46}

In lieu of a complete non-equilibrium solution, several investigators have combined normal shock wave chemistry calculation programs into a stream tube method for calculating variations of the thermodynamic properties and composition of a flowing gas. In this method, a pressure history is prescribed into which the products of the normal shock calculation are forced to flow. The pressure distribution may be obtained from either equilibrium characteristics, frozen characteristics, blast wave theory, or any other assumption. The locations of the stream tubes can be determined from conservation of mass.

Another approach which has been adapted to the blunt body program is the inverse method of subsonic flow field calculation. ⁴⁷ In this method, a body shape is found by stepwise integration of the conservation laws starting with a known shock geometry. Marrone⁴⁸ has added the rate equations for the reactions important in high temperature air to his procedure, and thus can calculate a non-equilibrium flow field by the inverse method. An apriori knowledge of the shock wave shape which results in a given body geometry is required by this method.

The accuracy and use of these methods for describing the inviscid flow field about a blunt body has been described in the literature. However, application of these techniques to the determination of the radiation history in the stagnation region is hampered by the same difficulties which have been discussed with respect to the normal shock front radiation history calculation, i. e. , the uncertainties about the excitation process. To apply the empirical calculation scheme for the nitrogen band systems to the blunt body, either the stream tube method or the inverse flow field calculation could be utilized. The inverse method has as its main advantage, the ability to account for modifications of the bow shock due to non-equilibrium effects. A change by about a factor of two occurs in the shock detachment distance between equilibrium and completely frozen flow. However, this effect

~~CONFIDENTIAL~~

will only be present at very high altitudes where the flow is strongly frozen. The assumption of continuum aerodynamics is questionable under these conditions. When the flow is a mixture of non-equilibrium and equilibrium flow, the modification of the shock position due to non-equilibrium effects is very small and consequently, the simpler stream tube method is equally applicable.

The relative simplicity of the stream tube method warrants its use wherever the assumptions involved in the calculations are justifiable. This is certainly the case when we try to apply our present understanding of the shock front radiation to a flow field situation.

In the case of the blunt body, the pressure distribution on the forward face is not affected by the chemistry and, consequently, a modified Newtonian assumption is satisfactory for describing the pressure distribution along the shock front and on the body surface for the forward face. Once the pressures on the shock and the body surface have been specified, stream tubes can be located by judicious use of the conversion laws and radial pressure gradients, assuming the flow is in thermodynamic equilibrium. From the streamline locations and the pressure field thus constructed, the pressure history along the streamlines can be determined. Using these pressure histories in terms of distance behind the shock front as an input, the shock front/stream tube chemistry calculation can be performed. Different normal shock strengths are used to identify the streamlines, i. e., shock strengths representative of the location along the shock wave where the streamline intersects the shock. The output of this program then gives the non-equilibrium flow parameters along each streamline.

The proposed calculation scheme assumes no significant differences in streamline locations between the equilibrium and non-equilibrium flow. Although this is a reasonable assumption, the shock front and stream tube positions could be recalculated from the non-equilibrium mass flow parameters by an iterative procedure to remove this restriction.

Once the non-equilibrium conditions have been determined for the flow along streamlines, the radiation field can be calculated by applying the semi-empirical procedure described previously for the normal shock case. Because of the pressure gradients present along streamlines in the blunt body case, and the subsequent acceleration of the flow, the radiation history must be calculated by determining the excitation process in particle time, i. e., the distances to the radiation peak which have been observed in the laboratory must be converted into distance, or time in a particle fixed coordinate system. The implicit assumption here is that the particle times to peak radiation and to the end of the non-equilibrium region are invariant in the normal shock and blunt body streamline cases, despite the pressure gradient differences.

The calculations described in the previous paragraphs have been carried out for a number of specific conditions. From these, as well as our knowledge of the scaling laws governing the various phenomena, we can estimate the radiative heating along the Apollo trajectory. One geometry and flight condition which has been calculated in detail, is a two-foot

~~CONFIDENTIAL~~

nose radius sphere flying at 35,000 ft/sec at an altitude of 200,000 ft (1959 ARDC atmosphere).⁴⁹ The results obtained from this calculation are in terms of the radiation along streamlines. It has been found more convenient, however, to cross plot the data and to present the results in terms of radiation along annular cuts taken at given radial distances. The annular profiles thus constructed for the example cited above, are shown in Fig. 29. Although the intensity of the radiation peak of the overshoot is considerably above the equilibrium value, non-equilibrium effects are restricted to a rather narrow region. Consequently, as an integrated effect, equilibrium radiation dominates. The integrated non-equilibrium radiation is only about one third of the total radiation seen by the body in the strong shock portion of the stagnation region. For the case of a one-foot nose radius body at the same speed and altitude, the non-equilibrium contribution was found to be the larger fraction of the total.

The values resulting from integrating under the profiles shown in Fig. 29 are shown in Fig. 30. The relative intensities due to equilibrium and non-equilibrium radiation are shown, as well as the total of the two contributions. It can be seen that the integrated radiation seen by the nose of a spherical body can be approximated quite closely by the normal shock value out to annuli of radius ratio, r/R_n , of at least 0.2 if not out to 0.3. This region includes angles of about 15° to the flight velocity vector. Outside this central region both equilibrium and non-equilibrium radiation drop rather rapidly and can, in many cases, be ignored completely. It is interesting to note that although in streamline co-ordinates, the non-equilibrium zone gets considerably wider for the outer streamlines, the thicknesses of the profiles at various annulus ratios do not vary much. The closer spacing of the stream tubes in the vicinity of the shock, corresponding to the increase in flow per unit area with increasing distance from the body in a direction normal to the surface, are felt to cause this result.

In the present calculation, the strongest radiation for the outer annuli emanates from the regions close to the body, and consequently from the gas along the streamlines which crossed the strong shock near the stagnation point. Excluding viscous and non-adiabatic effects, the radiation intensity along these streamlines maintains an intensity of about one third its normal shock value out to an annulus ratio of 0.7, whereas the radiation behind the oblique shock at this radius ratio has fallen by as much as two orders of magnitude from the stagnation point value. This is, of course, due to the differences in the entropy of the two streamlines. The stagnation streamline, having gone through a very strong shock has considerably higher entropy than the outer streamlines, say the one going through at 0.625 where the component of velocity normal to the shock is only 80% of U_∞ . However, under the Newtonian assumption, both have approximately the same pressure (different by the effect of radial pressure gradient only). The result is that the high entropy stagnation streamline air is considerably hotter than the lower entropy outer streamline directly behind the shock.

~~CONFIDENTIAL~~

As a consequence of this phenomenon, the radiative heat transfer does not show the rapid decrease with radius ratio, r/R_n , which would be predicted without considering stream tube flows. In Fig. 31, the equilibrium radiation distribution on an Apollo like vehicle presented by Wick⁴³ is compared to our present results. The results from the present calculation have been modified to account for the Apollo geometry, as shown in Fig. 30, by taking the radiation out to annulus ratio, r/R_n of 0.24. The flatness of our profile is strikingly different from the previous predictions.⁴³ The difference between these two results is not quite as striking as first apparent. The results of Wick⁴³ are in terms of the radiation seen by a point on the body at a given radial distance. Our results are in terms of the radiation coming from the gas at that point. At the edge of the body, where essentially no radiation would be seen from half of the solid angle, a correction of at most 1/2 should be made for this effect to the results presented. At other points the correction is progressively less moving toward the stagnation point.

The stagnation streamline will be the first to be effected by viscous and non-adiabatic effects. It appears, however, that there certainly will be a second radiation maximum along the body for the outer annuli. The first of the two above mentioned effects is beyond the scope of this report. The latter has been accounted for in the streamline chemistry program by writing the energy balance along a streamline in the form

$$\left(h_{\infty} + \frac{1}{2} u_{\infty}^2 \right) - \left(h_x + \frac{1}{2} u_x^2 \right) = \frac{10^7}{\rho_{\infty} u_{\infty}} \int_0^x 4\pi I(s) ds$$

where h_{∞} and h_x denote the specific enthalpy in the unshocked gas, and at a distance x behind the shock front, respectively, and s is the running variable along the streamline. For the example chosen, the energy loss at the stagnation point amounts to 1.59% of the incident kinetic energy. The total energy loss including the outer annulus ratios is, of course, much smaller due to the decrease in radiation with r/R_n .

The sphere calculations presented above can easily be scaled to the Apollo geometry, i. e., a relatively flat nose which is a segment of a sphere of 15.4 foot radius. Its outer edge is at a radius ratio of only 0.24. As with most hypersonic situations, only the face of the stagnation region is considered to be a serious source of radiative heating. As soon as the hot air starts to expand around the corner, it is quenched and is no longer a serious source of radiative heating.

The flatness of the Apollo stagnation region allows one to use the results of the inner portion of the sphere calculation discussed above. Indeed, it was shown in the above discussion that the normal shock assumption is an excellent approximation for such small values of r/R_n , and should suffice for most purposes. The larger size of the sphere merely adds more equilibrium radiation to the values calculated for the two-foot nose radius

~~CONFIDENTIAL~~

~~CONFIDENTIAL~~

body due to the considerably larger stand-off distance. As the radiation from most of the inviscid flow is already due to equilibrium air, a good approximation is to multiply the integrated equilibrium radiation by the pertinent radius ratio, in this case, 7.7. The resultant total radiation for the Apollo geometry at 200,000 feet and 35,000 ft/sec at the stagnation point is 748 watts/cm², only 69 watts/cm² of which is due to the non-equilibrium effect.

Another point along the Apollo trajectory can be scaled from the examples cited. As the non-equilibrium overshoot has been shown to be a binary phenomenon, the two-foot nose radius body at 200,000-foot altitude can be scaled into a 15.4-foot nose radius body at a factor of 7.7 less in density. This altitude turns out to be almost exactly 250,000 feet. The non-equilibrium region, thus scales merely by dividing the intensity everywhere by 7.7 and by multiplying the time or distance scale by the same value. The equilibrium intensity must be recalculated for the new density because of its stronger density dependence in this temperature region. Consequently, the point at which equilibrium is approached is somewhat later than would be predicted by direct binary scaling from the 200,000-ft altitude case. As has been discussed in other discussions of binary scaling,^{5, 50} this is precisely the region in which this type of scaling breaks down. Thus, the non-equilibrium distance is not achieved by binary scaling but by fairing the non-equilibrium radiation into the equilibrium value.

The net result is that although ρR is the same value in both cases, the non-equilibrium region is slightly larger relative to the stand-off distance for the lower density case. Due to binary scaling, the absolute magnitude of the integrated non-equilibrium intensity is essentially unchanged while the equilibrium contribution has decreased significantly due to the drop in density by a factor of 7.7. The non-equilibrium effect is now the dominant contribution to radiative heating. The profiles along the annular radial cuts are shown in Fig. 32.

The calculation scheme described has been used to estimate the radiation history for the Apollo vehicle. For the purpose of this study, the undershoot boundary⁵¹ for a vehicle with a lift/drag ratio of one half was used. The trajectory was calculated for a ballistic parameter, W/C_{DA} , of 50 and the re-entry angle yielding a peak deceleration of 10 g's was chosen. Only initial pull out portion of the trajectory up to level flight was considered because the radiative heating problems are most severe at this time. Once level flight is achieved, the remaining trajectory does not yield a unique velocity-altitude relationship. Rather, the velocity-altitude combination is a compromise designed to achieve the desired range.

The other extreme trajectory often considered, is the so called overshoot boundary.⁵¹ One limiting value of this maneuver is the equilibrium glide path at supercircular velocity with a negative lift/drag ratio of 0.5. This part of the trajectory must be joined by a proper pull-up maneuver at a positive lift/drag ratio of 0.5. Along this trajectory, the minimum

~~CONFIDENTIAL~~

altitude is approximately 240,000 ft at which time the velocity is about 33,000 ft/sec. Because of the variations possible on this maneuver, detailed radiation histories have not been determined but will be discussed only qualitatively.

Figure 33 shows the time histories of the radiative intensity radiated toward the body at the stagnation point, for both equilibrium and non-equilibrium radiation, along the 10 g undershoot trajectory. The equilibrium radiation has the usual sharply peaked shape. The rise is due to the density increase at approximately a constant velocity and the fall is due to the velocity decay. The absolute value of the equilibrium radiation, shown in this Figure, may be somewhat high in view of the experimental indications that the data of Ref. 6 overestimates the actual situation for Kramer's radiation.

The non-equilibrium radiation has a more unusual time history. The rapid initial rise is due to the loss of severe truncation below 300,000 ft. Above this altitude, the distance to the non-equilibrium peak is larger than the shock detachment distance and the radiation drops rapidly (with the square of the density). In the present calculation, no collision limiting has been considered to occur. Once the non-equilibrium shock front region is approximately equal to the shock detachment distance, the so called non-equilibrium plateau is reached where the integrated radiation becomes independent of density. The slow decay of the absolute magnitude of this radiation is due to the velocity decay. At the end of the pull-up maneuver, at 28,000 ft/sec and about 190,000 ft altitude, the non-equilibrium radiation is down to about 10 watts/cm² at the stagnation point.

Along the undershoot boundary, the non-equilibrium radiation should have a similar characteristic, in terms of the radiation intensity-velocity relationship. The time duration will be significantly stretched because of the longer times required to decelerate the vehicle to corresponding velocities at the higher altitudes. The equilibrium radiation, however, will be significantly lower than shown in Fig. 33, indeed, the peak value will be less than 50 watts/cm². Thus the non-equilibrium radiation will exceed the equilibrium value along the overshoot boundary.

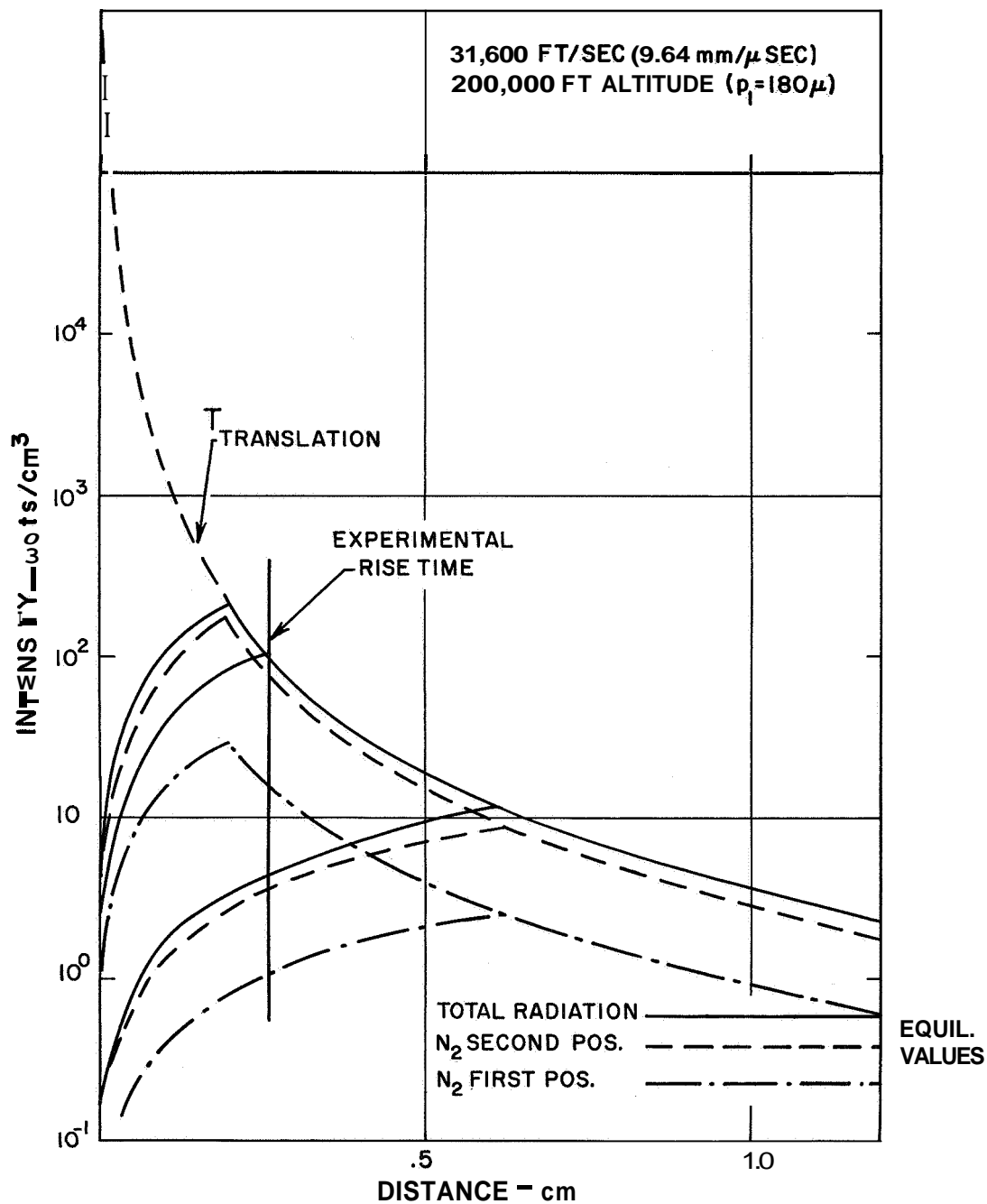


Fig. 26 Radiative intensity due to the nitrogen molecule first and second positive band systems, calculated under the assumption that the radiation is in local equilibrium with the translational temperature everywhere. The two linear rises of intensity were calculated to determine the effect of radiation energy losses. The intermediate linear rise represents the measured time to peak radiation for these conditions.

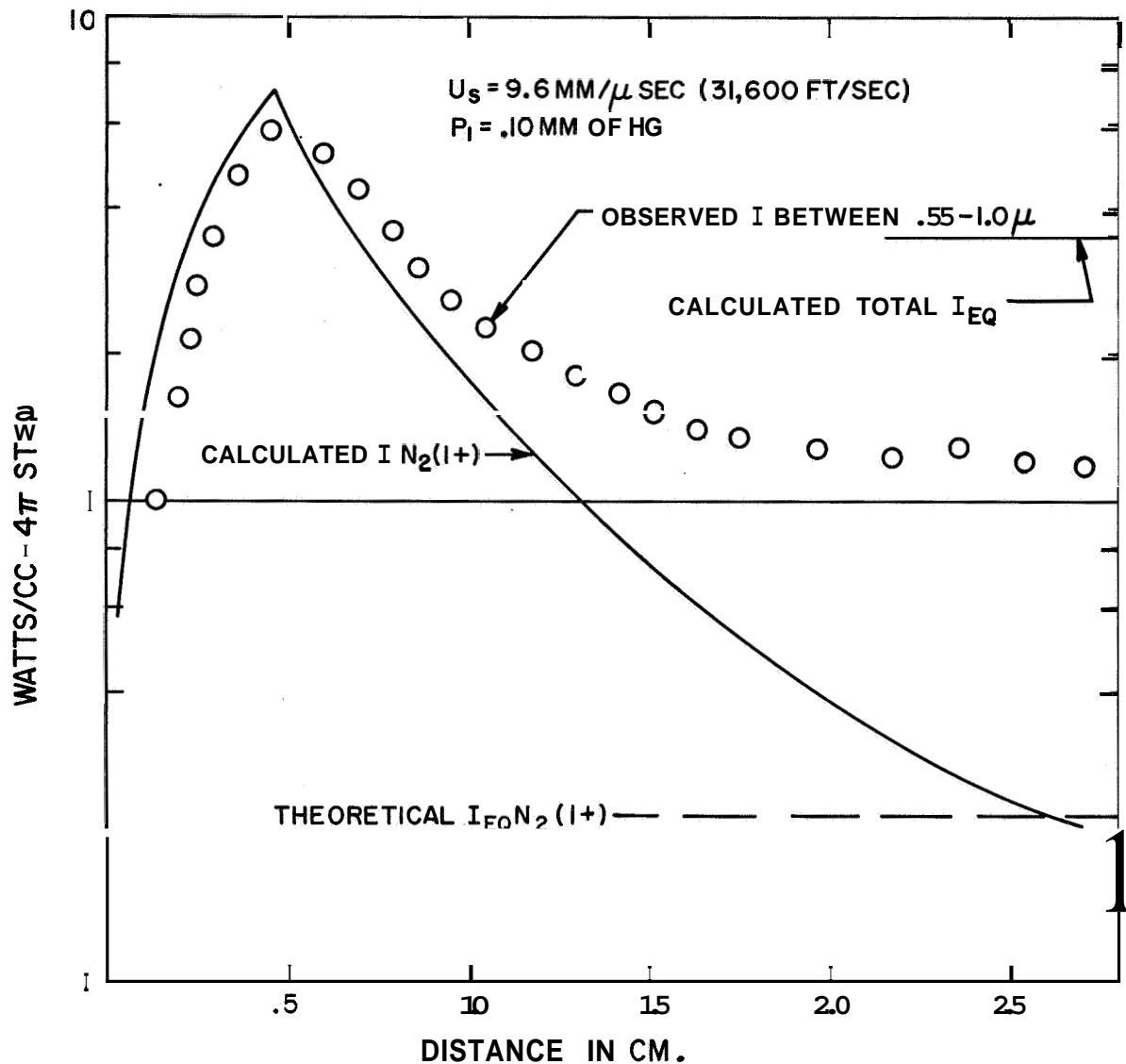


Fig. 28 Calculated profile of nitrogen molecule, first positive band system radiation, and the measured profile in the wavelength interval from $.55$ to 1.0μ . The experimental profile is postulated to be produced by the overshoot of the $N_2(1+)$ radiation followed by the decay to the total equilibrium value which in this wavelength region should have strong contributions due to Kramer's radiation and atomic nitrogen lines. The fairing of the $N_2(1+)$ overshoot into the total radiation is the model used in these calculations.

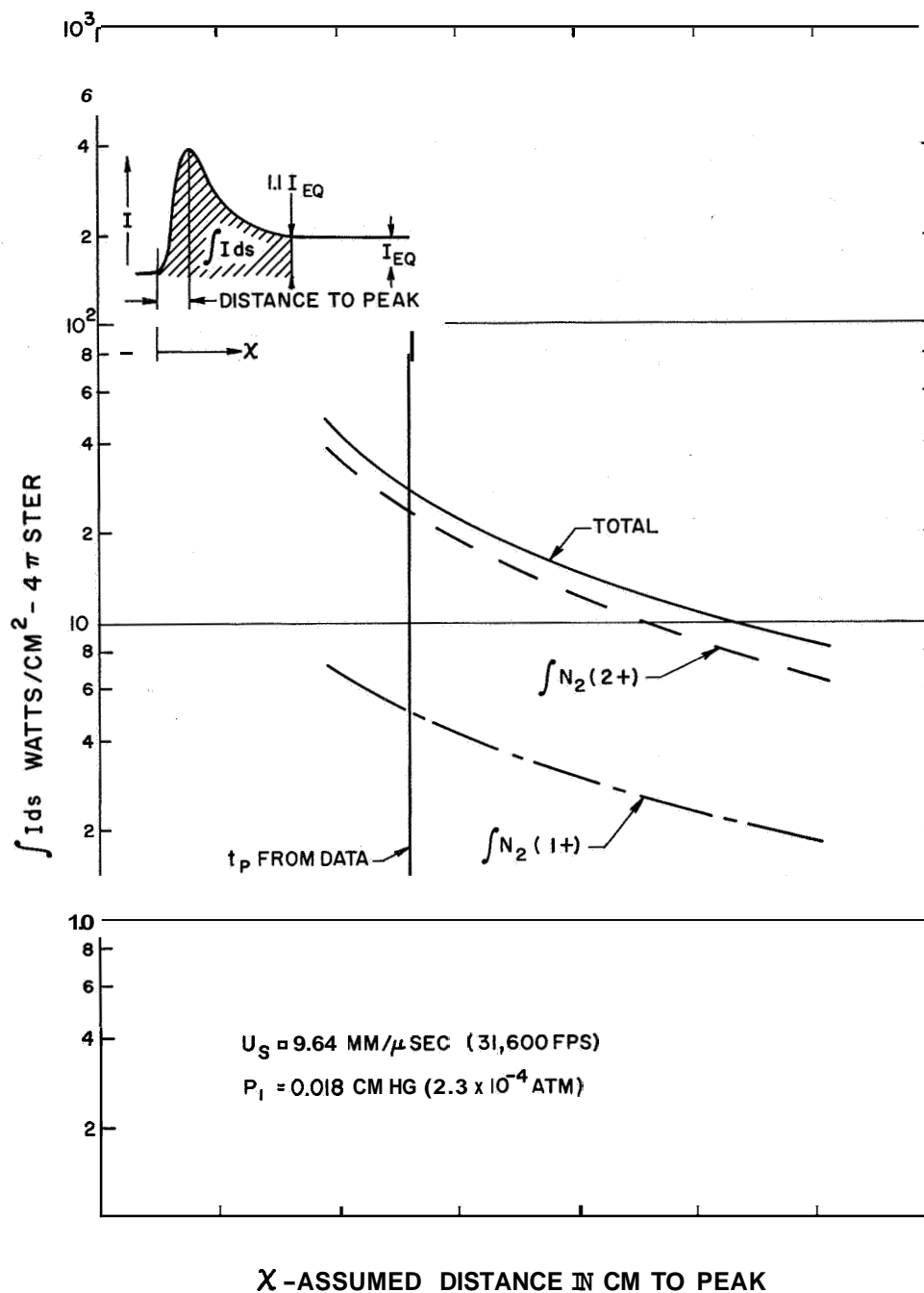


Fig. 27 Total non-equilibrium radiation resulting from integrating Fig. 26, using various values of excitation time. Where radiation losses become significant, separate radiation decay curves must be drawn for each rise time.

CONFIDENTIAL

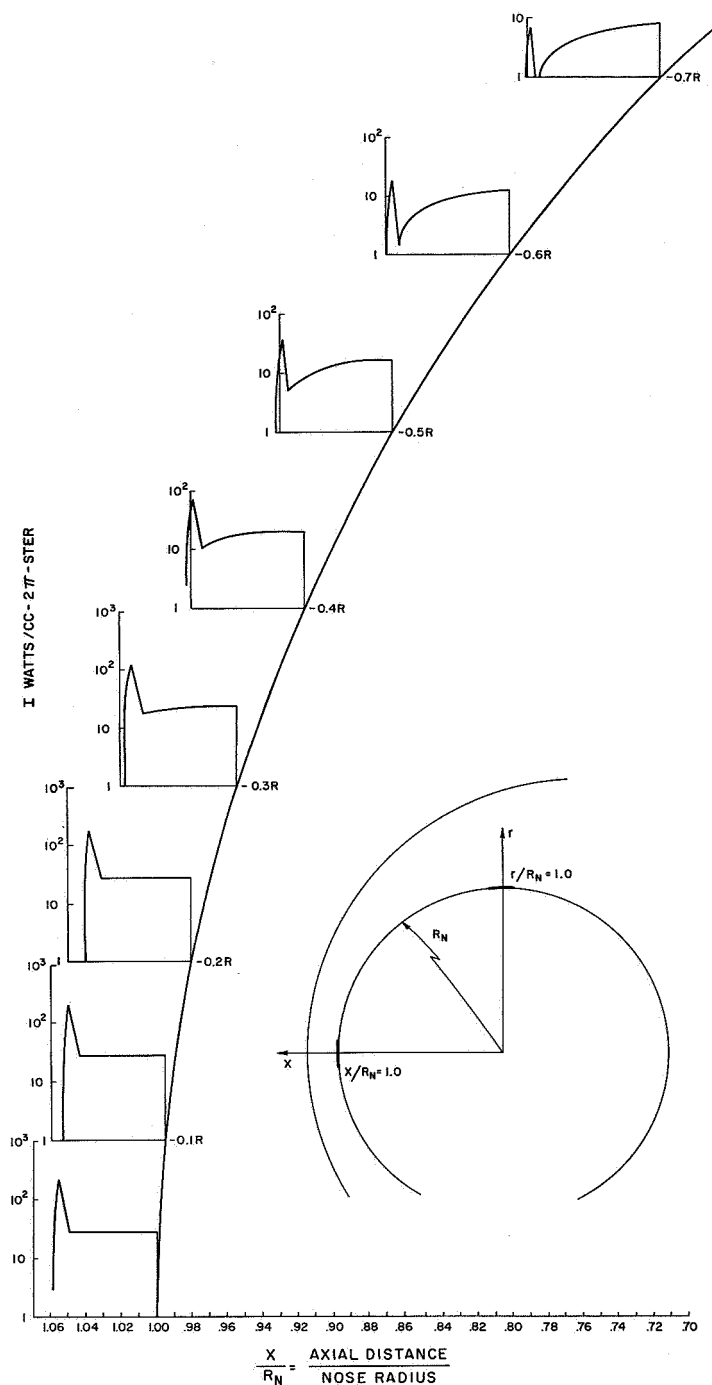


Fig. 29 Radiation profiles along annular cuts through the inviscid flow around a spherical nose body with a two foot radius, flying at a 200,000 foot altitude. Note that for the inner radii, the normal shock is a very good approximation, while at the outer radii, the isentropically expanded stagnation region air gives considerably more radiation than the gas at the shock at the same radius.

~~CONFIDENTIAL~~

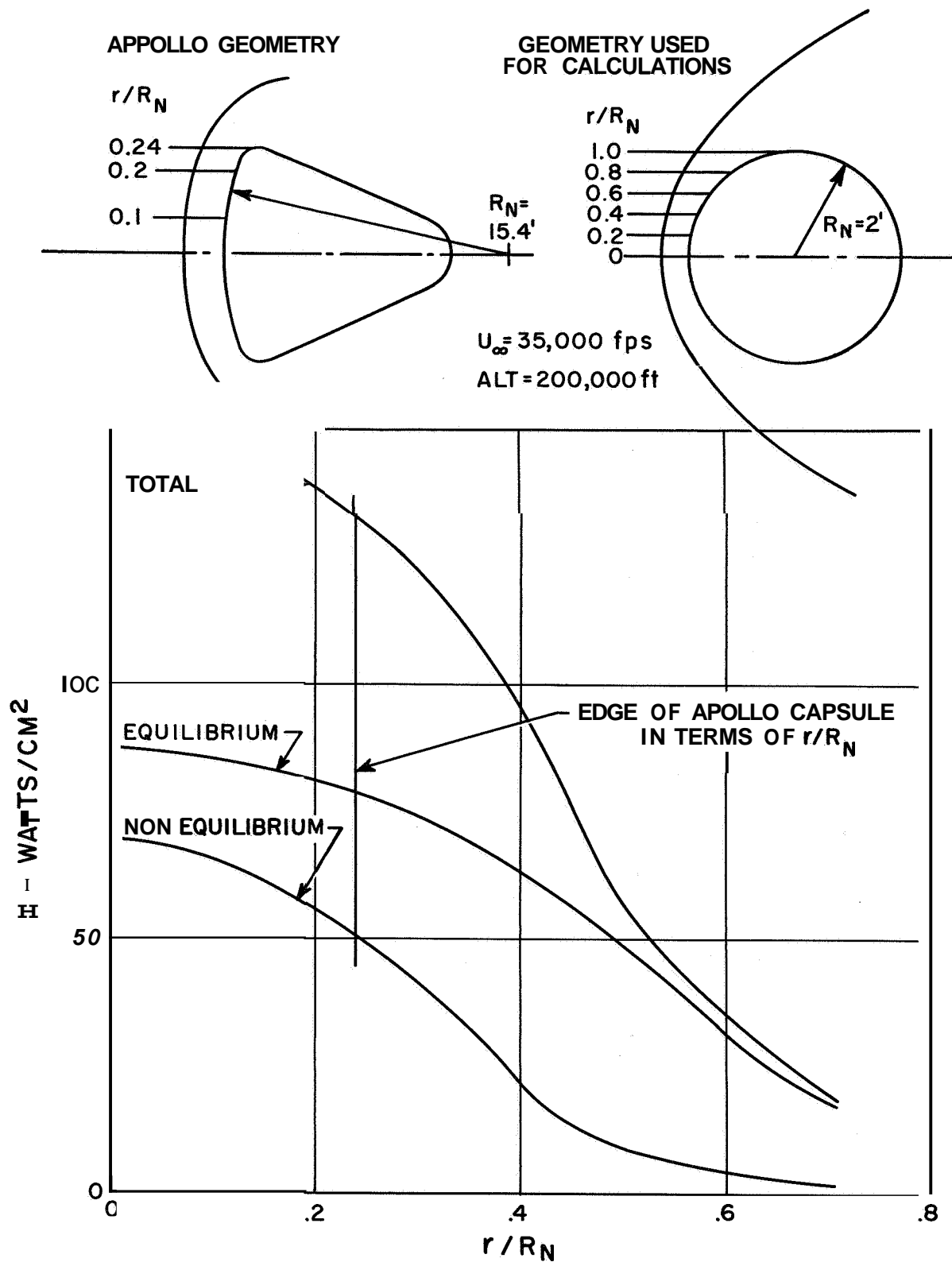


Fig. 30 Distribution of equilibrium, non-equilibrium and total radiation for a two foot nose radius sphere flying at a 200,000 foot altitude at 35,000 ft/sec. This is the distribution available in the flow which is not quite the same as the distribution seen by the body surface.

~~CONFIDENTIAL~~

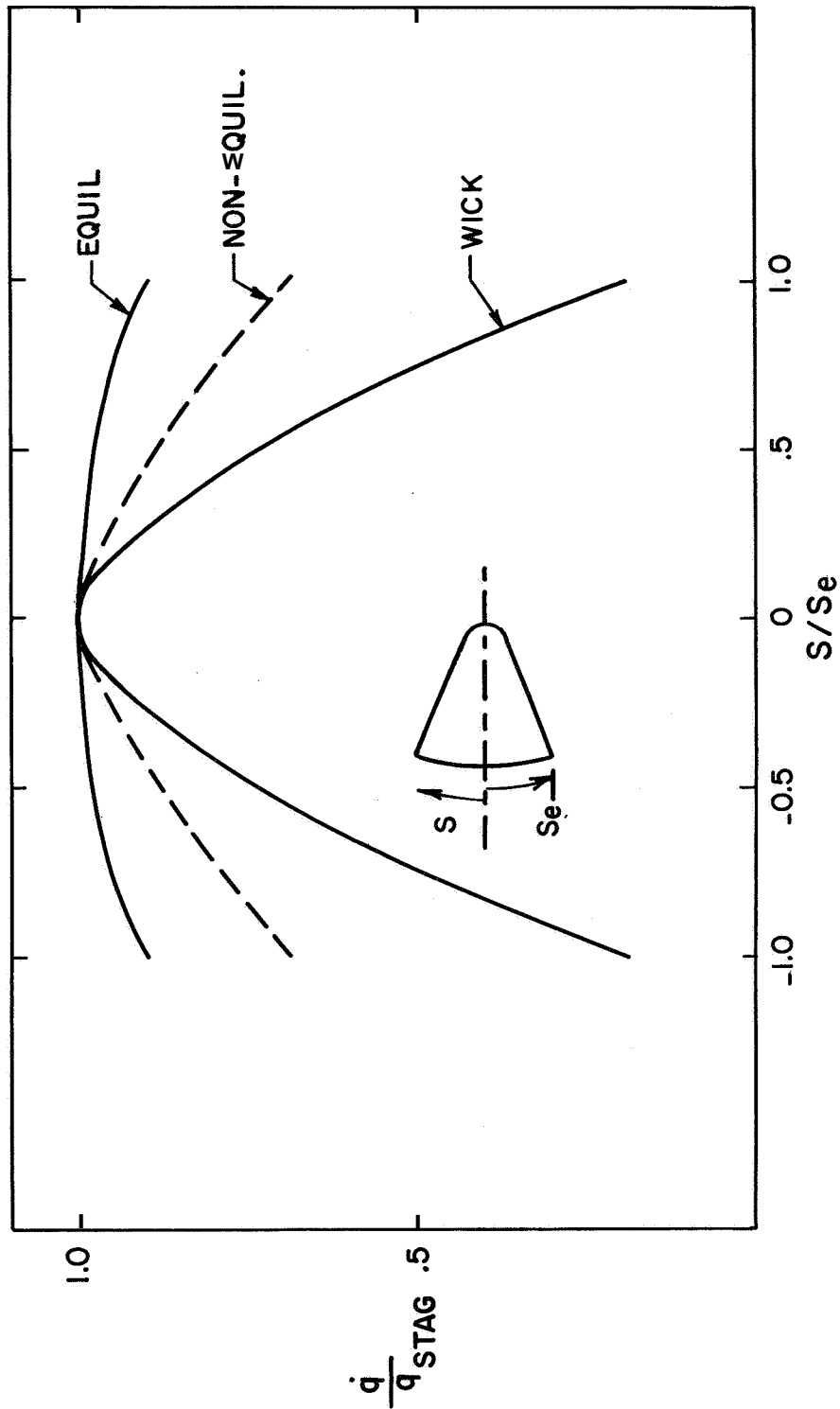


Fig. 31 Radiative heat flux distribution for an Apollo geometry from the present analysis compared to Wick's⁴³ presentation based on equilibrium radiation without considering streamtube curvature. Note that the data from this calculation is in terms of the distribution of the radiation, while Wick's data is in terms of the radiation seen by a point on the body surface. The difference between these two methods is no larger than a factor of two at the extreme edge of the body.

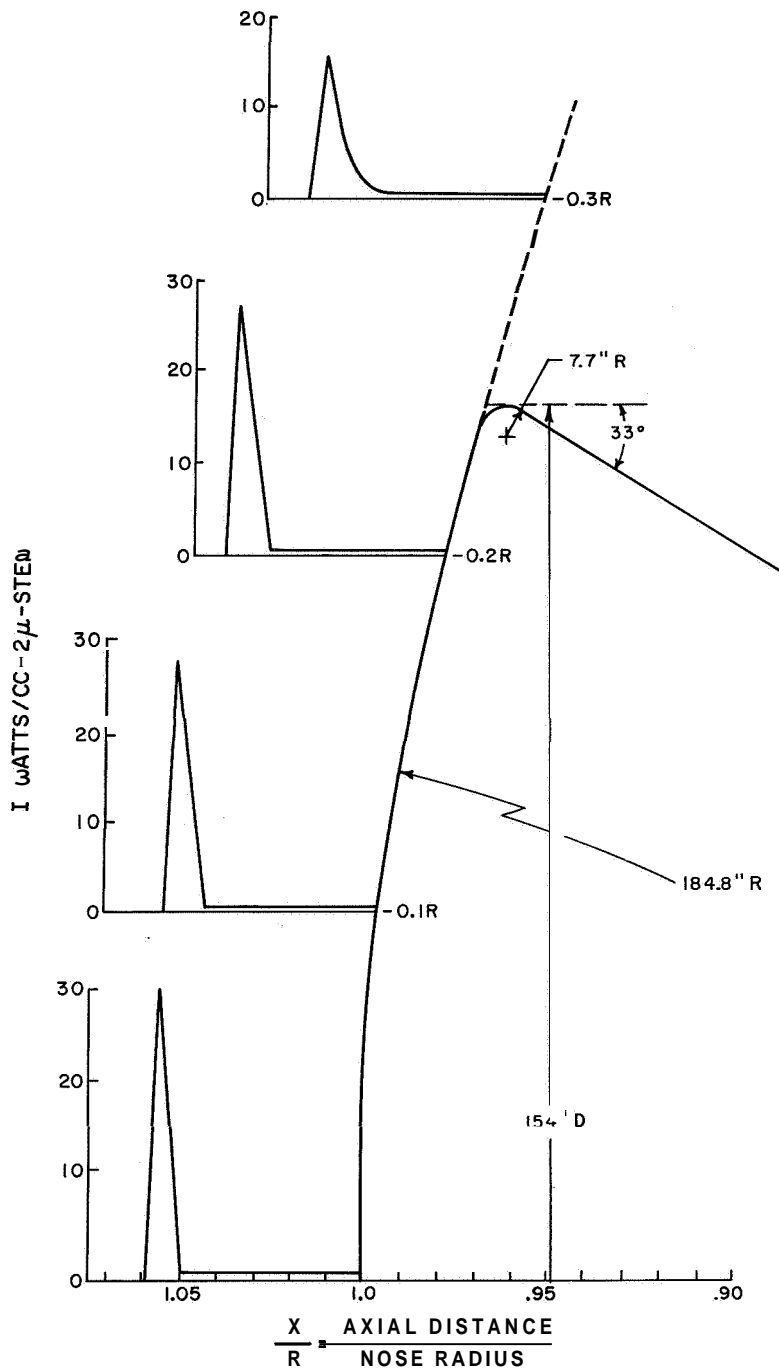


Fig. 32 Radiation profiles along annular cuts through the inviscid flow around the Apollo body, as shown, flying at 35,000 ft/sec at an altitude of 250,000 feet. Note the normal shock is a good approximation for the whole body.

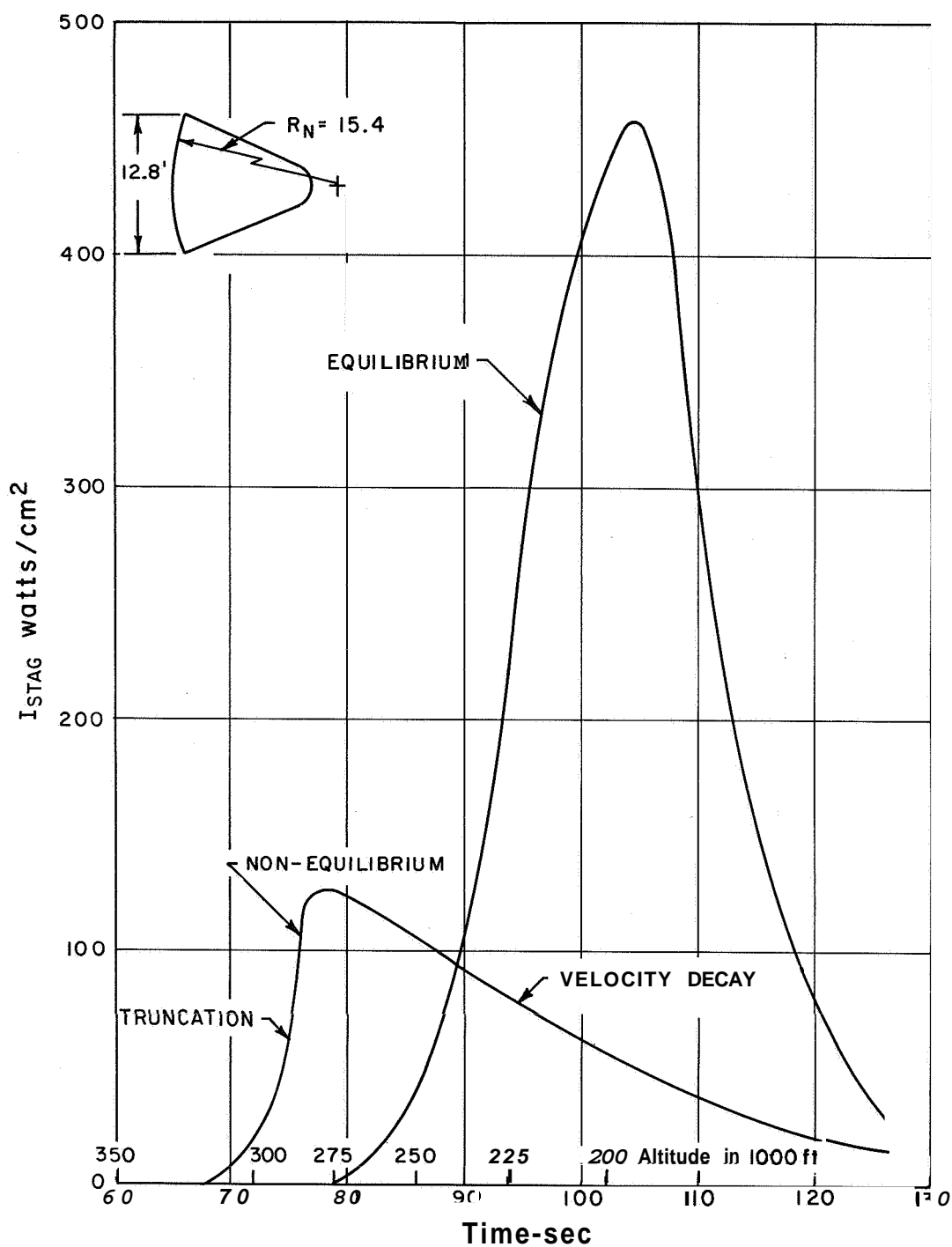


Fig. 33 Time history of radiation seen at the stagnation point of the Apollo vehicle re-entering above the 10 g undershoot boundary trajectory.

~~CONFIDENTIAL~~

THIS PAGE IS BLANK

-68-

~~CONFIDENTIAL~~

~~CONFIDENTIAL~~

IX. SUMMARY

Investigations performed in connection with an experimental and theoretical study of the non-equilibrium radiation from high temperature air under the conditions encountered by the Apollo re-entry vehicle have been discussed in this report. The experiments have been performed by observing the radiation produced by strong normal shock waves in air. The shock waves were produced by an arc-driven shock tube capable of shock strengths of over 40,000 ft/sec.

Most of the measurements were made by calibrated monochromators and photomultipliers. Some data was achieved by photoelectric gauges, infrared detectors, heat transfer gauges and photographic techniques. Although the wavelength coverage was limited in some regions, the absolute spectral distribution of the non-equilibrium radiation was synthesized by repeated measurements with a narrow band width. Integration of the spectral distribution has allowed us to estimate an upper limit for the total non-equilibrium radiative heat flux.

As a by-product of the non-equilibrium measurements, absolute equilibrium radiation data were also collected. New data on Kramer's radiation indicate this source to be less than previous estimates. However, atomic line radiation was observed which previously had not been seen in laboratory experiments. These two observations left many unanswered questions about radiation from air at temperatures of 10,000°K and above.

A theory of non-equilibrium radiation from air is still beyond our present understanding of the phenomenon. The greatest unknown appears to be the excitation mechanism whereby the energy originally in the heavy particles is transferred to the electronic states. Experiments have been performed which circumvent the need for this knowledge and allow a semi-empirical calculation procedure of non-equilibrium radiation which shows reasonable agreement with the measurements. This procedure has been applied to the blunt body flow problem and has produced estimates of the radiative heating problem for the Apollo vehicle.

The major questions which have been left unanswered regard the absolute magnitude of the equilibrium radiation due to Kramer's radiation and atomic lines. Several regions in the spectrum, such as the ultraviolet and the near infrared should receive additional coverage to guarantee that no significant radiators are present at wavelengths not covered at present. The excitation mechanisms by which excited electronic states are produced also requires much further study. Finally, the methods by which our knowledge of shock front radiation can be applied to the flow about bodies must be improved as our theoretical and empirical knowledge of the radiation phenomenon is advanced.

CONFIDENTIAL

ACKNOWLEDGEMENT

The authors wish to acknowledge the enthusiastic support given this work by A. R. Kantrowtiz, Director of the Avco-Everett Research Laboratory.

We wish to give credit to I. Frank who performed the calculation presented in the Appendix and to J. C. Camm who was mainly responsible for the development of the electric shock tube.

We also wish to express appreciation for the many helpful suggestions provided by J. C. Keck and M. Camac.

CONFIDENTIAL

APPENDIX A

GEOMETRICAL CONDITIONS FOR RADIATION MEASUREMENTS WITH INFRARED HEAT TRANSFER GAUGES

A. Evaluation of Geometry Factors

In order to improve the gauge ability to discrimination between the test gas and the driver gas radiation, two gauge geometries have been proposed to mask the gauge from the driver gas. The first method is the use of a recessed gauge, Fig. A-1, called Type I.

In this gauge, the maximum distance the gauge can see is x_D , where $x_D = 2a \cot \alpha$, as measured from the end of the knife edge designated as $x = 0$. It is desired to find the angle of inclination α which gives the best view of the region from $x = 0$ to $x = x_D$.

The second method for restricting the vision of the gauge is to mount a shield in front of the gauge which is mounted in the center of the shock tube, Fig. A-2.

In this geometry, the maximum view of the gauge is given by $x_D = a \cot \alpha$. For this type of gauge the test will be at an end when the shock front reaches the obstruction.

Considering the recessed, Type I, gauge, Fig. A-1, the geometry factor $\Omega(x)$ for a thin slug of gas per unit steradian is given by

$$\Omega(x) = \iint \frac{\cos \phi}{r^2} dA \quad (1)$$

The origin of the coordinate system is at the knife edge. It can be shown that

$$\cos \phi = \frac{(x + c) \sin \alpha - (z + b) \cos \alpha}{[(x + c)^2 + y^2 + (z + b)^2]^{1/2}}$$

and Eq. (1) becomes

$$\Omega(x) = \iint \frac{(x + c) \sin \alpha - (z + b) \cos \alpha}{[(x + c)^2 + y^2 + (z + b)^2]^{3/2}} dA \quad (2)$$

In cylindrical nondimensional coordinates, we have

$$\Omega(x) = \iint \frac{R [x' \sin \alpha - (R \sin \theta + b') \cos \alpha] dR d\theta}{[x'^2 + b'^2 + 2b' + R \sin \theta + R^2]^{3/2}} \quad (3)$$

where

$$R \cos \Theta = y/a = y'$$

$$R \sin \Theta = z/a = z' - b'$$

$$x' = \frac{x + c}{a}$$

$$b' = b/a$$

The region of integration for Eq. (3) is a segment of a circle bounded below by a line $z = x \tan \beta$.

$$\Omega(x) = 2 \int_{\Theta_0}^{\pi/2} d\Theta \int_0^1 \frac{R [x' \sin \alpha - (R \sin \Theta - b') \cos \alpha] dR}{[x'^2 - b'^2 - 2b'R \sin \Theta + R^2]^{3/2}}$$

$$-2 \int_0^{a \cos \Theta_0} dy \int_{1-b'}^{1+b'+y' \tan \Theta_0} \frac{(x' \sin \alpha - z' \cos \alpha) dz}{(x'^2 - y'^2 - z'^2)^{3/2}} \quad (4)$$

where

$$\Theta = \sin^{-1} \left| \frac{n \beta - 1}{n} \right|$$

The above expression for $\Omega(x)$ is the sum of certain elementary functions and elliptic integrals of the first, second, and third kind.

For a flush gauge, i. e., for $\alpha = \pi$, $b = c = 0$, we obtain

$$\Omega(x) = -2 \int_{-\pi/2}^{\pi/2} \frac{\sin \Theta d\Theta}{[x'^2 - 2 + 2 \sin \Theta]^{1/2}} \quad (5)$$

Equation (5) can be reduced to the difference of two complete elliptic integrals. In terms of these integrals we obtain for Eq. (5)

$$\Omega(x) = \sin y [(x'^2 - 2) K(y) - (x'^2 - 4) E(y)] \quad (6)$$

where

$$\sin y = \frac{2}{(x'^2 + 4)^{1/2}}$$

~~CONFIDENTIAL~~

and

$$K(\gamma) = \int_0^{\pi/2} \frac{d\phi}{[1 - \sin^2 \gamma \sin^2 \phi]}$$

$$E(\gamma) = \int_0^{\pi/2} [1 - \sin^2 \gamma \sin^2 \phi] d\phi$$

Figures A-3, A-4, A-5, and A-6 show the values of $\Omega(x)$ as a function of x for $x'_D \equiv x_D/a = .5, 1.0, 1.5$ and 2 respectively, for various values of the parameter, r . Also shown in Fig. A-6 are the geometry factors for the flush gauge. It can be seen that $\Omega(x)$ is a maximum for each x'_D when $\alpha = 180^\circ$.

It can be shown that for the Type II gauge, Fig. A-2, the geometry factor, $\Omega(x)$ per steradian is given by

$$\Omega(x') = x' \int_0^{2\pi} d\theta \int_{x' \tan \alpha}^1 \frac{r' dr'}{(x'^2 + r'^2)^{3/2}} \quad (7)$$

where

$$x' = x/a, \quad r' = r/a$$

and the coordinate system with respect to the gauge is the same as used for the Type I geometry.

Thus the geometry factor for the Type II gauge is per steradian

$$\Omega(x) = 2\pi \left[\cos \alpha - \frac{x'}{(x'^2 + 1)^{1/2}} \right] \quad (8)$$

The values of $\Omega(x)$ for the Type II gauges for which $\alpha = \cot^{-1} x'_D$ are also shown in Figs. A-3, A-4, A-5, and A-6.

B. Evaluation of Total Heat Energy Absorbed for the Gauge

For shock waves moving with constant velocity, u_s , and with a radiation one-dimensional profile I (A) invariant with time, the heat absorbed from cross-section A by the gauge when the shock front is at position x_1 ,

~~CONFIDENTIAL~~

~~CONFIDENTIAL~~

where $x = 0$ at the gauge, is

$$\int_{t_0}^{t_1} q(A) dt = \int_{t(x'_D)}^{t(x_1 + A)} I(A) \Omega[x(t)] dt = I(A) \int_{t(x_D)}^{t(x_1 + A)} \Omega[x(t)] dt \quad (9)$$

When x'_D is taken to be so far away from the gauge that $\Omega[x'_D(t)] = 0$, and denoting the time the arrival of the shock at the gauge by t_s , we obtain the position of cross-section A with respect to the gauge as $x(t, A) = x_1 + A t u_s (t_s - t)$. Equation (9) becomes

$$\int_{t_0}^{t_1} q(A) dt = \frac{I(A)}{u_s} \int_{x_1 + A}^{x'_D} \Omega(x) dx = \frac{I(A)}{u_s} \int_{x_1 + A}^{x'_D} (x') dx' \quad (10)$$

Similarly for cross-section B, for the same condition that the shock front is at $x = x_1$,

$$\int_{t_0}^{t_1} q(B) dt = a \frac{I(B)}{u_s} \int_{\frac{x_1 + B}{a}}^{x_D} (x') dx' = \frac{I(B)}{u_s} W(x_1 + B) \quad (11)$$

Thus the total heat input from all cross-sections at a time when the shock front is at the position $x = x_1$, is

$$Q_{\text{total}} = \frac{1}{u_s} \int_0^{x_D - x_1} I(y) W(x_1 + y) dy \quad (12)$$

Where y is a coordinate in the x direction which is zero at the shock front.

At the time of shock arrival, Eq. (13) becomes

$$Q_{\text{total}} = \frac{1}{u_s} \int_0^{x_D} I(y) W(y) dy \quad (13)$$

~~CONFIDENTIAL~~

~~CONFIDENTIAL~~

If a gauge with poor thermal contact to the backing is irradiated by this heat input, the temperature in the gauge can be considered to be the total heat input divided by the heat capacity of the gauge. It is assumed that there are no thermal gradients in the gauge. Thus we obtain

$$T(x_1) = \frac{1}{2\pi u_s \rho c l} \int_0^{x_D - x_1} I(y) W(x_1 + y) dy \quad (14)$$

We define a parameter T^* , where $T^* = (T u_s / I) (10^{-6})$, which is a measure of the sensitivity of the gauge. With $I(y)$ taken to be a constant. Thus

$$T(x_1) = \frac{I}{2\pi u_s \rho c l} \int_{x_1}^{x_D} W(y) dy, \quad T^*(x_1) = \frac{2\pi}{\rho c l} \int_{x_1}^{x_D} W(y) dy \quad (15)$$

A comparison of T^* vs x_D for the best Type I and Type II gauges is shown in Figs. A-7 and A-8 for various values of x_D . The properties of carbon used for $(\rho c l)$ gave the product as $8 \times 10^{-5} \text{ cal/cm}^2 \text{ } ^\circ\text{C}$.

From Fig. A-8, $T^*(0)$ for the Type II gauge = 670×10^{-5} for a value of $x'_D = 1.00$. Thus for $I = 418 \text{ watts/cm}^2$, $u_s = 1 \times 10^6 \text{ cm/sec}$, we obtain

$$T(0) = \frac{100 (670 \times 10^{-5}) \times 10^6}{1 \times 10^6 (2\pi)} = .11 \text{ } ^\circ\text{C}$$

for a shock tube with a one cm radius.

Thus a capability of detecting a temperature rise of $0.1 \text{ } ^\circ\text{C}$ would allow us to measure an equilibrium radiation level of only 54 watts/cm^2 in a six-inch diameter shock tube.

~~CONFIDENTIAL~~

~~CONFIDENTIAL~~

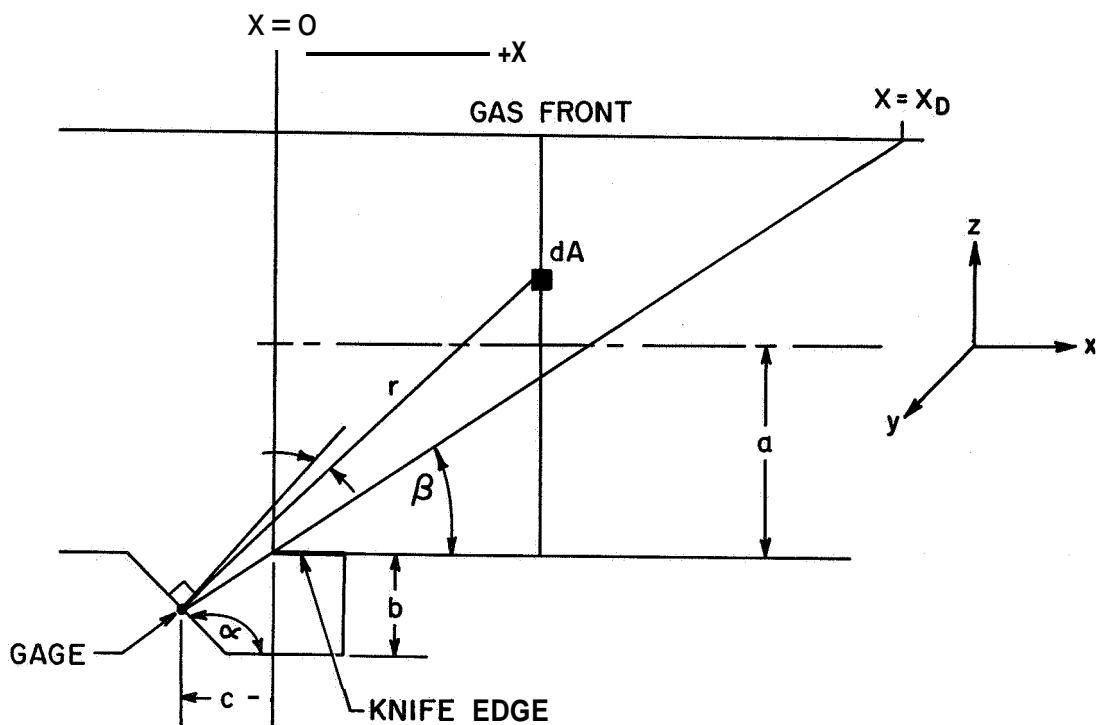


Fig. A-1 Type I Geometry

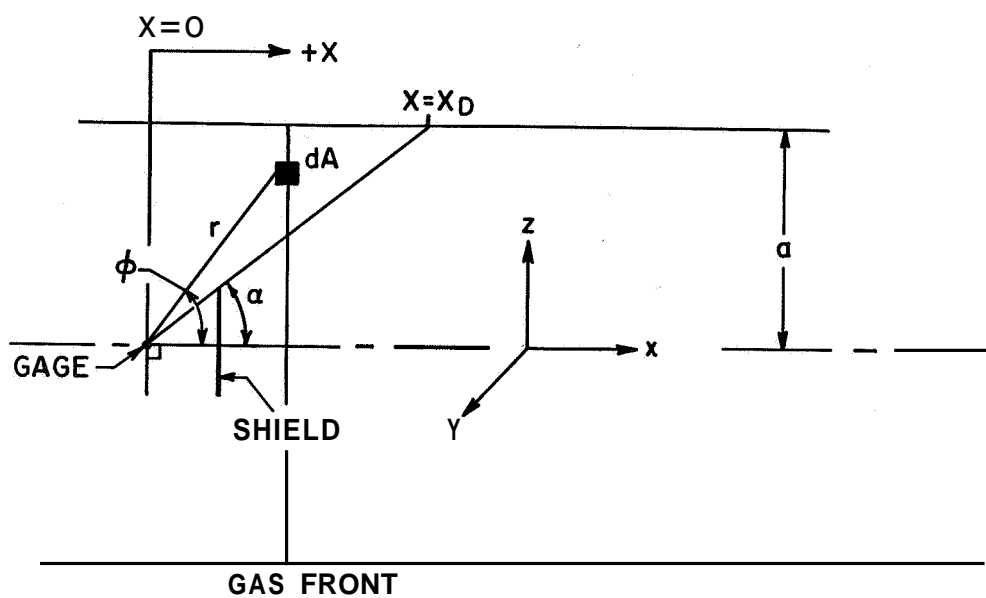


Fig. A-2 Type II Geometry

~~CONFIDENTIAL~~

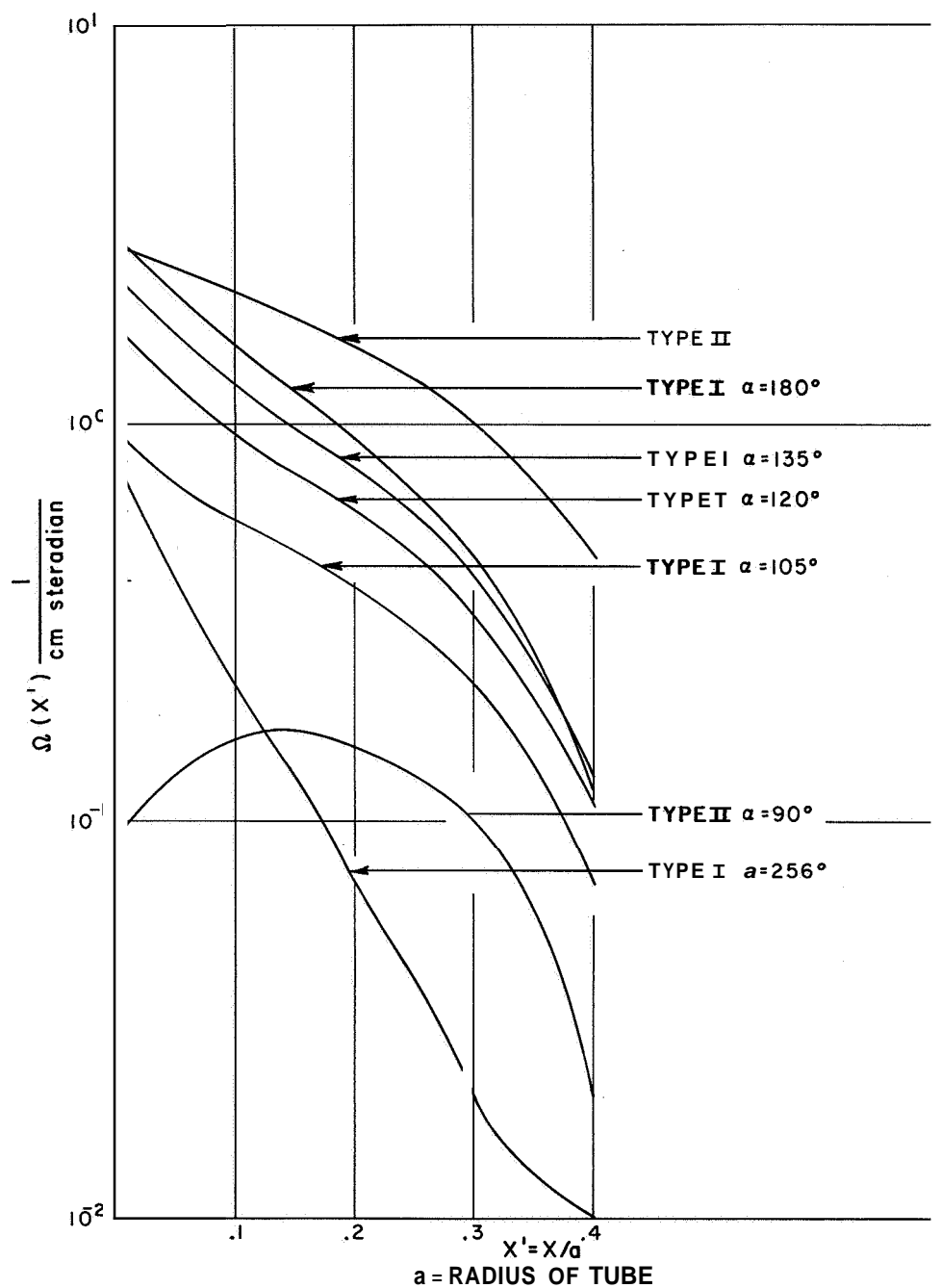


Fig. A-3 Geometry factors, $\Omega(x')$, for infrared gage, $x'_D = 0.5$.

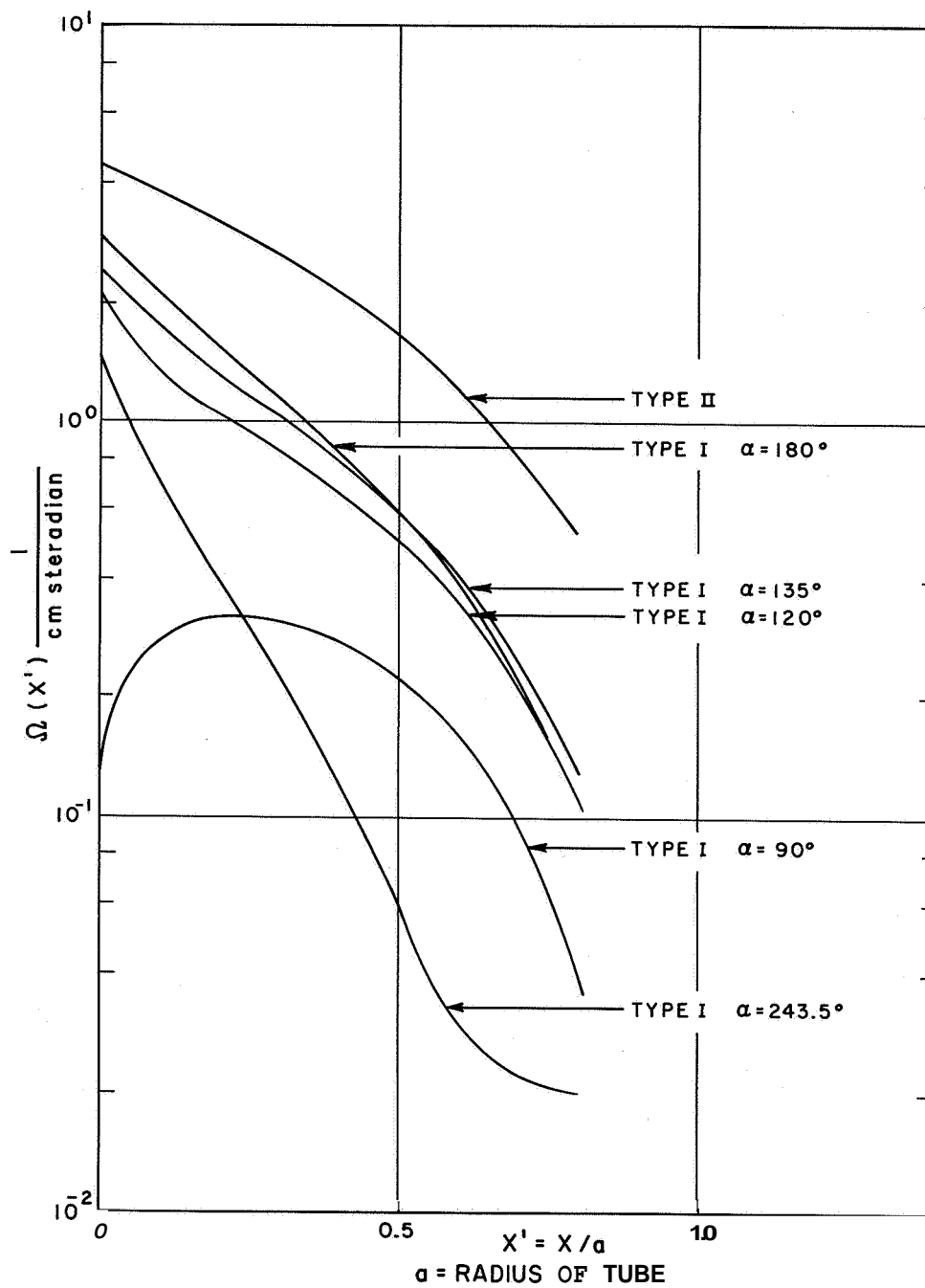


Fig. A-4 Geometry factors, $\Omega(x')$, for infrared gage, $x'_D = 1.0$.

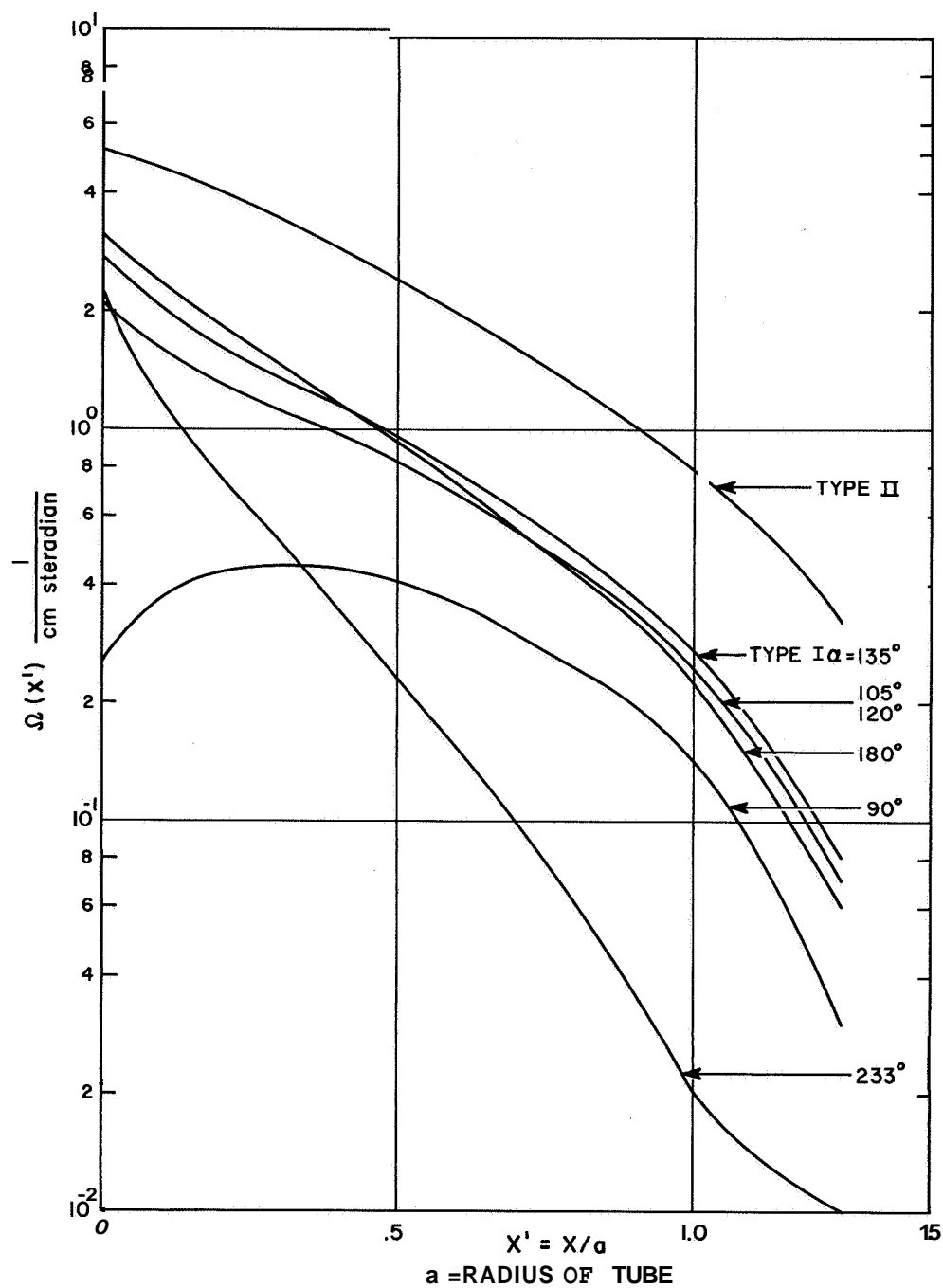


Fig. A-5 Geometry factors, $\Omega(x')$, for infrared gage, $x'_D = 1.5$.

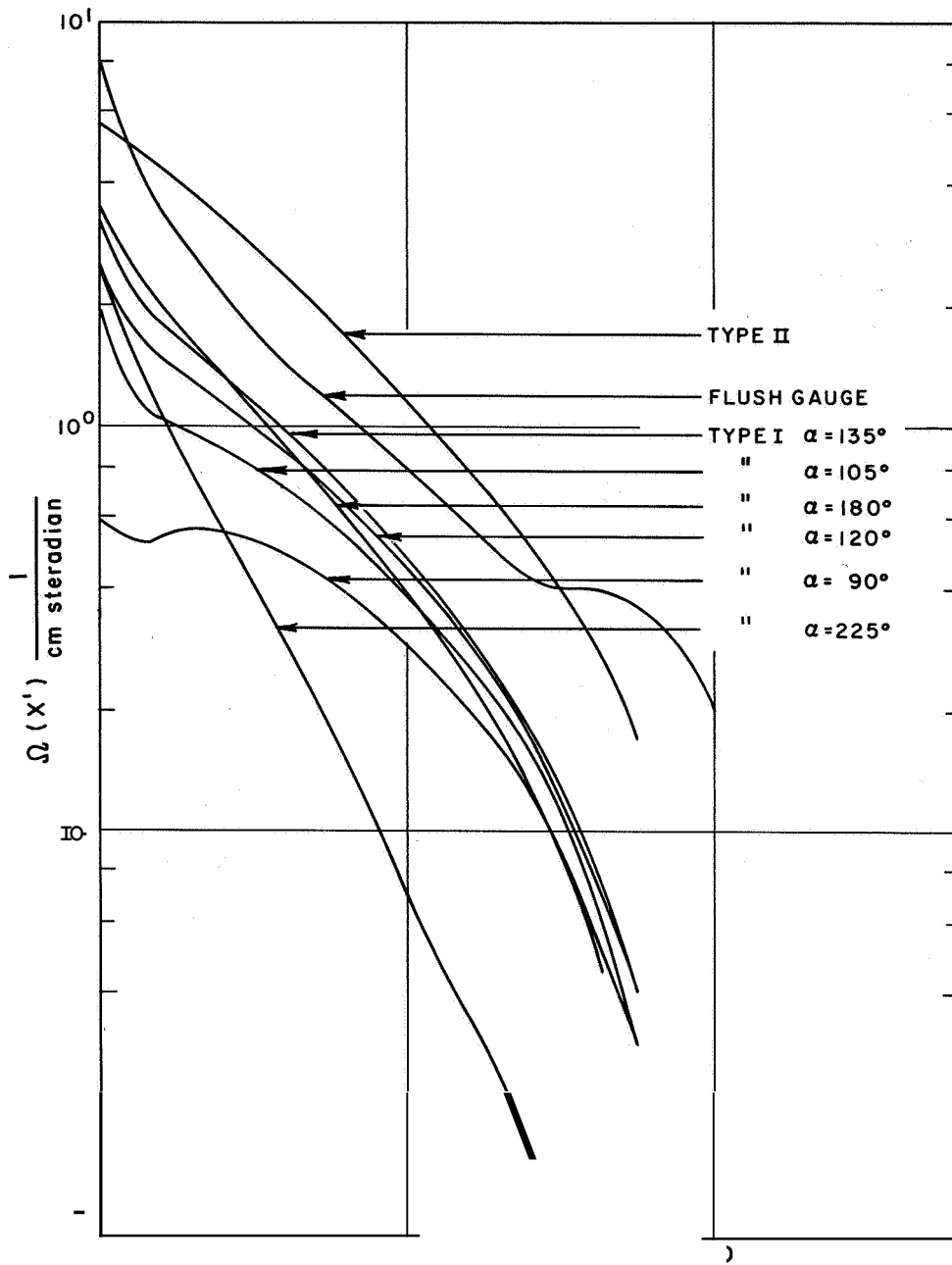


Fig. A-6 Geometry factors, $\Omega(x')$, for infrared gage, $x'_D = 2.0$

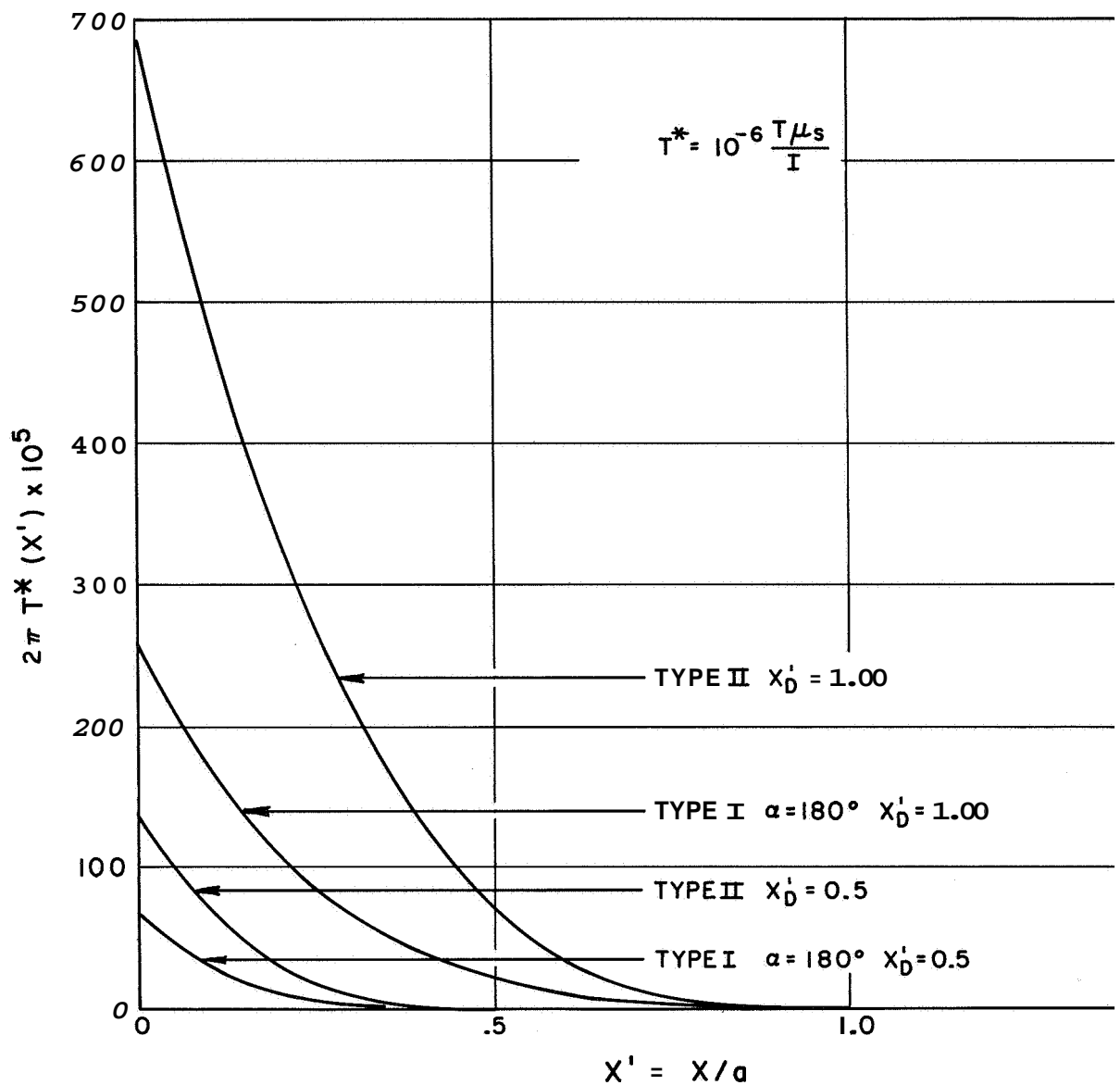


Fig. A-7 Normalized temperature, T^* , rise in gage.

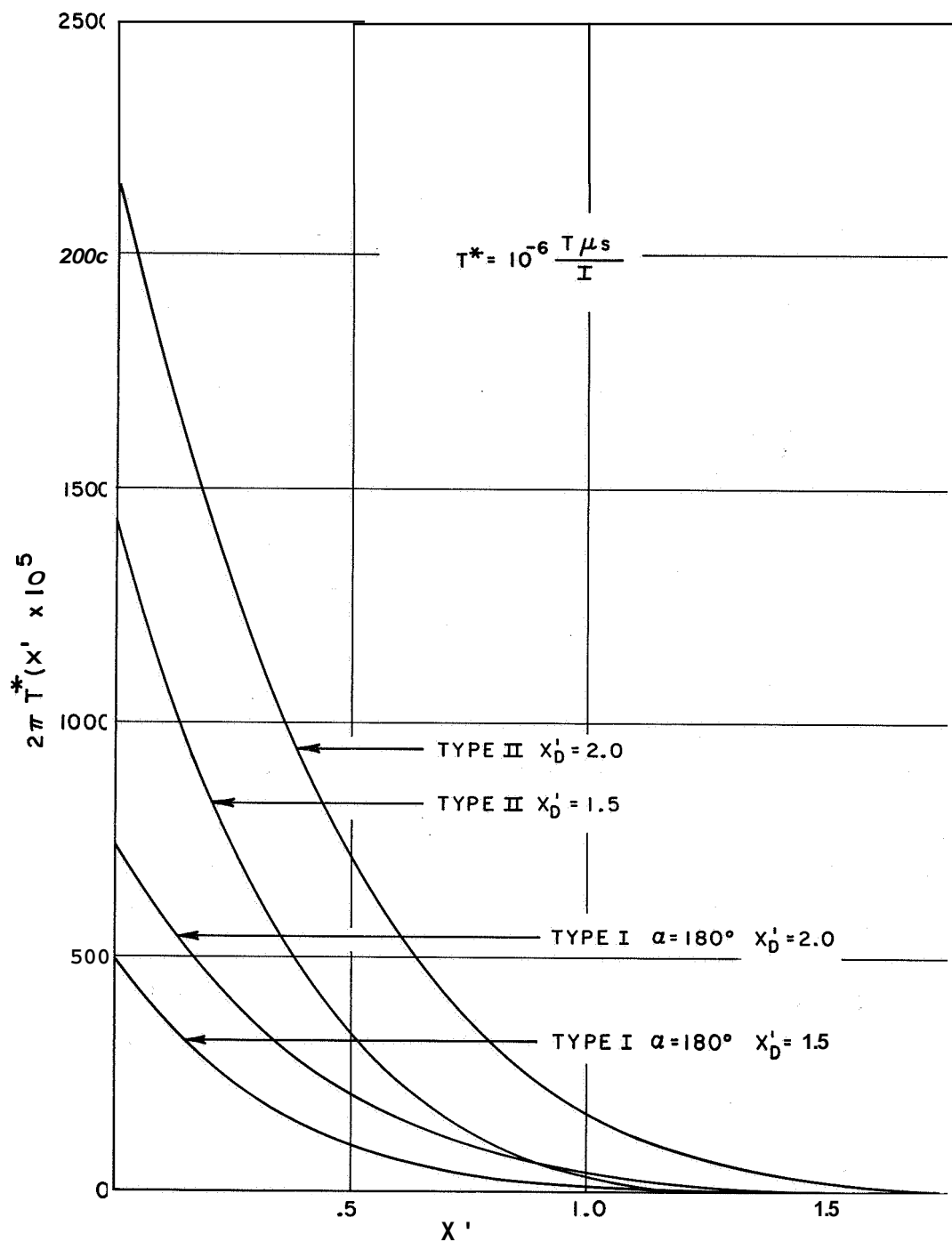


Fig. A-8 Normalized temperature, T^* , rise in gage.

REFERENCES

1. Fay, J. A. , and Riddell, F. R. , "Theory of Stagnation Point Heat Transfer in Dissociated Air," J. Aero. Sci. , vol. 25, p. 73, (1958).
2. Rose, P. H. , and Stark, W. I. , "Stagnation Point Heat-Transfer Measurements in Dissociated Air," J. Aero. Sci. , vol. 25, p. 86, (1958).
3. Kivel, B. , "Radiation from Hot Air and its Effect on Stagnation-Point Heating," J. Aero/Space Sci. , vol. 28, p. 96, (1961).
4. Meyerott, R. E. , "Radiation Heat Transfer to Hypersonic Vehicles," Lockheed Aircraft Corporation Missile Systems Division, Sunnyvale, California, LMSD-2264-R1, September 1958.
5. Camm, J. C., Kivel, B., Taylor, R. L., and Teare, J. D., "Absolute Intensity of Non-Equilibrium Radiation in Air and Stagnation Heating at High Altitudes," Avco-Everett Research Laboratory, Research Report 93, December 1959; also, J. Quant. Spec. Radiat. Transfer, vol. 1, p. 53, (1961).
6. Kivel, B., and Bailey, K. , "Tables of Radiation from High Temperature Air," Avco-Everett Research Laboratory, Research Report 21, December 1957.
7. Rosa, R. J., "Shock Wave Spectroscopy," Phys. Rev., vol. 99, p. 633(A), (1955).
8. Teare, J. D., Georgiev, S. , and Allen, R. A., "Radiation from the Non-Equilibrium Shock Front," Avco-Everett Research Laboratory, Research Report 112, October 1961; also, ARS Preprint No. 1979-61.
9. Allen, R. A. , Keck, J. C. , and Camm, J. C. , "Non-Equilibrium Radiation from Shock Heated Nitrogen and a Determination of the Recombination Rate," Avco-Everett Research Laboratory, Research Report 110, June 1961; also, Phys. of Fluids, vol. 5, p. 284, (1962).
10. Keck, J. C., Camm, J. C. Kivel, B. , and Wentink, T. , Jr. , "Radiation from Hot Air, II," Avco-Everett Research Laboratory, Research Report 42, February 1959; also, Annals of Physics, vol. 7, p. 1, (1959).
11. Goulard, R., A comment on "Radiation from Hot Air and its Effect on Stagnation-Point Heating," J. Aero/Space Sci. , vol. 28, p. 158, (1961).

~~CONFIDENTIAL~~

12. Kennet, H. , and Strack, S. L. , "Stagnation Point Radiative Transfer," ARS Journal, vol. 31, p. 370, (1961).
13. Camm, J. , and Rose, P. H. , "Electric Shock Tube for High Velocity Simulation," Avco-Everett Research Laboratory, Research Report 136, July 1962.
14. Hammerling P. , Teare, J. D. , and Kivel, B. , "Theory of Radiation from Luminous Shock Waves in Nitrogen," Avco-Everett Research Laboratory, Research Report 49, December 1959; also, Phys. of Fluids, vol. 2, p. 422, (1959).
15. Camac, M., and Vaughan, A., " O_2 Dissociation Rates in O_2 -Ar Mixtures," J. Chem. Phys., vol. 34, p. 460, (1961).
16. Lin, S. C., "A Survey of Shock Tube Research Related to the Aero-physics Problem of Hypersonic Flight," ARS Reprint No. 1985-61, (1961).
17. Patrick, R. M. , "High-speed Shock Waves in a Magnetic Annular Shock Tube," Phys. of Fluids, vol. 2, p. 589, (1959).
18. Allen, R. A. , Camm, J. C. , and Keck, J. C. , "Radiation from Hot Nitrogen," Avco-Everett Research Laboratory, Research Report 102, April 1961; also, J. Quant. Spec. Radiat. Transfer, vol. 1, p. 269, (1961).
19. Lin, S. C., Neal, R. A. , and Fyfe, W. J. , "Rate of Ionization Behind Shock Waves in Air. I - Experimental Results," Avco-Everett Research Laboratory, Research Report 105, September 1960.
20. DeVos, J. C. , "A New Determination of the Emissivity of Tungsten Ribbon," Physica, vol. 20, p. 690, (1954).
21. Euler, J. , "The Graphite-Carbon Arc as a Standard (Source) of Intense Radiation," Sitzber Heidelberg. Akad. Wiss. Math. - naturw. Kl. No. 4, p. 413, (1956-57).
22. Taylor, R. , "Continuum Infrared Spectrum of High Temperature Air," Avco-Everett Research Laboratory, Research Report 88, June 1960.
23. Meyerott, R. E. , Sokoloff, J. , and Nicholls, R. A. , "Absorption Coefficients of Air," Lockheed, Sunnyvale, California, LMSD 288052, September 1959.
24. Breene, R. G., and Nardone, M. C. , "Radiant Emission from High Temperature Equilibrium Air," General Electric Co. , MSVD TISR 61SD020, May 1961.

~~CONFIDENTIAL~~

~~CONFIDENTIAL~~

25. Lindenmeier, C.W. , "Kramers' Radiation from Hot Air," Avco-Everett Research Laboratory, Research Note 157, September 1959.
26. Feldman, S. , "Hypersonic Gas Dynamic Charts for Equilibrium Air," Avco-Everett Research Laboratory, Research Report 40, January 1957.
27. Gilmore, F.R. , "Equilibrium Composition and Thermodynamic Properties of Air to 24,000°K," Rand Corporation, Santa Monica, California, RM- 1543, (1955).
28. Hammerling, P. , "Ionization Effects of Precursor Radiation from Shocks in Air," Avco-Everett Research Laboratory, Research Report 98, June 1960.
29. Camac, M. , and Feinberg, R. , "High Speed Infrared Bolometer," Avco-Everett Research Laboratory, Research Report 120, October 1961.
30. Hartunian, R.A., Russo, A.L., and Marrone, P.V., "Boundary-Layer Transition and Heat Transfer in Shock Tubes, " J. Aero/Space Sci. , vol. 27, p. 587, (1960).
31. Bromberg, R., Ramo Wooldridge Report No. 20280, May 1955.
32. Mirels, H. , "The Wall Boundary Layer Behind a Moving Shock Wave," paper presented at Symposium on Boundary Layer Research, Freiburg, Germany, August 1957.
33. Rott, N., and Hartunian, R., "On the Heat Transfer to the Walls of a Shock Tube," Cornell University, Graduate School of Aeronautical Engineering Report, November 1955.
34. Kemp, N. , Avco-Everett Research Laboratory, private communication.
35. Canning, T.N. , and Page, W. A. , "Measurements of Radiation from the Flow Fields of Bodies Flying at Speeds up to 13.4 Kilometers per Second," Ames Research Center; presented to the Fluid Mechanics Panel of Advisory Group for Aeronautical Research and Development, Brussels, Belgium, April 3-6, 1962, NASA, Washington, D. C.
36. Wray, K. L. , "Chemical Kinetics of High Temperature Air," ARS Reprint No. 1975-61, August 1961.
37. Massey, H. S. W., and Burhop, E. H. S., Electronic and Ionic Impact Phenomena, Oxford: Clarendon Press, London, (1952).
38. Faizullov, F.S., Sobolev, N.N., and Kudryavtsev, E.M., "Spectroscopic Investigation of the State of the Gas Behind a Shock Wave. III," Optics and Spectroscopy, vol. 8, p. 400, (1960).

~~CONFIDENTIAL~~

39. Clouston, J. G., Gaydon, A. G., and Hurle, I. R. , "Temperature Measurements of Shock Waves by Spectrum-Line Reversal II. A Double-Beam Method," Proc. Roy. Soc. , A, vol. 252, p. 143, (1959).
40. Gaydon, A. G. , and Hurle, I. R. , "Measurement of Times of Vibrational Relaxation and Dissociation Behind Shock Waves in N₂, O₂, CO, CO₂, and H₂," Eighth Symposium (International) on Combustion, Pasadena, California, (1960). Baltimore, Maryland: Williams and Wilkins, pp. 309-318, (1962).
41. Rose, P. H. , and Teare, J. D. , "On Chemical Effects and Radiation in Hypersonic Aerodynamics," Avco-Everett Research Laboratory, AMP 72, March 1962.
42. Goulard, R. , "The Coupling of Radiation and Convection in Detached Shock Layers," The Bendix Corporation, Research Note 23, December 1960.
43. Wick, B. H. , "Radiative Heating of Vehicles Entering the Earth's Atmosphere," Ames Research Center; presented to the Fluid Mechanics Panel of Advisory Group for Aeronautical Research and Development, Brussels, Belgium, April 3-6, 1962, NASA, Washington, D. C.
44. Treanor, Charles E. , "Radiation at Hypersonic Speeds," ARS Preprint No. 1978-61, August 1961.
45. Feldman, S. , "Trails of Axi-Symmetric Hypersonic Blunt Bodies Flying through the Atmosphere," Avco-Everett Research Laboratory, Research Report 82, December 1959.
46. Whalen, Robert J. , "Viscous and Inviscid Non-Equilibrium Gas Flows, IAS Reprint No. 61-23, January 1961.
47. Lick, W. , "Inviscid Flow of a Reacting Mixture of Gases around a Blunt Body," J. Fluid Mech., vol. 7, p. 128, (1960).
48. Wurster, W. H. , and Marrone, P. V., "Study of Infrared Emission in Heated Air," CAL Report QM 1373-A-4, July 1961.
49. Minzner, R.A., Champion, K.S.W., and Pond, H.L., "The ARDC Model Atmosphere, 1959," Geophysics Research Directorate, Air Force Cambridge Research Center, AFCRC-TR 59-267, August 1959.
50. Hall, J. G., Eschenroeder, A. Q., and Marrone, P. V., "Inviscid Hypersonic Airflows with Coupled Chemical Reactions," IAS Paper 62-67, January 1962.
51. Chapman, Dean R., "An Analysis of the Corridor and Guidance Requirements for Supercircular Entry into Planetary Atmospheres," NASA TR-55, (1959).

~~CONFIDENTIAL~~

52. Rose, P. H. , and Nelson, W. , "On the Effect of Attenuation of Gas Dynamic Measurements Made in Shock Tubes," Avco-Everett Research Laboratory, Research Report 24, March 1958; also, paper presented at the 2nd Shock Tube Symposium, March 5-6, 1958.

~~CONFIDENTIAL~~

~~CONFIDENTIAL~~

THIS PAGE IS BLANK

~~CONFIDENTIAL~~